Scuola Internazionale Superiore di Studi Avanzati - Trieste

Equilibrium and kinetic properties of knotted ring polymers: a computational approach.

A Thesis submitted for the degree of
PhilosophiæDoctor.

Candidate
Luca Tubiana

Supervisor
Cristian Micheletti

Statistical and Biological Physics Group
Ph.D. curriculum in Physics and Chemistry of Biological Systems

Contents

Introduction

Motivation

The study of knotted polymers dates back to the early sixties when Frisch and Wasserman [38] and Delbrück [26] published two important papers in which they discussed the possible occurrence and consequences of knots in circular synthetic polymers and in biopolymers. In particular they correctly conjectured (see ref. [131]) that the knotting probability of a polymer goes to one with increasing polymer length. The subsequent discovery of circular [30, 152, 144] and knotted DNA [69, 68, 68, 123] showed that knots are indeed common in biopolymers, and raised a great interest in understanding their physical and functional implications. In the years following those seminal studies, the improvement of electrophoretic techniques allowed researchers to estimate the probability of formation of different kinds of knots [129, 54, 147], i.e. the knot spectrum, under several conditions. Using the information from the knot spectrum it was possible to understand the mechanism by which several enzymes process DNA [150, 127, 126, 122, 14], the value of DNA effective radius as a function of the concentration of monovalent counterions [120, 123], and more recently even the properties of DNA encapsidated in some bacteriophage capsids [9, 8, 80].

Nowadays, thanks to the advent of micromanipulation techniques, experimentalist are able to tie knots in single polymers and study their effects on the polymer properties as well as their mobility along the polymer backbone. Using optical tweezers, Arai and coworkers were able to tie knots in actin filaments [5]. Testing the filaments resistance to stretching they found that knots tighten under stretching, causing the rupture of the filament as suggested by the numerical investigation of Saitta et al. [121]. As a consequence, the tensile resistance of a polymer is severely decreased by the presence of a knot. Furthermore Bao and Quake [13] showed how knots diffuse along stretched DNA and rationalized the results on the basis of reptation theory.

Given the difficulty of an analytical treatment of knotting, theoretical studies on knots

in polymer have been mainly computational[1]. Since the first seminal studies on knotting probabilities [148], numerical simulations of polymer rings have been used to characterize the knotting probability for polymer rings of increasing contour length [60, 137, 102] under several physical conditions (e.g. polymer thickness, degree of confinement, globular polymers, etc.) [89, 59, 120, 74, 8, 9, 86, 87, 80]. Those studies have been proved to be of fundamental importance in conjunction with experimental knot spectra to ascertain DNA characteristics in several conditions.

Computational studies have been widely adopted to investigate the influence of knots on polymers as well. Geometrical properties like the radius of gyration of polymer rings have been shown to be topology dependent for short rings [109, 54] as well as highly charged rings like DNA, a fact which can be used to characterize electrophoresis results [129, 147]. On the other hand very long polymer rings seems to behave like unknots, a fact which can be explained with knots becoming localized along the ring [100, 101]. This knot localization has been recently experimentally confirmed for adsorbed double-stranded DNA [33].

Simulations of tensioned DNA [15, 84, 48] showed that knots can diffuse along tensioned filaments, with a diffusion coefficient arguably depending on the tightness of the knot. Computationally it has also been demonstrated that knots affect polymer translocation through a pore [114], possibly affecting genome ejection from bacteriophages [81, 80]

The historical perspective we presented highlights a two-way relationship between physical and topological properties of polymers. On one hand, physical interactions and geometrical constraints affect polymers knotting probabilities, measured by the knot spectrum. On the other hand, we saw that the presence of a knot on a polymer affects its physical and geometrical properties.

In this thesis we investigate numerically the relationship between topological and geometrical entanglement and their relationship with physical properties of biopolymers, particularly DNA. Since many biopolymers and particularly DNA are often subject both to confinement inside regions with calliper size that is smaller than their contour length (e.g. the Eukariotic nucleus, mitochondria, bacteria, bacteriophage capsids..) and to geometrical entanglement due to the presence of other polymers in high density solutions, we will dedicate particular effort to clarify the relationships between topological and geometrical/physical properties of polymers in these two situations. A key element of

[1]Notably, one of the few analytical results is the theorem by Sumners and Whittington, proving that with increasing polymer length the probability of finding a knot goes to one [131]

our study will be the characterization of the degree of localization (tightness) of the knot in all the considered circumstances.

Outline of the Thesis

We provide hereafter a summary of the Thesis organization. Chapter 1 contains a short introduction to the mathematical theory of knots. Starting from the mathematical definition of knotting, we introduce the fundamental concepts and knot properties used throughout this Thesis.

In chapter 2 we tackle the problem of measuring the degree of localization of a knot. This is in general a very challenging task, involving the assignment of a topological state to open arcs of the ring. To assign a topological state to an open arc, one must first close it into a ring whose topological state can be assessed using the tools introduced in chapter 1. Consequently, the resulting topological state may depend on the specific closure scheme that is followed. To reduce this ambiguity we introduce a novel closure scheme, the *minimally-interfering closure*. We prove the robustness of the minimally-interfering closure by comparing its results against several standard closure schemes.

We further show that the identified knotted portion depends also on the search algorithm adopted to find it. The knot search algorithms adopted in literature can be divided in two general categories: bottom-up searches and top-down searches. We show that bottom-up and knot-down searches give in general different results for the length of a knot, the difference increasing with increasing length of the polymer rings. We suggest that this systematic difference can explain the discrepancies between previous numerical results on the scaling behaviour of the knot length with increasing length of polymer rings in good solvent.

In chapter 3 we investigate the mutual entanglement between multiple prime knots tied on the same ring. Knots like these, which can be decomposed into simpler ones, are called *composite knots* and dominate the knot spectrum of sufficiently long polymers [131]. Since prime knots are expected to localize to point-like decorations for asymptotically large chain lengths, it is expected that composite knots should factorize into separate prime components [101, 82, 43, 11]. Therefore the asymptotic properties of composite knots should merely depend on the number of prime components (factor knots) by which they are formed [101, 82, 43, 11] and the properties of the single prime components should

be largely independent from the presence of other knots on the ring. We show that this factorization into separate prime components is only partial for composite knots which are dominant in an equilibrium population of Freely Jointed Rings. As a consequence the properties of those prime knots which are found as separate along the chain depend on the number of knots tied on it. We further show that these results can be explained using a transparent one-dimensional model in which prime knots are substituted with paraknots.

Chapters 4, 5 and 6 are dedicated to investigate the interplay between topological entanglement and geometrical entanglement produced either by surrounding rings in a dense solution or spherical confinement.

In chapter 4 we investigate the equilibrium and kinetic properties of solutions of model ring polymers, modulating the interplay of inter- and intra-chain entanglement by varying both solution density (from infinite dilution up to $\approx 40\%$ volume occupancy) and ring topology (by considering unknotted and trefoil-knotted chains). The equilibrium metric properties of rings with either topology are found to be only weakly affected by the increase of solution density. Even at the highest density, the average ring size, shape anisotropy and length of the knotted region differ at most by 40% from those of isolated rings. Conversely, kinetics are strongly affected by the degree of inter-chain entanglement: for both unknots and trefoils the characteristic times of ring size relaxation, reorientation and diffusion change by one order of magnitude across the considered range of concentrations. Yet, significant topology-dependent differences in kinetics are observed only for very dilute solutions (much below the ring overlap threshold). For knotted rings, the slowest kinetic process is found to correspond to the diffusion of the knotted region along the ring backbone.

In chapter 5 we study the interplay of geometrical and topological entanglement in semiflexible knotted polymer rings under spherical confinement. We first characterize how the top-down knot length l_k depends on the ring contour length, L_c and the radius of the confining sphere, R_c. In the no- and strong-confinement cases we observe weak knot localization and complete knot delocalization, respectively. We show that the complex interplay of l_k, L_c and R_c that seamlessly bridges these two limits can be encompassed by a simple scaling argument based on deflection theory. We then move to study the behaviour of the bottom-up knot length l_{sk} under the same conditions and observe that it follows a qualitatively different behaviour from l_k, decreasing upon increasing confinement. The behaviour of l_{sk} is rationalized using the same argument based on

deflection theory. The qualitative difference between the two knot lengths highlights a multiscale character of the entanglement emerging upon increasing confinement.

Finally, in chapter 6 we adopt a complementary approach, using topological analysis (the properties of the knot spectrum) to infer the physical properties of packaged bacteriophage genome. With their μm long dsDNA genome packaged inside capsids whose diameter are in the $50 - 80$ nm range, bacteriophages bring the highest level of compactification and arguably the simplest example of genome organization in living organisms [31, 40]. Cryo-em studies showed that DNA in bacteriophages epsilon-15 and phi-29 is neatly ordered in concentric shells close to the capsid wall, while an increasing level of disorder was measured when moving away from the capsid internal surface. On the other hand the detected spectrum of knots formed by DNA that is circularised inside the P4 viral capsid showed that DNA tends to be knotted with high probability, with a knot spectrum characterized by complex knots and biased towards torus knots and against achiral ones. Existing coarse-grain DNA models, while being capable of reproducing the salient physical aspects of free, unconstrained DNA, are not able to reproduce the experimentally observed features of packaged viral DNA. We show, using stochastic simulation techniques, that both the shell ordering and the knot spectrum can be reproduced quantitatively if one accounts for the preference of contacting DNA strands to juxtapose at a small twist angle, as in cholesteric liquid crystals.

The material presented in this thesis is largely based on the following articles:

- L. Tubiana, E. Orlandini and C. Micheletti, *Probing the entanglement and locating knots in ring polymers: a comparative study of different arc closure schemes*, Progress of Theoretical Physics Supplement **191**, 192-204, December 2011.

- A. Rosa, E. Orlandini, L. Tubiana and C. Micheletti, *Structure and dynamics of ring polymers: entanglement effects because of solution density and ring topology*, Macromolecules **44**, 8668-8680, October 2011.

- L. Tubiana, E. Orlandini and C. Micheletti, *Multiscale entanglement in ring polymers under spherical confinement*, Physical Review Letters **107**, 188302-188306, October 2011.

- D. Marenduzzo, E. Orlandini, A. Stasiak, D.W. Sumners, L. Tubiana and C. Micheletti,*DNA-DNA interactions in bacteriophage capsids are responsible for the*

observed DNA knotting, Proceedings of the National Academy of Sciences of the U.S.A. **106**, 22269-22274, December 2009.

Chapter 1

A short introduction to knot theory

1.1 Basic introduction to knot theory

In this section we provide a basic introduction to knot theory, tailored on the topics of interest in this thesis. For an extensive introduction to the subject we refer the interested reader to the books by Adams [1], Livingston [70] and Cromwell [24].

1.1.1 Knot definition

From our daily experience, we are used to think of knots as entanglements in ropes, made by tying or interweaving a rope so that it can bind to itself. On the other hand in defining a knot mathematically one wants to preserve its fundamental properties, dictated by the way it is tied, abstracting away all those physical properties which depend on particular conditions like the thickness of the rope, its friction coefficient, the tightness of the knot, etc. To do so imagine to tie a knot in a very thin string made of highly deformable, frictionless rubber and then glue the ends of the string together, as depicted in Fig. 1.1. Now the knot is trapped in the rubber ring. No matter how we deform the rubber ring, we can not untie the knot or change it to another knot without cutting open the ring. If we take the rubber ring to be infinitely thin and perfectly flexible, we have abstracted away all physical properties related to the string. Similarly a knot can be defined mathematically as an embedding of the circle $\mathbb{S}^1$ in euclidean space $\mathbb{R}^3$. Two embeddings are said to be equivalent and to describe the same knot if there exists an *ambient isotopy* transforming one into the other. An ambient isotopy of a space $X \subset \mathbb{R}^3 \to \mathbb{R}^3$ is an isotopy of $\mathbb{R}^3$ that carries X with it. To picture it, imagine the knot as a thin thread embedded in a viscous fluid, like honey. Stirring the honey causes the thread to move and change conformation in response [24]. The use of ambient isotopies

Figure 1.1: To be suitable to mathematical analysis a physical knot (depicted on the left) must be closed. Knot theory works on idealized knots like the one depicted on the right.

guarantees that pathological behaviours such as the unknotting depicted in Fig. 1.2 are avoided.

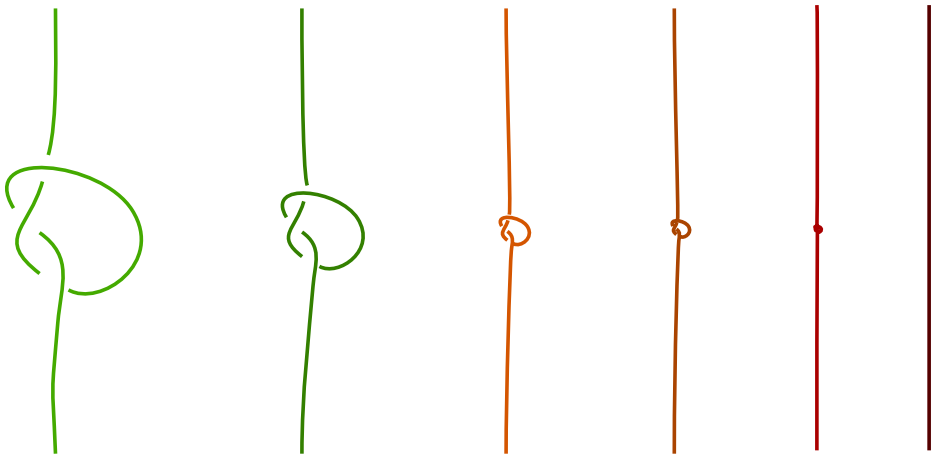

Figure 1.2: Bachelors' unknotting: a continuous isotopy which makes a knot vanish into a point.

The definition of knot we introduced is very general and allows also for knots which can not be tied with "real" ropes or threads, such as the one in Fig. 1.3, Such knots are known as "wild knots". To avoid such pathological behaviour while at the same time being able to describe all physically representable knots, knots which can be tied with physical objects such as strings or polymers, one restricts the set of admissible curves. It is intuitive and it can be proved [24], that all physically representable knots, known

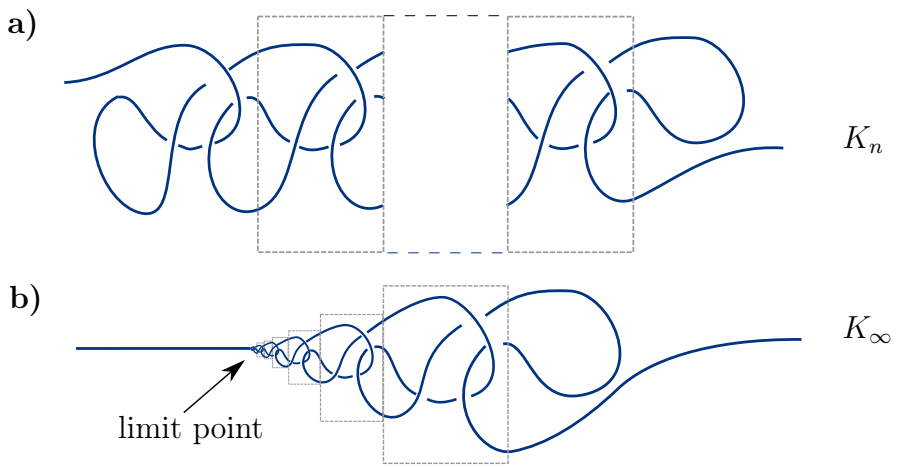

Figure 1.3: a) A trivial knot, K_n, made by n repetitions of the tangle shown in the box. Clearly, even if the pattern is repeated an infinite number of times the resulting knot will still be trivial. b) A wild knot, K_∞, made by repeating the tangle an infinite number of times while reducing it by a constant factor. In this case it is possible to prove that K_∞ is not a trivial knot [24].

as *tame knots*, can be described using piecewise-linear curves. We therefore limit our definition of knot to the following.

Definition 1 (Knot)**.** A knot is a simple closed polygonal curve in $\mathbb{R}^3$.

Here *simple* means that no intersections of edges are possible apart for the intersection of two successive edges at each vertex of the polygon.

1.1.2 Knot tabulation

At the heart of knot theory lies the task of distinguishing and tabulating knots. Knots can be represented pictorially through (regular) *knot diagrams*, planar projections of the three-dimensional embedding, whose only singular points are transverse double points where two strands cross each other. Underpassing strands in every crossings are drawn interrupted in order to carry the information on the relative height of the strands, as in Fig. 1.1 (c)[1].

The same knot can be represented by infinitely many diagrams, as every change of its three-dimensional embedding produces a different projection. It is possible to show that

[1]More generally, a (non-regular) knot diagram can involve singular points which are not double points. It can be proven that tame knots always have a regular knot diagram. Therefore in the following we will tacitly assume we are working with regular knot diagrams.

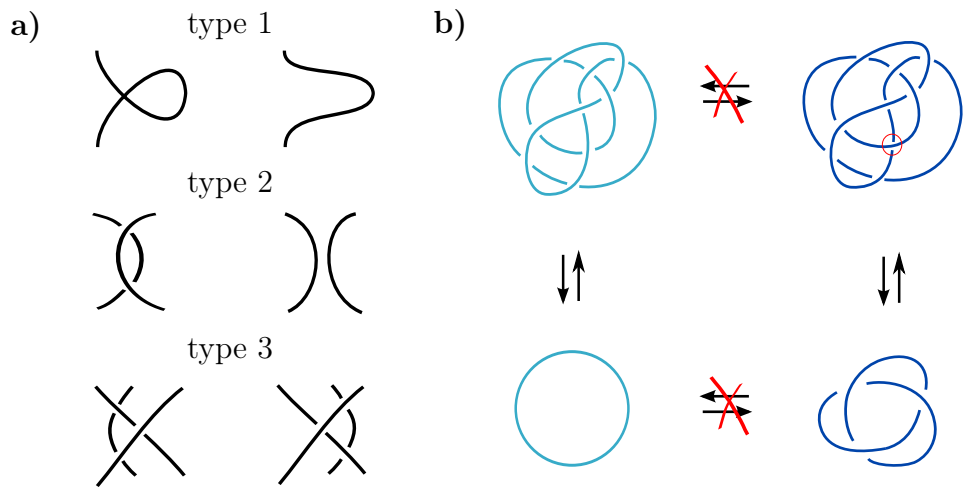

Figure 1.4: a) Reidemeister moves. b) Diagram equivalence relations through Reidemeister moves. The two diagrams on the left both represent the unknot and can be transformed one into the other trough a sequence of Reidemeister moves. The same is true for the two diagrams on the right, representing a trefoil knot. No set of Reidemeister moves exists which can transform one of the diagrams on the left (right) into one of the diagrams on the right (left).

two diagrams represent the same knot through the use of *Reidemeister moves*. These three moves, represented in Fig.1.4, together with an isotopy of the plane, cover all possible topology preserving deformations of a knot diagram. It can be proved that two knots are equivalent if and only if their diagrams can be made identical in this way.

Knots can be characterised through *topological invariants*, whose values depend only on the kind of knot but not on its geometrical representation or projection. There are several kinds of topological invariants, the most famous one being the *minimal crossing number* C of a knot, which is defined as the minimum number of crossings appearing in any diagram of the knot. The knot diagram having the minimum number of crossing is called the *minimal diagram* of the knot. Knots are conventionally tabulated according to their crossing number, as in Fig. 1.5. Knots with the same crossing number are labelled with an increasing index to distinguish them, like for example knots 5_1 and 5_2.

1.1.3 Prime and composite knots

Knots can be added up trough a procedure called *connected sum*, which is equivalent to tie several knots on the same rope (see Fig.1.5 b)). It is intuitive and it can be proved that it is not possible to reduce a knot to a trivial knot 0_1 by summing another knot to

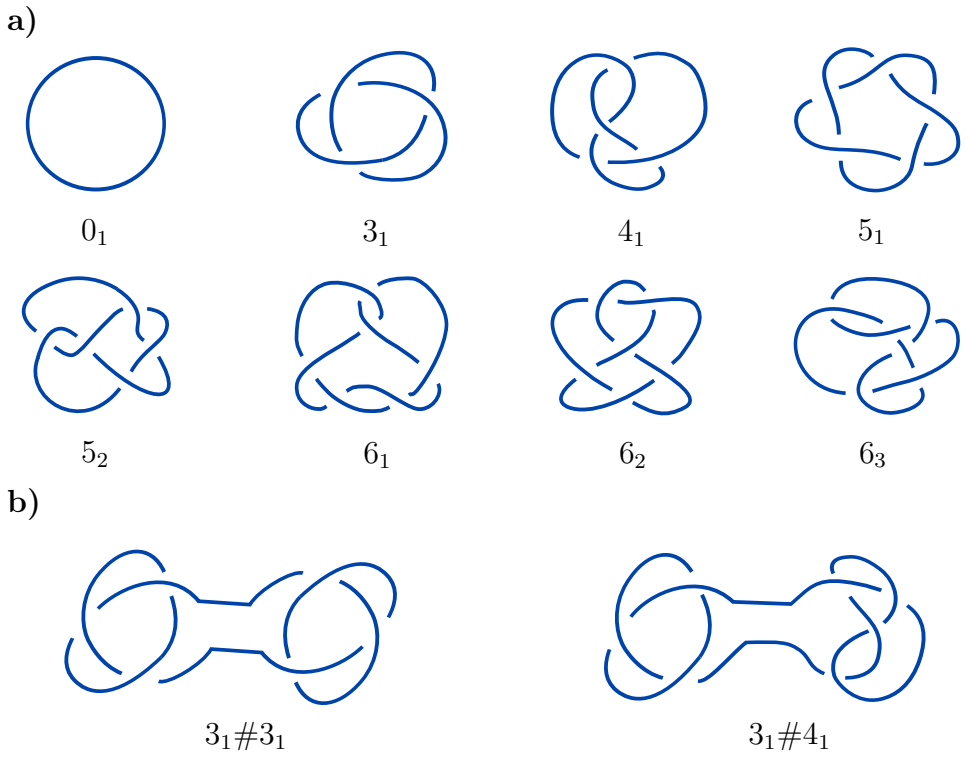

Figure 1.5: a) Knot diagrams of simple knots up to crossing number 6. A broken line in a diagram indicates where a part of the curve underpass another part. b) Knot diagrams of two composite knots with two components.

it, so no "antiknot" exists. A knot $\tau\#\tau'$ obtained by the connected sum of knots τ and τ' is called a *composite knot*, while τ and τ' are called *factor knots* of $\tau\#\tau'$. Clearly the trivial knot 0_1 is a factor knot of all knots: $\tau\#0_1 = \tau$. A knot τ which admits as factor knots only itself and the trivial knot is called a *prime knot* in analogy to prime numbers. Knot composition has the following important properties: i) it is associative, ii) it is commutative, $\tau\#\tau' = \tau'\#\tau$ and iii) every composite knot admits a unique decomposition in prime factor knots.

1.1.4 Some properties of knots

Different knots can show different properties and can be divided in families on the basis of the properties they share. In this thesis we will consider in particular the concept of *chirality* of knots, as well as *torus* and *twist* knot families.

A knot is said to be chiral if there exist no ambient isotopy bringing an embedding of

the knot to its specular image. A typical example is the trefoil knot (see Fig.1.6). On the other hand a knot whose embeddings can always be transformed into their specular images is called achiral. Between the simple knots reported in Fig. 1.5 only knots 4_1 and 6_3 are achiral. When working with simple knots with less than eight crossings there is a

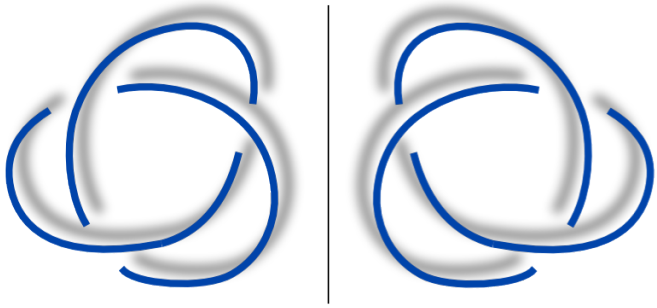

Figure 1.6: The two enantiomers of trefoil knot are topologically distinct.

straightforward method to distinguish the two enantiomers. First attach an orientation to the knot diagram. The crossings of an oriented diagram can be only of the two kinds shown in Fig. 1.1.4, called positive or negative according to the right-hand rule. Summing $+1$ for all positive crossings of a knot diagram and -1 for all negative crossings one can assign a $+$ or $-$ sign to the knot, distinguishing its chirality, as in Fig. 1.6. For knots with 8 or more crossings this algorithm is not guaranteed to work anymore, as in the case of the famous Perko knots, which have been found to be different diagrams of the same knot.

Torus knot are characterized by the fact that they can be drawn as a nonintersecting continuous closed curve on the surface of a standardly embedded torus (see Fig. 1.8). Torus knots have many important properties, in particular all torus knots are chiral.

Twist knots can be tied by twisting a ring n times and then clamping the free loops together (see Fig. 1.9). In Fig. 1.5 twist knots are 3_1, 4_1, 5_2 and 6_1.Twist knots can be either chiral or achiral.

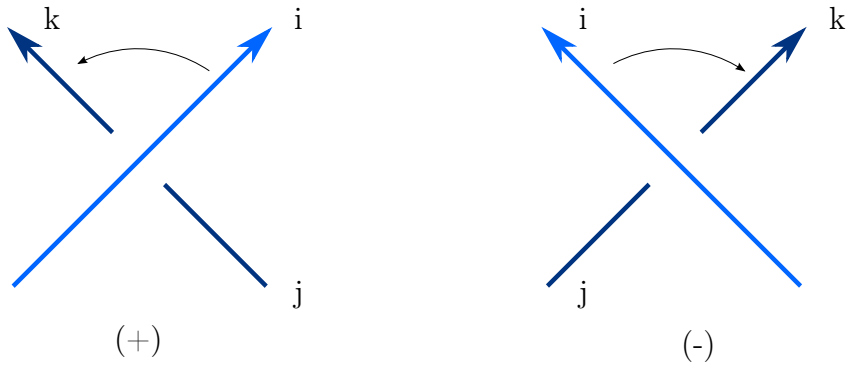

Figure 1.7: Positive and negative crossings are defined through the right-hand rule. Labels are used for the computation of the Alexander Polynomial.

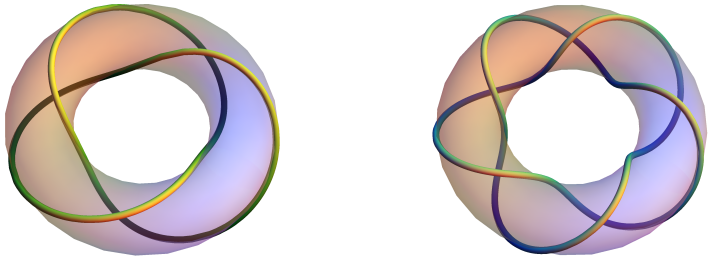

Figure 1.8: The two torus knots with less than 7 crossings: 3_1 (left) and 5_1 (right).

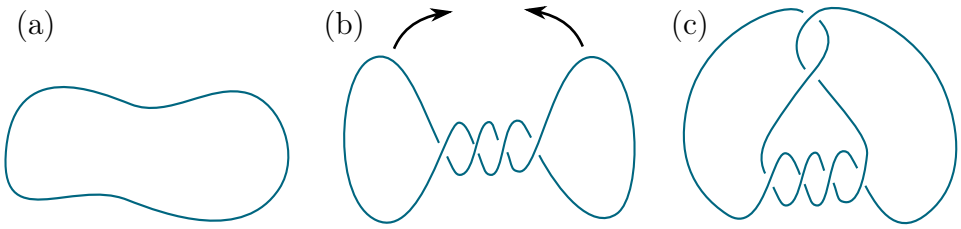

Figure 1.9: Twist knots can be tied by taking a ring (a), twisting it keeping two loops (b) and clamping together the two loops (c).

1.1.5 The Alexander Polynomial

As we pointed out in § 1.1.2, it is crucial to be able to distinguish different knots from each others, independently of their particular embedding. Several topological invariant have been devised during the past years, the most used in numerical studies

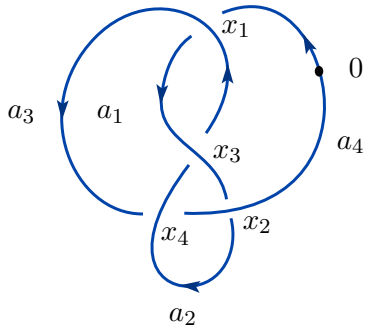

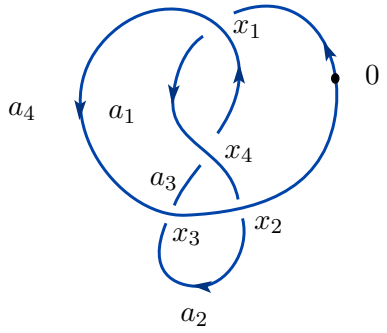

$$\mathbf{M}(t) = \begin{pmatrix} t & 0 & 1-t & -1 \\ t & -1 & 0 & 1-t \\ 1-t & -1 & t & 0 \\ 0 & 1-t & t & -1 \end{pmatrix} \qquad \mathbf{M}(t) = \begin{pmatrix} -1 & 0 & 0 & 1 \\ t & -1 & 0 & 1-t \\ 0 & -1 & t & 1-t \\ 1-t & 0 & -1 & t \end{pmatrix}$$

$$\begin{vmatrix} 0 & 1-t & -1 \\ -1 & 0 & 1-t \\ -1 & t & 0 \end{vmatrix} = -t^2 + 3t - 1 \qquad \begin{vmatrix} -1 & 0 & 0 \\ t & -1 & 0 \\ 0 & -1 & t \end{vmatrix} = t$$

$$\Delta(t; 4_1) = t^2 - 3t + 1 \qquad \Delta(t; 0_1) = +1$$

Figure 1.10: Computing the Alexander polynomial for two different knots. A 3_1 on the left and an unknot on the right. Note that the unknot diagram is not minimal.

being algebraic invariants like *knot groups*, *Vassiliev invariants*, *Jones*, *HOMFLY* and *Alexander* polynomials. In this thesis we often use the Alexander polynomial to distinguish simple knots from each others. The Alexander polynomial is defined for a regular knot diagram in terms of a single variable t and can be implemented on a computer using the following algorithm (see for example [148]).

1. Assign an orientation to the knot diagram and establish the sign of each crossing following the right-hand rule as in Fig. 1.1.4.

2. Starting from an arbitrary non-crossing point of the diagram, 0, follow the ring orientation and assign an increasing numbering index to all the undercrossings.

3. Consider arcs as going from an undercrossing to the next one. Starting from point 0 and following the orientation, assign an increasing numbering index to all the arcs in the diagram.

4. Define an $n \times n$ matrix $\mathbf{M}(t, \tau)$. The rows of $\mathbf{M}$ correspond to the crossings of the diagram, the columns to the arcs. For every crossing x we assume for definiteness that the arc i passes over arcs j and k. The matrix is constructed starting from a matrix with all entries equal to zero and summing the following values for the entries $\mathbf{M}(x,i), \mathbf{M}(x,j), \mathbf{M}(x,k)$ of all crossings x.
   - If x is a positive crossing, $\mathbf{M}(x,i) = +1 - t$, $\mathbf{M}(x,j) = -1$, $\mathbf{M}(x,k) = +t$
   - If x is a negative crossing, $\mathbf{M}(x,i) = +1 - t$, $\mathbf{M}(x,j) = +t$, $\mathbf{M}(x,k) = -1$.
   - If $i = k$ or $i = j$, $\mathbf{M}(x,j) = 1$ and $\mathbf{M}(x,k) = -1$ irrespective of the crossing's sign.

5. Compute any minor of order $n-1$ of the matrix $\mathbf{M}$ and multiply it by a quantity $\pm t^m, -m \in \mathbb{N}$ in such a way that the resulting polynomial does not contain negative powers, and has a positive constant term. Such a minor is the (irreducible) Alexander polynomial $\Delta(t;\tau)$ of the knot τ.

The calculation of the Alexander polynomial for a 4_1 knot and for a trivial knot with a similar projection is reported in Fig. 1.10. The Alexander polynomial does not depend on the particular knot diagram used to calculate it, but only on the knot type and is therefore a topological invariant [2].

Exchanging positive and negative crossings for all crossings, does not change the resulting Alexander polynomial, which therefore is unable to distinguish between two enantiomers of a chiral knot, like $(+)3_1$ and $(-)3_1$. Another useful property of the Alexander polynomial is that for a composite knot $\Delta(t;\tau_1\#\tau_2) = \Delta(t;\tau_1)\Delta(t;\tau_2)$.

The Alexander polynomial is not a very powerful discriminator, as several knots can have the same polynomial. This is true for all known knot polynomials although some are more powerful than others in discriminating different knots. Between the simple knots with less than eleven crossings only six of them share the same Alexander polynomial, making it a convenient topological discriminator for numerical works thanks to its small computational cost. In this thesis the Alexander polynomial is used to distinguish knots with less than eight crossings, for which there is no ambiguity. As in many computation works, we will not compute the whole polynomial, but rather its values in $t = -1$ and $t = -2$, $\Delta(-1)$ and $\Delta(-2)$ which allow one to distinguish the first 84 prime knots [2].

We note here that the computational cost of computing the Alexander matrix grows with the number of crossings in a projection. To reduce this cost it is customary to transform knots projections into equivalent ones with fewer crossings, for example by using Reidemeister moves. Another possible approach is to transform the three-dimensional embedding of the knot in a simpler one without changing its topology. Working with piecewise linear knots, i.e. polygons, one can considerably reduce the complexity of their projections by reducing the number of edges of the polygons without changing the topology of the knots. In this thesis we follow this latter approach. Our simplification scheme is a generalization of the well known rectification scheme [60, 137, 132, 145] and is described in detail in § 2.3.3

Chapter 2

Probing the entanglement and locating knots in ring polymers

It is known that the global topological state of a ring polymer affects its salient physical properties such as its size [27, 92] sedimentation velocity, gel-electrophoretic mobility [129, 151, 103], resistance to mechanical stretching [121, 5], and velocity of translocation through a pore [114].

While a comprehensive understanding of this phenomenon is still lacking, it is often explicitly or implicitly acknowledged that topology-dependent physical properties arise because of a sophisticated interplay of polymer geometry and topology. In other words, the global topological state affects the average geometrical properties of the polymer, which in turn directly impact various physical properties such as those mentioned above.

A vivid illustration of this relationship is offered by the mechanical resistance of a knotted polymer that is pulled at both ends. The breaking force depends on the topological state of the polymer. Indeed, the rupture point is invariably in correspondence of the knot [121, 5] which is progressively tightened by the pulling action. The above example highlights a very important player in the relationship between the topological, geometrical and physical properties of a ring polymer (or a polymer with constrained ends), namely the degree of localization of the topologically-entangled region [99]. While locating a tight knot on a rope by visual inspection is straightforward, to locate a generic, possibly loose knot on a polymer of known topology can be highly challenging. To accomplish this task one needs to assign a topological signature to any portion, or arc, of the polymer and then select the shortest arc(s) whose topology matches that of the whole ring. Such procedure presents two difficulties. The first and more obvious one is that assigning a topology to a subportion of a polymer presents the same ambiguities faced in assigning a topology to an open polymer. In order to do so one has to close the arc into a ring in

a suitable way and measure the topology of such ring. This operation can itself alter the measured topology if the closure interferes with the arc to be closed, for example by piercing through a loop. The second, more subtle, difficulty lies in the way one looks for the smallest arc having the same topology of the whole polymer. As we will see for the case of polymer rings different algorithms to locate the knotted portion result in different entanglements being measured. This fact may explain some of the discrepancies in the known results on knot localization.

In this chapter we tackle both difficulties involved in locating the knotted portion of a knotted ring polymer. We start in § 2.1 by introducing the *minimally-interfering* closure scheme, a new fast and robust algorithm we developed to assign a topological status to open chains. In § 2.2 we compare the minimally-interfering closure against three different closure schemes of common use: the *direct bridging closure*, the *radial closure* [75] and the *stochastic closure* [90]. The comparison is performed by computing the knot matrix of three trefoil knotted freely jointed rings of increasing compactness and geometrical complexity. From the comparative investigation we ascertain that for the ring with the least degree of compactness (spatially unconstrained), the various closure schemes yield consistent results. For the higher level of compactness noticeable differences emerge between the direct bridging method and the other schemes. Notably, despite their different formulation, the stochastic closure and the computationally faster minimally-interfering closure appear to be well consistent for all the considered levels of ring compactification. This is an important result as it gives an *a posteriori* indication of an overall consensus of unrelated methods about the topological state of various portions of rings with different geometrical complexity.

In section § 2.3 we tackle the second difficulty, namely the knot search algorithm, showing that several knot-searching algorithms introduced in literature can be divided into two broad categories, which we call "bottom-up" and "top-down" search schemes. We describe two algorithms, one for each category and compare them against each other, showing that in general they give different results for the length of the knotted portion. We then apply our algorithms to study knot localization on infinitely thin trefoil knotted rings and find that while both methods confirm that knot are localized on very long rings, they result in two different approaches to this localized state. In fact, we observe that the difference in the average knot length measured by the two algorithms increases with increasing length.

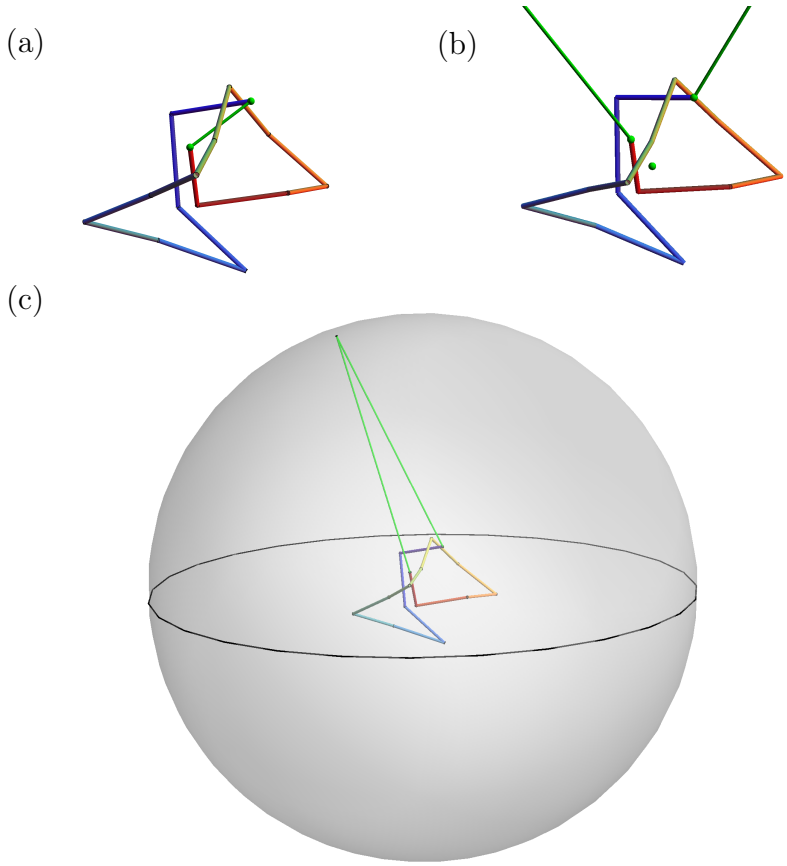

Figure 2.1: Three closure schemes proposed in recent years. (a) Direct bridging of the two termini, (b) radial closure and (c) stochastic closure. Closing segments are drawn in green. In (b) the green sphere represents the position of the center of mass of the arc to be closed. This and some other images in this chapter have been adapted from ref. [139].

2.1 Knotting of open chains: closure schemes

Defining the knot status of open chains is in general a challenging problem. As we already pointed out, to apply the mathematical definition of knot and knot theory tools it is first necessary to close the chain into a ring. To do so, several viable arc closure schemes can be used and they can result in different knots being measured on the same arc. This is especially the case for rings under geometrical confinement [90, 102, 76]. The most widely used closure schemes at the moment of writing this thesis are the *direct bridging closure* [145], the *radial closure* [75, 145] and the *stochastic closure* [90].

Direct closure The chain ends are directly joined by a straight line as in Fig. 2.1 (a).

Radial closure Each chain end is prolonged outwards along the line connecting the center of mass of the chain to that end (see Fig. 2.1 (b)). The prolonged segments are then joined by an arc on a sphere centered on the center of mass of the chain and having radius much larger than the dimensions of the chain (infinite radius).

Stochastic (MDS) closure One starts by computing the smallest enclosing sphere for the chain to be closed and rescales its radius by a large factor (10 in the present study). The two chain ends are connected by a random point drawn with uniform distribution on this sphere as in Fig. 2.1 (c). The closure is repeated a large number of times with different random points, resulting in a knot spectrum for the chain. The topological state with the largest statistical weight is identified and if the weight exceeds a preassigned threshold, q, it is taken as the topological state of the chain. Otherwise the topology of the chain is considered to be ambiguous and it is left unassigned. Typical threshold values are $q = 50\%$ and $q = 90\%$.

Every scheme has its advantages and disadvantages. The direct closure is the easiest to implement, and it can be safely used to study the statistical properties of loose linear polymers, for which it gives results qualitatively compatible with those given by a radial closure [145]. On the other hand the direct closure is not reliable for studying globular proteins or confined polymers. When their ends are on the outside of globule, a case often encountered for proteins in the pdb, the direct closure greatly interferes with the chain to be closed. As a result spurious topologies are often measured. Some knotted proteins in the pdb, for example, are seen as unknotted by the direct closure schemes. The radial closure scheme, on the other hand, implicitly assumes that the chain ends are not buried within the rest of the polymer. While this is a good assumption for loose and θ-point polymers, its validity is questionable for polymers which are either collapsed or under geometrical confinement. Finally the stochastic closure is based on a radically different concept. It generates a spectrum of possible knots for the chain to be closed and therefore permits a statistical analysis of its knotting status. The price to be paid for this greater detail lies in much longer computational times compared to non-stochastic schemes. In numerical studies nonetheless there is often the necessity to assess the topological status of hundreds of thousands of chains, which translate into the necessity of having a closure scheme which is not only reliable but also computationally efficient.

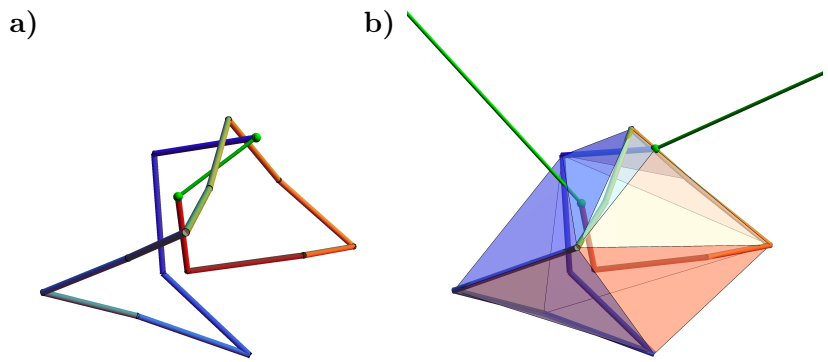

Figure 2.2: a) direct closure. b) Convex-hull closure. The minimally interfering closure choose either a) or b) to close a chain on the basis of an estimate of their relative interference with the chain to be closed.

Minimally-interfering closure The requirements of reliability and computational efficiency motivated us to develop a new closure scheme, designed to be more reliable than both the direct and radial closure schemes, while remaining computationally efficient to be used in extensive studies on large datasets.

The rationale behind this scheme, which we call *minimally-interfering* closure, is that the degree of interference introduced by non-stochastic closure schemes can be intuitively related to the distance travelled by the closing arcs amidst the chain. It is then natural to try to reduce this distance. In order to do so the minimally-interfering closure computes the convex hull enclosing the chain to be closed and seeks to minimize the distance spanned by the closing arc(s) inside it. To do so the sum of the distances from each end to the surface of the convex hull, d_{out}, is computed and compared to the distance between the two chain ends, d_{in}. If $d_{out} < d_{in}$ the two ends are prolonged to infinity through their nearest points on the surface of the convex hull and joined on a sphere much larger than the convex hull. If $d_{in} \leq d_{out}$ the chain ends are directly connected.

This procedure leads to a closure scheme which is more reliable than both the radial and direct closures, as a direct or an outward closure are chosen appropriately to reduce the closure interference, and computationally very efficient requiring the topological evaluation of only one ring.

2.2 Comparison of different closures

2.2.1 Knot matrices

To compare the minimally-interfering closure scheme against the other closure schemes introduced in § 2.1 we use *knot matrices*. Given a ring $\Gamma = \{\vec{r}_1, \vec{r}_2, \ldots, \vec{r}_N, \vec{r}_{N+1} = \vec{r}_1\}$ with N vertices, its knot matrix is a $N \times N$ matrix formed by assigning a topological state to every open subportion of the ring (arc). In the following we will denote by $\Gamma_{ij} = \{\vec{r}_i, \ldots, \vec{r}_j\}$ the arc comprising all edges from vertex i to vertex j (including the endpoints i and j). The orientation of Γ_{ij} follows the one given by the increasing numbering of the nodes on the full ring.

To construct the knot matrix of a ring Γ we consider all possible $N(N-1)$ oriented arcs, Γ_{ij}, with $i \neq j$. After circularization, the topological state of each arc is established using the Alexander determinants computed in -1 and -2 (see § 1.1.5). By convention the diagonal of the matrix is taken to correspond to the whole ring. The knot matrix entries, which take on discrete values reflecting the variety of knots trapped in the arcs, are conveniently conveyed in color-coded graphical representations, see Fig. 2.3. The graphical representation adopted here follows the indexing convention first introduced by Yeates et al. to highlight the presence of slipknots in naturally-occurring proteins [58].

As illustrated in Fig. 2.3 by analysing the knot matrix it is possible to recover a wealth of information about the interplay of the geometrical and topological entanglement of the ring. In particular, as we will see in § 2.3, it is possible to locate the position of a knot on a chain and characterize its degree of tightness.

2.2.2 Polymer model

The degree of entanglement is measured for the simplest model of ring polymers, that is freely-jointed rings (FJRs). These rings are fully-flexible equilateral polygons and no excluded volume interaction is introduced between the ring edges or vertices.

It is known that the global topological complexity of the rings is strongly influenced by the level of imposed spatial confinement. Typically, a higher degree of ring compactification leads to more complex knots. This aspect was initially investigated by Michaels and Wiegel [89] and more recently by other studies [8, 86, 87, 80] in biologically-motivated contexts, see refs. [78] and [85] for two recent reviews.

It is therefore envisaged that, by focusing on conformations having a specific topological

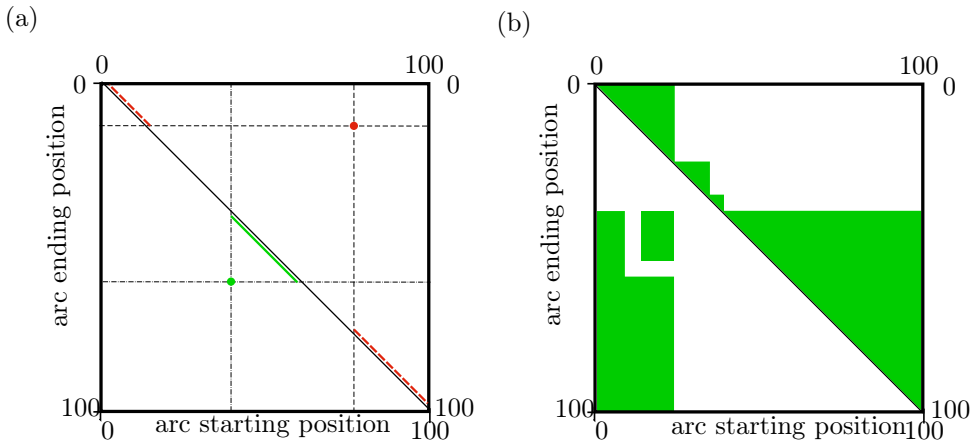

Figure 2.3: A ring of N edges is associated to $N \times N$ knot matrix. Unlike the case of open chains [58] the matrix is periodic. To each entry, i, j of the matrix is associated an oriented arc $\Gamma_{i,j}$ of the ring going from $\vec{r}_i$ to $\vec{r}_j$. This is illustrated in panel (a), where the arcs associated to the two different marked entries are highlighted on the matrix diagonal. The topological state of an arc is encoded by the color of the corresponding matrix entry. In the example shown in panel b white is used for the unknot and green for the trefoil knot. In general, although the ring has only one topology, several topologies can be assigned to different arcs of a ring. Knotted arcs with a different topology than that of the ring from which they are taken are known as *ephemeral knots*.

state (such as trefoil knots) and different degree of compactness, one might observe a very different level of geometrical complexity, i.e. local entanglement, associated to the same knot type.

We have consequently mapped in detail the topological entanglement for all subportions of three equilateral rings of $N = 100$ edges of unit length. The ring configurations are picked randomly from a pool of Monte-Carlo equilibrated structures subject to three different isotropic confining pressures. Specifically, one configuration was picked from the unconstrained ensemble (zero confining pressure), which is largely dominated by unknotted rings. The radius of the smallest sphere that is centred on the ring centre of mass and that encloses all ring vertices is $R_c = 4.8$. The second configuration has enclosing hull radius equal to $R_c = 4.1$. This hull radius is close to the value of R_c for which the probability of observing a trefoil in rings with $N = 100$ edges is maximum, see ref. [86]. The third configuration has hull radius equal to $R_c = 2.5$ and was picked at higher values of the confining pressures, where the knot spectrum was dominated by knots with topology more complex than the trefoil one.

2.2.3 Unconstrained ring

We start by discussing the knot matrices for the unconstrained ring in Fig. 2.4. From an overall visual inspection, the various knot matrices appear largely consistent and the topologies of most arcs correspond to either unknots or trefoil knots.

Yet, as it is visible in panels (b), (c), (e) and (f), a limited occurrence of complex knots, either composite knots or prime knots having more than 6 minimal crossings, is found for arcs of various lengths. These instances are manifestly ephemeral knots because their topological state differs from the global one of the ring, which is the trefoil.

Note that for this ring, all schemes are basically consistent. This fact is compatible with the finding of ref. [90] that, for unconstrained rings, the dominant knot type found with the stochastic closures with threshold $q = 50\%$ is usually the same one obtained with the direct closure scheme.

Regarding the robustness of the closure scheme in terms of the threshold, q, we report that for $q = 90\%$ about 15% of the entries are marked as undetermined knots (grey color). These undetermined arcs represent cases where the details of the closure scheme can likely yield different results. It is interesting to observe that across panels (b), (c), (e) and (f) most arcs whose topology is not the trefoil or the unknot, correspond to undetermined entries in panel (d).

It should also be noted that the direct bridging closure scheme introduces "jagged" boundaries separating the trefoil and unknotted regions. Sharper boundaries are instead found for the stochastic closure ($q = 50\%$), the radial closure and the minimally-interfering closure.

2.2.4 Spatially-confined rings

The analysis presented above was repeated for the more compact configuration depicted in Fig. 2.5.

The increased level of geometrical complexity compared to the unconstrained case is conveyed by the fact that a much larger fraction of the matrix entries ($\sim 45\%$) have an undetermined topological state according to the stochastic closure scheme with the stringent $q = 90\%$ threshold. This is because the geometrical complexity characterizing more compact structures prevents the occurrence of a single highly-dominant knot type.

A related aspect is that the knot matrix obtained with the direct bridging closure, see panel (b), is considerably noisier than the knot matrices obtained with the tolerant

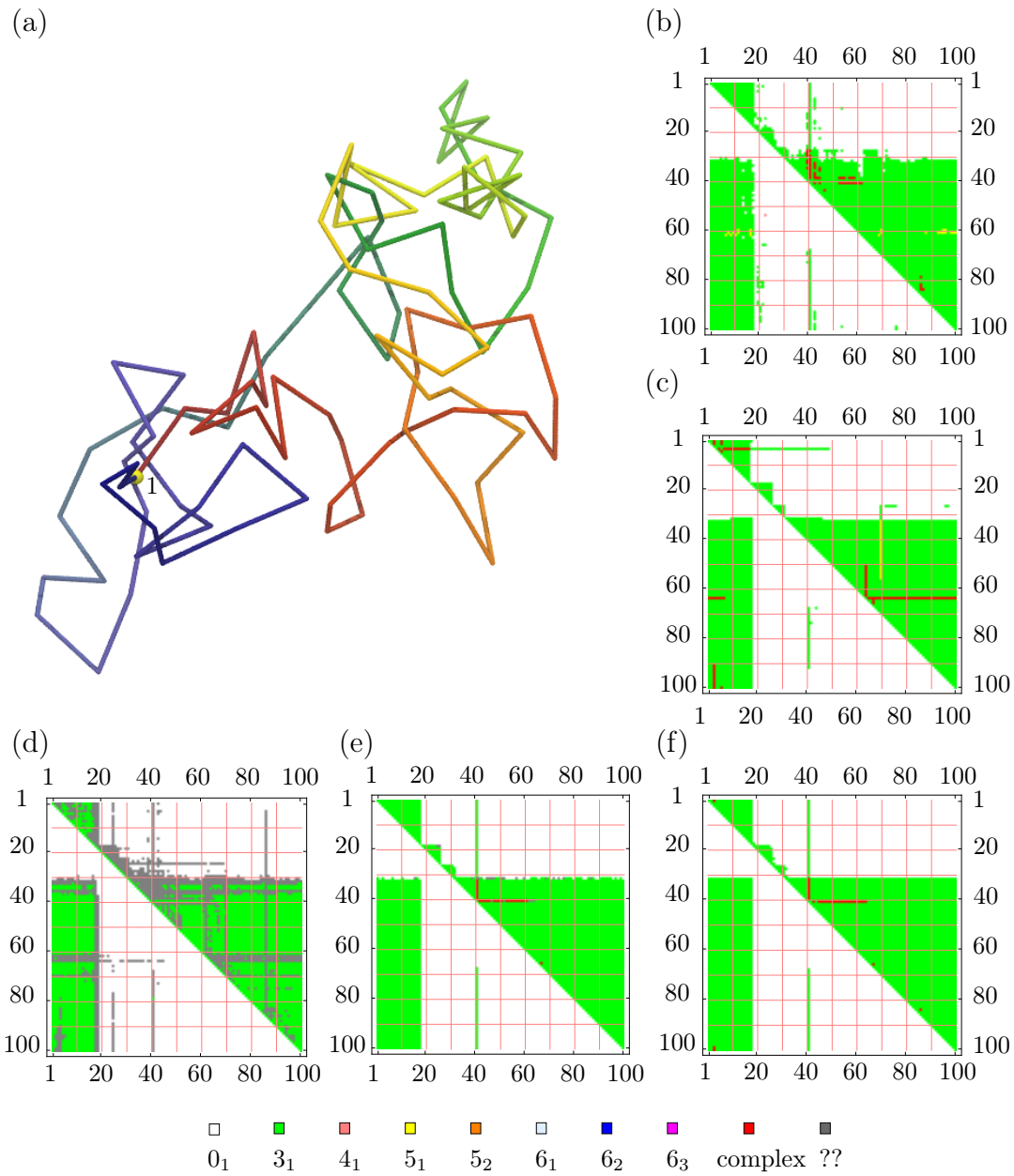

Figure 2.4: Large panel: spatially-unconstrained trefoil-knotted ring of $N = 100$ edges. The indices (numbering) of subsets of vertices are shown explicitly; the first vertex is highlighted with a yellow sphere. Other panels: knot matrices of the ring obtained by using 5 different closure schemes: (b) direct closure, (c) radial closure, stochastic closure at infinity with threshold (d) $q = 90\%$ and (e) $q = 50\%$, (f) minimally-interfering closure. Different topologies are color-coded according to the legend at the bottom.

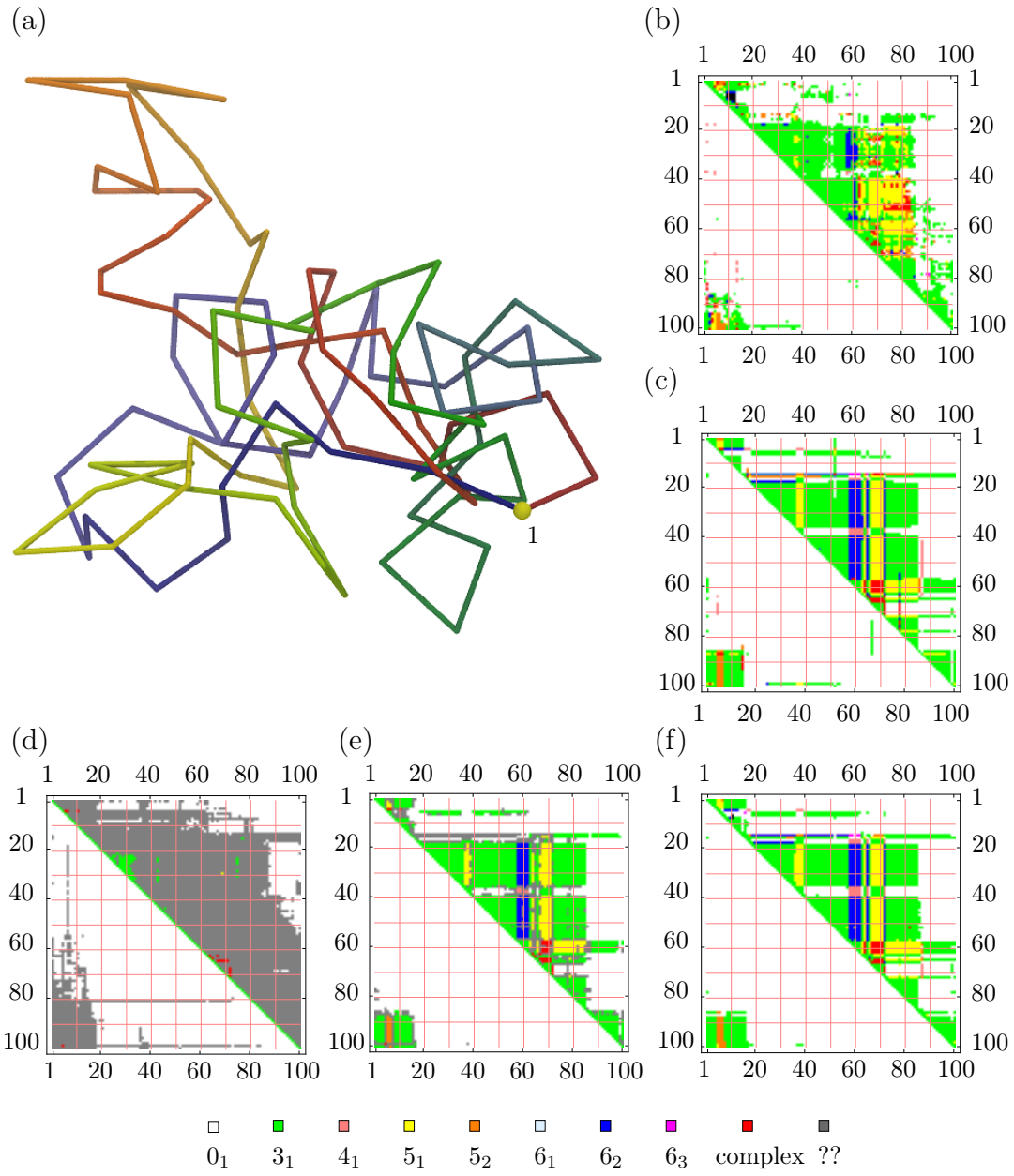

Figure 2.5: Mildly-confined trefoil-knotted ring of $N = 100$ edges (top-left panel) and associated knot matrices displayed and coloured as in Fig. 2.4.

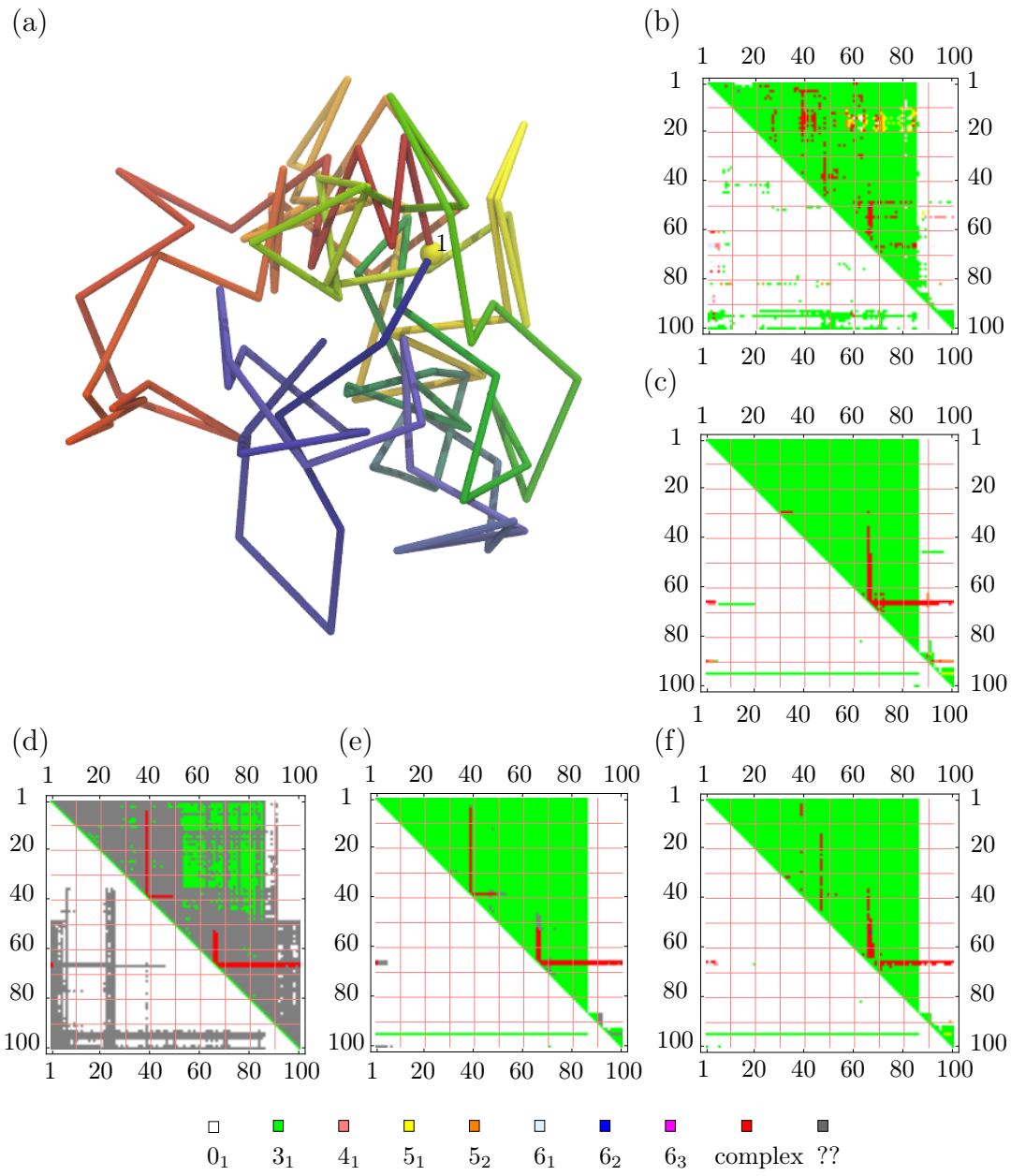

Figure 2.6: Strongly confined trefoil ring of $N = 100$ edges (top-left panel) and associated knot matrices displayed and coloured as in Fig. 2.4.

($q = 50\%$) stochastic closure the radial closure and the minimally-interfering one, see panels (c), (d) and (f).

Notably, the visual inspection of panels (d) and (f) indicates that the responses of these two methods remain highly compatible notwithstanding the increased geometrical complexity. The radial closure, while showing an acceptable agreement with the 50% stochastic closure and the minimally-interfering closure, tends to find several knotted arcs in region where the other two closure schemes only see unknotted arcs.

All the above considerations hold also for the ring with highest level of compactification shown in Fig. 2.6.

In summary, at all the three levels of compactness a high consistency is found between the tolerant stochastic closure and the minimally-interfering one. Given the different spirit of these two methods this accord is both pleasing and important, because it provides *a posteriori* confidence that a consensus indication of the topological state of various arcs of a ring can be achieved with these two different closure methods.

It is important to point out that, despite returning consistent results, these two methods are very different in terms of the computational expenditure, because the stochastic closure scheme is based on a collection of several (in our case 1000) random closures per arc, whereas only two closures per arc are involved in the minimally-interfering scheme. The latter scheme appears therefore to be preferable when one seeks to establish the local level of entanglement over a large ensemble of rings or open chains (as for large-scale surveys for detecting and locating knots in all available structures of globular proteins [58, 107].) The former, however, has the advantage of providing a quantitative control of the statistical weight associated to the dominant knot type for every arc.

2.3 Identifying the knotted portion

Locating the knot can be a highly challenging task. To start, one needs to establish the kind of entanglement "trapped" in any subportion, or arc, of the ring or chain under study, a task requiring the analysis of open knots, and then select the shortest arc whose topological state matches that of the whole chain or ring.

As we already anticipated, apart from the ambiguities arising from the definition of an open knot, there is another ambiguity in locating the knotted portion of a ring. Here we will show that the measured degree of localization of a knot depends on the way one

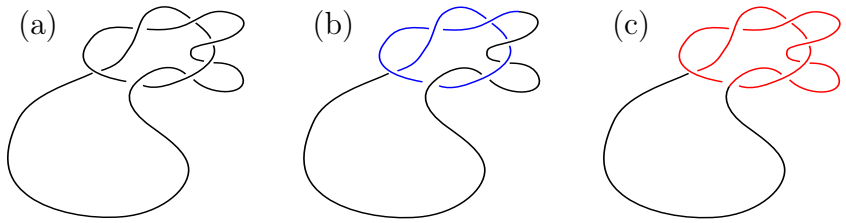

Figure 2.7: An example of how a bottom-up (b) and a top-down search (c) on the trefoil knotted arc shown in (a) give rise respectively to the shortest knotted arc (blue curve in (b)) and to the shortest C-knotted arc (red curve in (c)).

looks for the knotted portion, or equivalently on the definition of *smallest knotted portion* one implements.

2.3.1 Knot searching algorithms

A few different procedures have been proposed so far to localize the shortest knotted portion of a ring with non-trivial topology [56, 76, 73, 91]. They can be divided into two main categories depending on the strategy used to identify the "shortest knotted portion". In the first category we have those searches which start from a small unknotted arc and subsequently look for the knot in arcs of increasing length. In the second category we have those searches in which one starts by considering large knotted arcs of the ring and try to reduce their size until the knot is lost, then keep the previous to last (knotted) arc. Here we call these two approaches "bottom-up" and "top-down" respectively.

We illustrate two possible implementations of those methods, considering a trefoil knot in a ring of N vertices.

Bottom-up search The purpose is to identify the shortest portion of the ring that has the same topology of the whole ring. One starts by sorting all subportions of the ring (arcs) by increasing arc length. Arcs with the same lengths are sorted according to the index of their starting vertex. The shortest arc in the list[1] is then closed and its topology measured. If the arc's topology does not match that of the whole ring the next arc in the list is analyzed, otherwise the knot is located on the arc under analysis. We shall refer to this arc as the *shortest knotted arc* (also called "bottom-up" knotted arc in this thesis). It is important to stress that the returned shortest knotted arc may correspond

[1]No knots can be tied with less than 5 segments, so all arcs shorter than 5 segments can be safely discarded from the analysis.

to an *ephemeral knot*. These are arcs with non-trivial topology that are contained in longer arcs with a different topology (which, in turn, can be contained inside arcs with a different topology etc.) [91]. Using the alternative knot matrix of Fig. 2.8 (b) this arc corresponds to the lowest point of the matrix having the topology of the whole ring, highlighted with a red circle.

Top-down search In this case we look for the shortest knotted portion of the ring that (i) cannot be further shortened without losing the knot and (ii) can be extended continuously to encompass the whole ring. To do so, one begins by setting $l = 1$ and considers all arcs of length $N - l$ and discards those that are not trefoil-knotted. Then l is increased by one unit and, inside the survived arcs, one looks for trefoil-knotted arcs of length $N - l$. Those that are not trefoil-knotted are discarded and the procedure is repeated until at a certain value of $l = \bar{l}$ no trefoil-knotted arc is found. The trefoil-knotted arc (or arcs in case of degeneracy) that survived at the previous iteration step (the one(s) with length $N - (\bar{l} + 1)$) provides the desired ring portion accommodating the knot. We shall refer to such arc(s) as the shortest *continuously-knotted* ("top-down" knotted) portion of the ring, or shortest C-knotted portion for brevity. This portion can be located on the alternative knot matrix by looking for the lowest point which has the same topology as that of the whole ring and which can be connected to the top row with a continuous line going either down or right at every step and passing only through points having the same topology of the whole ring. The point and line are highlighted in red in Fig. 2.8 (b).

The knotted portions identified by the two procedures are not necessarily the same, as illustrated in Fig. 2.7 and Fig. 2.8 (b). From the two definitions it follows that the length of the shortest C-knotted arc cannot be smaller than that of the shortest knotted arc.

Both methods are applied and compared here and in the following, but with one important addition with respect to the procedure described above. The modification follows the observation that a satisfactory location of the trefoil knot in a specific arc, Γ_{ij}, of the ring should be accompanied by the condition that the complementary arc, Γ_{ji}, is unknotted. Therefore the test for "trefoil-knottedness" in the previous schemes, consists in the stringent requirement that upon closure Γ_{ij} is trefoil knotted *and* its complementary arc, Γ_{ji} is unknotted.

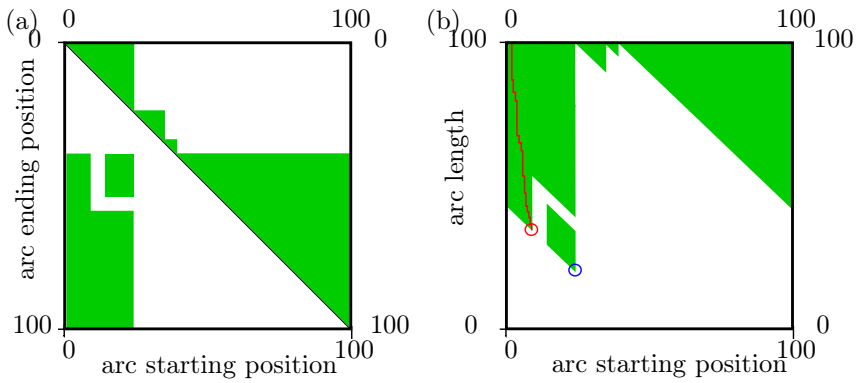

Figure 2.8: (a) An example knot matrix for a trefoil knotted ring and (b) its alternative representation where instead of mapping the starting and ending points of all arcs we map the starting point and length of the arcs. The top row correspond to the diagonal of the knot matrix in (a). The shortest knotted arc is given by the lowest point having the same topology of the whole ring (circled in blue). The shortest C-knotted arc is identified by the lowest point which has the correct topology and can be connected to the top row with a continuous curve going either down or right at every step and passing only through points having the same topology of the whole ring.

2.3.2 Knotted portions: test cases

To locate the trefoil knot within each of the three rings under analysis we processed the associated knot matrices obtained by applying the minimally-interfering closure. We use both the top-down and the bottom-up approaches to locate the knot. The results are described hereafter and reported graphically in Fig. 2.9. The application of the two algorithms on the knot matrices obtained from the tolerant stochastic closure gave practically identical results.

For the unconstrained knot, the two search methods identify the same arc, see Fig. 2.9, as the region that accommodates the knot.

This is not the case for the two more compact rings. In particular, for the ring shown in Fig. 2.5 the shortest knotted arc corresponds to $\Gamma_{87,15}$ (highlighted in blue in the figure), while the shortest C-knotted arc corresponds to the much longer arc $\Gamma_{51,16}$ shown in red.

Finally, for the most compact ring, the shortest knotted arc is found to be $\Gamma_{86,95}$, while the shortest C-knotted arc is found to be $\Gamma_{86,1}$, see Fig. 2.6. In this case the comparison between the two knot localization methods reveals a notable hierarchy of ephemeral knots. In fact, while arc $\Gamma_{86,95}$ is trefoil knotted, the longer arcs from $\Gamma_{86,96}$ up to $\Gamma_{86,99}$

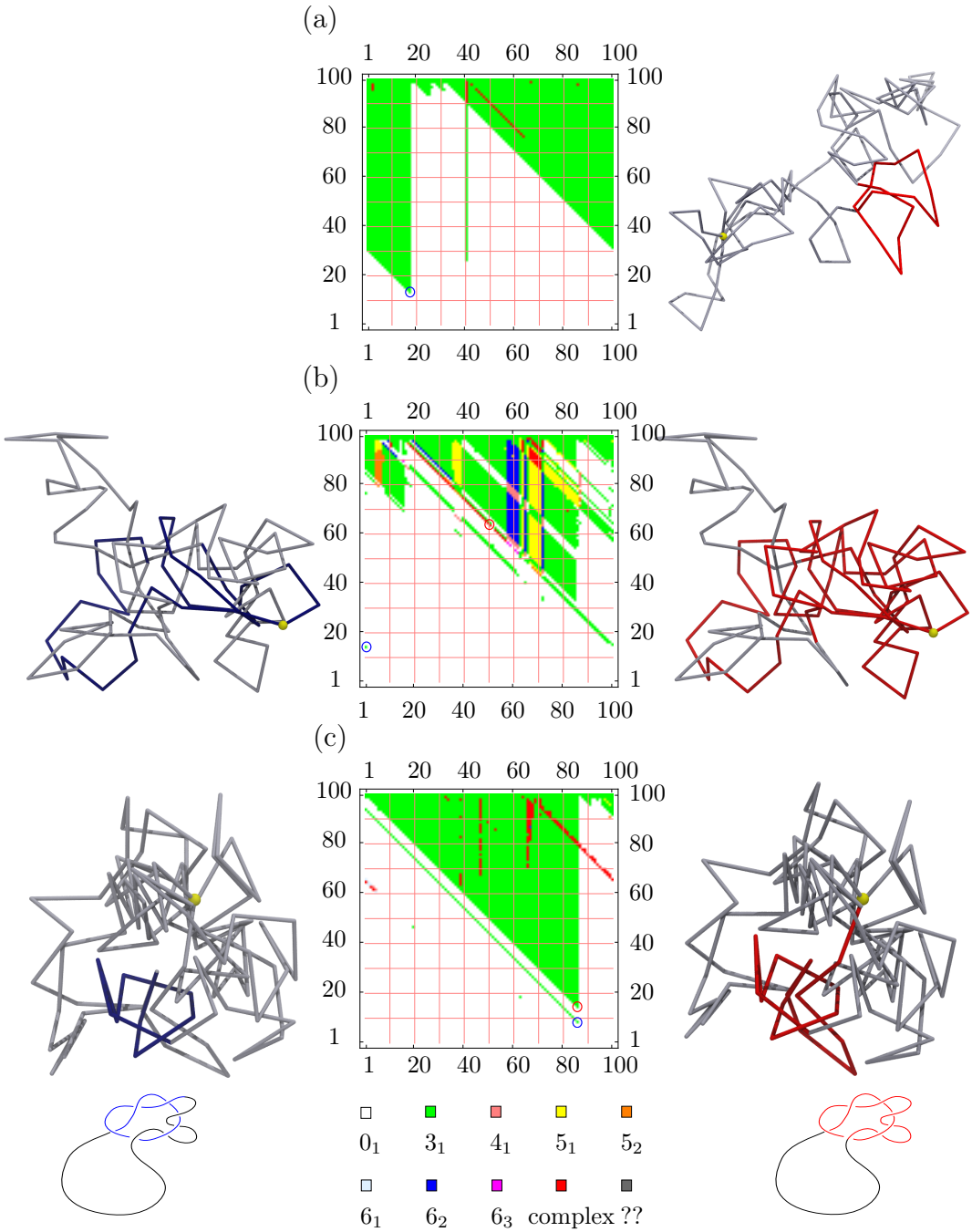

Figure 2.9: The smallest knotted portion (left column) and smallest C-knotted portion (right column) are highlighted in blue and red respectively for, (a), the unconstrained trefoil ring of Fig. 2.4, (b), the mildly confined ring of Fig. 2.5, and, (c), the strongly confined trefoil ring of Fig. 2.6. The central column reports the alternative representation of the knot matrices of the three rings. The first ring in the left column is not shown as the two knot definitions give the same result in this particular case.

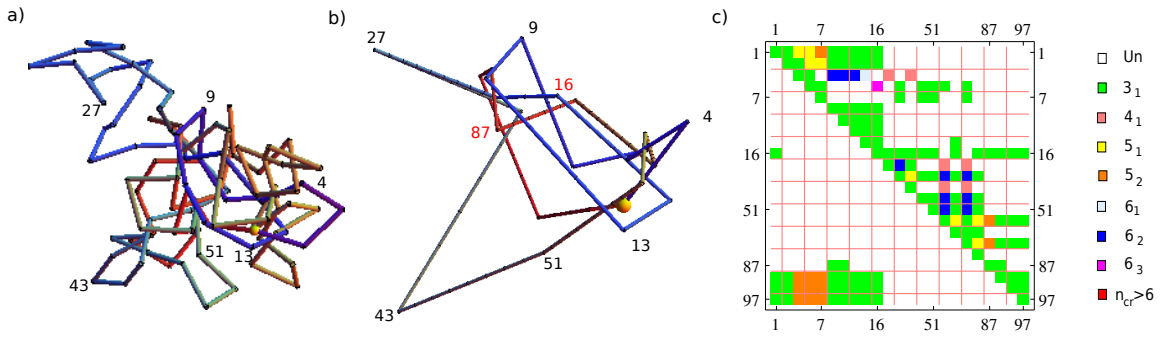

Figure 2.10: (a) Original and (b) simplified ring after the rectification procedure. The original index (numbering) of a subset of vertices is shown explicitly. The first vertex is highlighted with a yellow sphere. The knot matrix of the simplified ring is shown in panel (c). The full knot matrix of the original ring is shown in Fig. 2.5 panel (f).

are unkotted and still longer arcs, such as $\Gamma_{86,1}$, are trefoil-knotted again.

It therefore appears that the increased geometrical complexity of the rings resulting from the isotropic spatial confinement produces a non-trivial interplay of geometry and topology, which manifests in the sensitive dependence of the knot location on the search strategy that is used. The implications of this finding are discussed in particular in § 2.3.4 and in chapter 5.

2.3.3 Effect of simplification on the search for the knotted portion

In the attempt to reduce the heavy computational cost of locating the knot either in rings or linear chains, several groups have avoided the extensive topological profiling of all arcs of the ring and have instead mapped out the topology of a simplified representation of it [60, 132, 145].

The simplification, or rectification procedure entails the removal of those ring vertices which can be made collinear with their neighbouring pair along the ring through a continuous local deformation (morphing) of the ring that does not lead to any edge crossing. Such rectification operations clearly preserve the topology of the ring and can considerably reduce the number of ring vertices, and hence the linear size of the knot matrices.

Here we discuss the effect of rectification procedure on the bottom-up and top-down knot location schemes.

In order to ensure the most uniform level of simplification, we subjected each ring on N edges to several simplification rounds. At each stage of the procedure we disallow the removal of ring vertices that would introduce a gap larger than a given integer, s, in the original index of consecutive surviving beads. Because of the ring periodic boundary conditions, we employ the modulus operation on s. By starting with $s = 2$, we carry out N statistically-independent attempts at bead removal (sweep). Then s is increased by one and another sweep of vertices elimination is attempted. The procedure is carried on until no vertex can be further removed within a sweep. Notice that more beads might be removed by allowing s to increase more rapidly at each sweep, for example by doubling it. These more aggressive rectifications are not considered in the present section.

Reducing the number of beads of the ring has two distinct effects. First, the linear dimensions of the knot matrix are reduced. Second, the topological entanglement of the remaining subportions might be different from the one measured for the corresponding subportions of the original ring. Regarding the first aspect we recall that we establish the entanglement trapped in the arcs of the surviving nodes by closing the arcs with the same ends on the original, unsimplified ring. As a consequence the knot matrix of the simplified ring is a subset of the original full knot matrix, obtained by restricting to the rows and columns pertaining to the surviving ring vertices. This procedure is illustrated in Fig. 2.10.

Notice that since the simplified knot matrix is a subset of the original knot matrix, the length of the shortest knotted arc measured on the simplified ring can not be smaller than the length of the shortest knotted arc measured on the unsimplified ring. On the other hand no such reasoning can be made for the shortest C-knotted arc.

The rectification procedure clearly brings about a simplification of the geometrical complexity of the ring. As a consequence, the difference between the shortest knotted arc and shortest C-knotted arc will likely decrease after rectification but it will not be obliterated for sufficiently entangled rings. This is illustrated by the rectification of the ring with intermediate compactness, whose simplified knot matrix is shown in Fig. 2.10. The shortest knotted arc on the simplified ring goes from node 87 to node 16. The inspection of the matrix reveals that from the point $(87, 16)$, corresponding to the shortest knotted arc $\Gamma_{87,16}$, one cannot find a connected path through points corresponding to longer and longer trefoil-knotted arcs (even disregarding the unknottedness requirement

on the complementary arcs) that reaches out to the whole ring. This clarifies that $\Gamma_{87,16}$ does not correspond to the shortest C-knotted arc, and hence the two methods for knot detection do necessarily not coincide even after simplification.

2.3.4 Application to scaling analysis of knot lengths

The study of the scaling of knot length with increasing ring length is motivated by the observation that, if one fixes the topology of a knotted ring and increases its length, then the ring becomes more and more similar to an unknotted one, suggesting that the knotted portion becomes negligible compared to the rest of the ring [100, 101]. This possibility was studied directly only in recent years, mainly through numerical investigations. Let us call l_{knot} a generic length of the knotted portion. Upon increasing the ring contour length, N, three different scenarios can occur for $\langle l_{knot} \rangle$: i) $\langle l_{knot} \rangle$ increases more slowly than any power of N. In this case the knot is said to be *strongly localized*; ii) $\langle l_{knot} \rangle$ grows like N^{α} with $0 < \alpha < 1$. The knot is said to be *weakly localized*; iii) $\langle l_{knot} \rangle$ is proportional to N, the knot is said to be *delocalized*. While a complete delocalized knot can be expected to affect the ring geometrical properties independently of N, in cases i) and ii) one has that ${}^{l_{knot}}/_{N} \to 0$ with $N \to \infty$, so the knotted portion is expected to behave like a point-like decoration on the ring in the asymptotic limit.

All the studies performed up to now on loose three dimensional polymers agree that the knot is localized on the chain. Nonetheless they differ substantially both in the kind of localization found, strong [91] or weak [76, 36, 145, 73], and in the latter case in the measured exponent α. Farago et al. [36] reported $\alpha = 0.4$ for trefoil knotted polymers, Marcone et al. [76] $\alpha = 0.75$, Virnau et al. $\alpha = 0.65$ [145], Mansfield and Douglas [73] reported $\alpha = 0.54$ and Millett recently reported a bounded behaviour of $\langle l_{knot} \rangle$ in FJRs with $N \geq 500$, compatible with a strong localization of the knot. The studies [145] and [36] are somehow different from the others in that they consider knotted linear chain-of-beads polymers. In particular in [36] the value of α is obtained studying force-extension curves for a knotted polymer without using any knot location algorithm. The other studies we reported considered trefoil knotted rings and used either a top-down knot location scheme (ref. [76]) or a bottom-up knot location scheme (ref. [73, 91]) to identify the length of the knotted portion. We argue that the discrepancies in their results can be explained by the inherent difference in these two knot location schemes. To support our argument, we investigate the behaviour of the knot lengths measured by

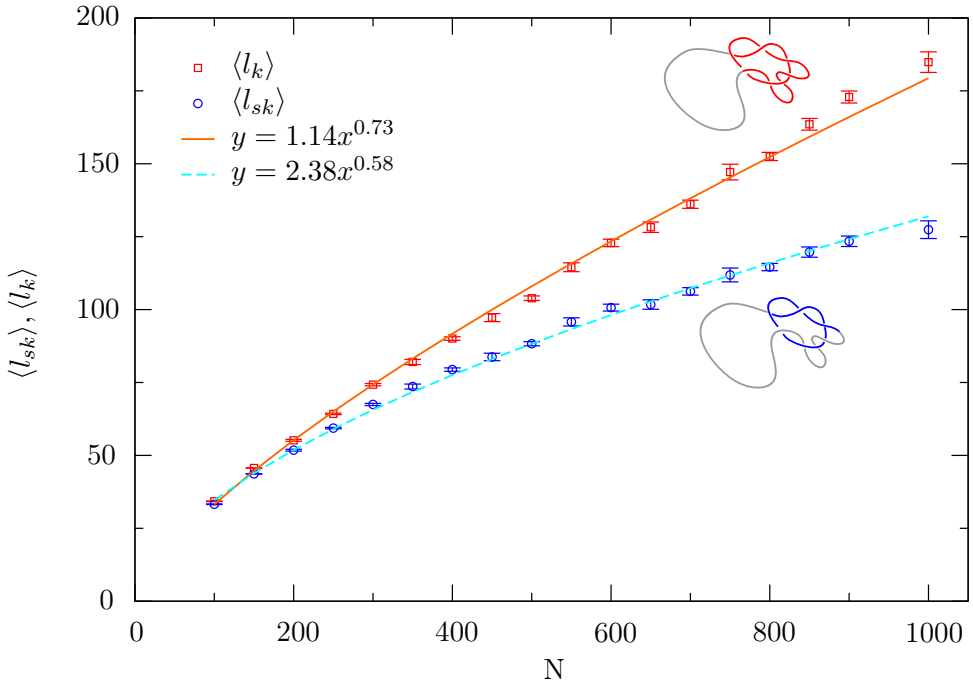

Figure 2.11: Numerical data for l_{sk} (blue circles) and l_k (red squares) and their fitting functions.

bottom-up and top-down schemes, which we will call l_{sk} and l_k from now on, for infinitely thin trefoil rings of increasing length N, up to $N = 1000$.

Trefoil rings were extracted a posteriori from a pool of FJRs using the KNOTFIND routine implemented in the KNOTSCAPE package [47]. The KNOTFIND routine efficiently simplifies the diagrammatic representation of a knot and compares it against a look-up table of diagrams of prime knots with less than 17 minimal crossings. When a positive match is found, the topological state of the ring is unambiguously established. If no match is found (due to genuine excessive complexity of the knot or to insufficient classification) the topological state is regarded as undetermined.

In order to reduce the computational time required by the knot location algorithms, we used the simplification procedure described in § 2.3.3. Simplified rings were about $\simeq 20$ edges long. Our results, presented in Fig. 2.11, clearly show that while both l_{sk} and l_k grow like N^α, with $0 < \alpha < 1$, they diverge with increasing N. A fit of the data with fitting function $y = cx^\alpha$ gives $\alpha = 0.58 \pm 0.01$ for l_{sk} and $\alpha = 0.73 \pm 0.01$ for l_k. Although we do not aspire to give definite values for α, it is interesting to compare our values with previously obtained ones. The scaling exponent we obtain for l_k is in good agreement

with the one obtained by Marcone et al. [76], who used a conceptually similar method. As for l_{sk}, we do not observe any plateau, contrary to what observed in [91]. We think that this difference can be due to the fact that we used a stronger condition than previous studies to check the knottedness of a ring portion, by requiring that the complementary arc of the knotted portion must remain unknotted. Without this further requirement it is easier to exchange ephemerally knotted arcs for the "genuine" knotted portion of the ring. Given the nature of the bottom-up scheme this results in smaller length being measured. It must be noted that the other study using bottom-up approach [73] did not find any plateau for l_{knot}, and the authors report a value $\alpha = 0.54$, which is more compatible with our results than with those of [91]. We think this is due to the fact that the authors of that study, in locating knots, considered only arcs of the rings which had both ends near the surface of a ball enveloping the ring. This was done in order to avoid considering ambiguous knots and could in fact avoid measuring ephemeral knots as well.

Chapter 3

Mutual entanglement of prime components in composite knots

As we saw in 1.1.3 several knots can be tied on the same rope or ring, resulting in a composite knot. This is indeed what happens in sufficiently long polymers. Increasing the polymers length the knot spectrum gets dominated by composite knots to the point that prime knots are exponentially rare [131]. Despite their ubiquity, only few studies so far were dedicated to investigate the characteristics of composite knots more complex than the simplest ones, $3_1\#3_1$ and $3_1\#4_1$ [137, 55, 101, 82, 43, 11, 88]. The main result from these studies is that for three dimensional rings, following the weak localization of prime knots (see § 2.3.4), every prime component of a composite knot becomes localized, so that for asymptotically large chain lengths all prime components behave like independent point-like decorations on the ring (see Fig. 3.1 (f)). As a consequence, the asymptotic properties of composite knots should merely depend on the number of prime components (factor knots) by which they are formed [101, 82, 43, 11].

Here we investigate how this factorization into independent separate prime components is reached for increasing ring length and how one can describe the behaviour of composite knots before this factorization takes place. Do the geometric characteristics of relatively short knots, like their lenghts and their distribution along the ring, depend on the number of knots tied on the ring or their relative distance? This is a relevant question to understand whether specific polymeric and biopolymeric systems of known length should be considered as a series of independent prime knots or if it will be necessary to account for the mutual entanglement and possibly interaction of different factor knots.

In order to have a simple reference system, we model our knotted rings as equilateral freely jointed rings (FJRs), as we did in§ 2.3.4 to study knot length scaling behaviour.We study composite knots with $2, 3$ and 4 prime components. Using the tools introduced

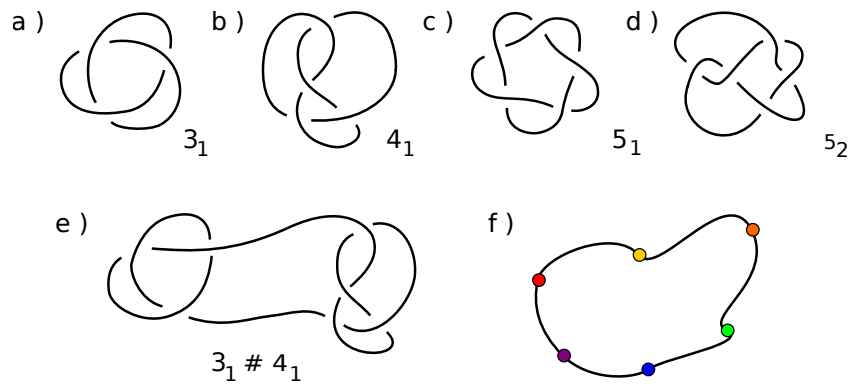

Figure 3.1: Prime knots considered in this work. (a) 3_1, (b) 4_1, (c) 5_1, (d) 5_2. Panel (e) shows a simple composite knot with two components, $3_1 4_1$. (f) In the limit of infinite length all component are expected to localize and behave like independent point like decorations along the ring.

in chapter 2 we are able to identify the factor knots and investigate their geometric properties like their linear dimension, disposition along the ring and mutual entanglement. In particular we are able to characterize the frequency with which composite knots are found with all their prime components separate along the ring as a function of ring length. We find that at ring lengths where the composite knots we study dominate the knot spectrum, there is not a complete factorization into separate prime components. Even for the simplest composite knot, $3_1\#3_1$ we find that the probability of having two or more prime components entangled with each other is at least $\simeq 10\%$ in the range of ring lengths considered, which spans rings of length up to two order of magnitude greater than the typical (most probably) knot length of a trefoil ring.

Finally, we show that the above mentionend results can be qualitatively reproduced using a transparent one dimensional model, in which factor knots are substituted by randomly arranged paraknots (loops on a ring formed by a sliplink [82, 83]) having lengths sampled from the knot length distribution of their corresponding *prime* knots. The agreement between this simple model and simulations suggest that the properties of composite knots follow a simple statistic even in absence of a complete factorization into separate prime components.

3.1 Simulation: model and methods

3.1.1 Chain model

We generate Freely Jointed Rings of contour length $N = 100, 200, \ldots, 1000$ using the crankshaft rotation algorithm [4]. For every contour length N we generated $\simeq 10^7$ independent configurations without constraining ring topology.

As reported in Fig. 3.2 the range of lengths considered spans the crossover from a knot spectrum dominated by prime knots to one dominated by composite knots. In this chain model composite knots starts to dominate for $N \simeq 400$. From the figure it is evident how the spectrum of composite knots is dominated by knots with 2, 3 and 4 components in the range of length we consider. As composite knots formed by the simplest prime knots 3_1, 4_1, 5_1 and 5_2 dominate the spectrum we focused on the following topologies: $3_1 3_1$, $3_1 4_1$, $3_1 5_1$, $3_1 5_2$, $3_1 3_1 3_1$, $3_1 3_1 4_1$, $3_1 3_1 5_1$, $3_1 3_1 5_2$, $3_1 3_1 3_1 3_1$, $3_1 3_1 3_1 4_1$ (here and in the following we have dropped the # to ease the notation). As in § 2.3.4 we used the KNOTFIND routine implemented in KNOTSCAPE [47] to extract rings with the desired topologies. For every topology and every value of N we collected several hundreds to thousands of independent configurations.

3.1.2 Identification of separate prime-knotted components

Let us consider a rope with n knots tied on it. Intuitively we can say that a knot is "separate" from all the others if we can cut it away from the rope and join the rope back together leaving the others $n-1$ knots unchanged. In analyzing composite knots we want to implement the same procedure numerically. We start by identifying the portion of the ring which accommodates the whole composite knot (shown in green in Fig. 3.3 (a), (b), and (c)). In this region we look for those factor knots which can be "cut away" without changing the topology of the others $n-1$ factor knots. So in the example of Fig. 3.3 (a) our scheme identifies two prime factor knots, in (b) one factor knot, and in (c) zero as the two factor knots are too intermingled with each other to be distinguishable.

To assign a topological state to open arcs we close them using the minimally-interfering closure introduced in 2.1 and analyze their topology using the Alexander determinants $\Delta(-1)$ and $\Delta(-2)$.

We consider a factor knot of topology τ_i of a composite knot of topology $\tau_{comp} = \tau_1 \ldots \tau_{i-1}\tau_i\tau_{i+1} \ldots \tau_n$ to be separate from the others if we can identify an arc of the ring

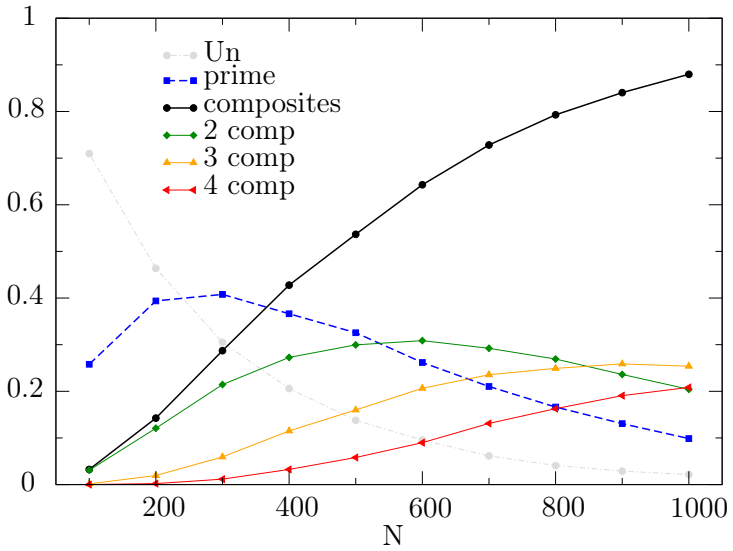

Figure 3.2: Probabilities of composite knots and prime knots for increasing length of the rings, measured using KNOTFIND. Curves for composite knots with different number of components are reported as well. Note that the probability curve of composite knots is not exponential. This can be ascribed to the fact that with increasing ring length also the fraction of knots which are too complex to be identified by KNOTFIND increases. We can expect many of those unidentified knots to be composite.

such that its topology is measured to be τ_i while its complementary arc on the ring has topology $\tau_{comp} \setminus \tau_i = \tau_1 \dots \tau_{i-1}\tau_{i+1} \dots \tau_n$. Fig. 3.3 (c) shows an example configuration in which two factor knots are entangled to the point that it is not possible to find two arcs satisfying the two conditions which characterize a separate prime component.

We look for separate factor knots only inside the knotted portion. The ring portion accommodating the composite knot is identified using the bottom-up approach described in 2.3 To identify all separate factor knots we proceed in the following way: we begin by ordering all the subarcs of the knotted arc for increasing length. Then, starting from the shortest arc we check if it is a prime factor knot of the composite knot. If this is the case and an arc is found to accommodate a factor knot, all the arcs overlapping it are removed from the list of arcs to be analyzed. This guarantees that in a situation like that depicted in Fig. 3.3 (b) only one component is seen as separate, while the larger one is discarded as it includes the smaller knot and therefore can not be removed without removing the other knot along with it.

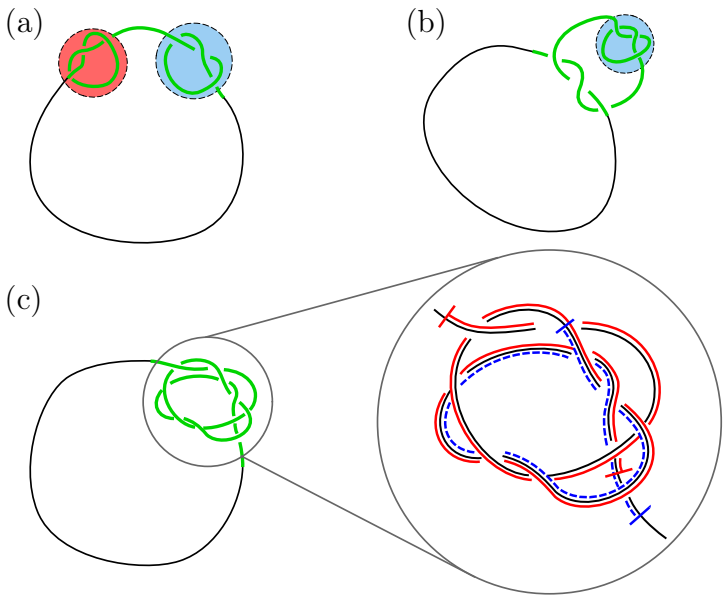

Figure 3.3: (a) A $3_1 3_1$ with both factor knots separate. (b) A $3_1 3_1$ knot with one factor knot included inside the other. Since we look for factor knots only inside the ring portion accommodating the composite knot (marked in green) we find only one separate prime component. (c) A configuration with both factor knots so entangled that they can not be separated from one another. The magnification on the right shows that it is not possible to close the red component without unknotting the blue one and vice versa. The length of the composite knot is shown in green in panels (a), (b), (c).

Ring simplification

In order to reduce both the computational cost of locating the knots and the incidence of ephemeral knots (see chapter 2), we apply the topology-preserving simplification procedure described in 2.3.3. This procedure has the advantage that it allows a fine tuning of the simplification stride, s, by bounding the maximum distance allowed between two remaining vertices on the simplified chain. The greater the stride, the faster the analysis, but the poorer its geometrical accuracy. While this inaccuracy is of no much importance when studying the statistical properties of prime knots, it can not be overlooked when trying to distinguish factor knots tied on the same ring, as the simplification may often result in an aliasing effect. In order to compromise between the time required to complete the analysis and its accuracy we impose a maximum stride $s_{max} = 15$, which is comparable to the characteristic length of trefoil knots on FJR [73] (see also Fig. 3.9). The effects of ring simplification on the results are further discussed in § 3.2.3.

3.2 Simulation Results

3.2.1 Probability of factorization into separate prime components

Based on the fact that knots become localized for long chains we expect a progressive factorization of composite knots into separate prime factor knots. To investigate whether and to what extent this factorization sets in with increasing ring length N, we study the probability, $P_{sep}^{\tau_{comp}}$, of having all factor knots of a composite knot separate along the chain as a function of the ring length N. We estimate $P_{sep}^{\tau_{comp}}$ as the ratio between the number of configurations of topology τ_{comp} in which all factor knots have been identified and the total number of configurations of that topology. Results are plot in Fig. 3.4 as a function of N and show that for every fixed topology the probability of having two or more factor knots mutually entangled, $1 - P_{sep}^{\tau_{comp}}$, is not negligible for all composite knots in the length range we investigated. Taking into account the knot spectrum of Fig. 3.2, this result suggests that composite knots taken from an equilibrium sample of rings in good solvent will not show a complete factorization into separate prime components. This is arguably due to the fact that knot length distributions of prime knots, although being peaked around $l_k \simeq 10$ independently of N, have very long tails which give origin

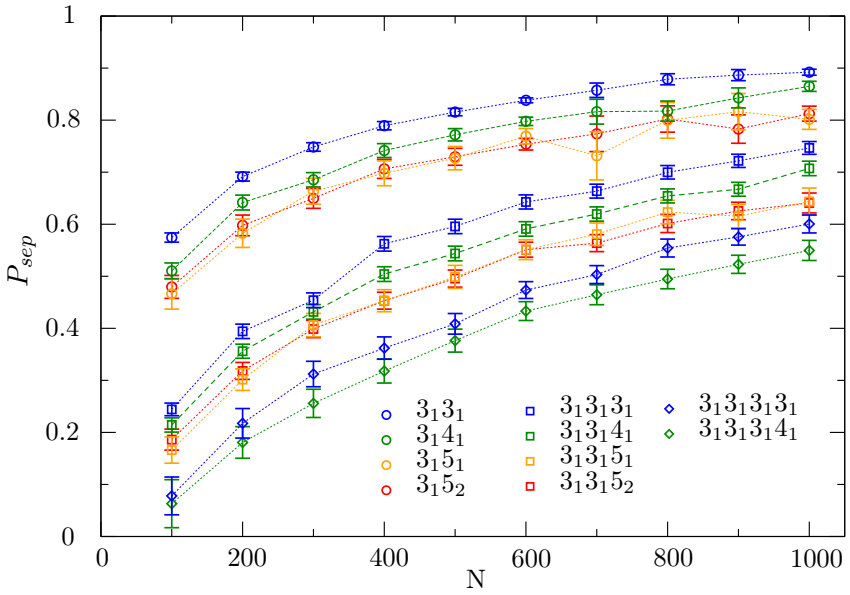

Figure 3.4: Probabilities of configurations with all components being isolated as a function of ring length N for different topologies and number of components.

to the sublinear growth of the average knot length with N (see Fig. 3.9 for an example).

From Fig. 3.4 is also clear that the probability of having all factor knots separate depends on their minimum crossing number, as there is no difference in the probabilities involving either a 5_1 or a 5_2 factor knot.

3.2.2 Knot lengths

Looking at the average length of single factor knots $\langle l_k \rangle$, reported in fig 3.5 (a), we observe that factor knots size is influenced by the number of factor knots on the whole range of ring length considered. Even the average length of factor knots in a $3_1 3_1$ knot is still lower than that of a prime 3_1 knot, while in the asymptotic limit one would expect the length of factor knots to be independent of their number.

We now characterize the average total knot length of the composite knot, $\langle l_k^{comp} \rangle$, which is the length of the shortest portion of the ring including all the factor knots. As reported in Fig. 3.5 (b) $\langle l_k^{comp} \rangle$ grows linearly in N, as expected if the knots were random point-like decorations on the rings. The slopes of the fitting lines are reported in table 3.1. Although their values are not strictly compatible within the given errors, they seem to depend basically on the number of factor knots forming the composite knots. If

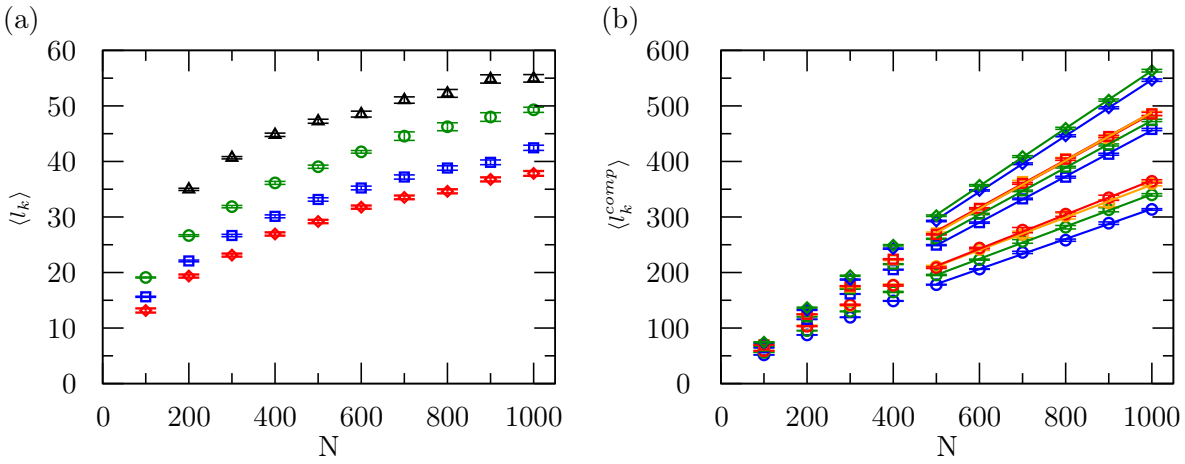

Figure 3.5: (a) From top to bottom, average knot lengths l_k of prime trefoil knots and of trefoil factor knots in knot with 2, 3 and 4 components. The average is computed only on isolated components. (b) From top to bottom, average lengths $\langle l_k^{comp} \rangle$ of composite knots with 4, 3 and 2 components. Knots composed only of trefoils are reported in blue, knots including a 4_1 factor in green, a 5_1 factor in orange and a 5_2 factor in red. Lines correspond to linear regression for $N > 400$.

the knots were point-like decorations on the ring, the knot length $\langle l_k^{comp} \rangle$ would be given by the largest arc containing all the points. The expectation value of this knot length can be computed analytically and it results to be $\bar{l}_{2points} = 1/4L$, $\bar{l}_{3points} = 7/18L$ and $\bar{l}_{4points} = 23/48L$ for two, three and four points placed randomly on a circle of contour length L. The slopes obtained from our simulations are larger than those factors, showing that finite size effects are still important in the range of ring lengths considered.

The linear growth of $\langle l_k^{comp} \rangle$ with N is compatible with factor knots being randomly distributed along the ring. There is still the possibility that when two factor knots come close to each other they feel the presence of the other knot. If this is the case, we expect that its effects will be visible in the distribution of factor knot lengths at different separations of two factor knots along the chain. Factor knots could for example exchange length when they come close to each other or feel some repulsion due to the topological interaction of their loops. To investigate such effects we consider those configurations in which all factor knots are separate. Going clockwise along the ring, for every couple of adjacent factor knots we compute their separation along the ring s^{AB}, from the ending point of one knot to the starting point of the next one and the sum of their knot lengths $l_k^{AB} = l_k^A + l_k^B$. We then average all lengths l_k^{AB} over bins of length 10 in s^{AB} to observe

Table 3.1: Slopes of lines fitting $\langle l_k^{comp} \rangle (N)$ [a]

Topology	Slope
$3_1 3_1$	0.271 ± 0.005
$3_1 4_1$	0.290 ± 0.004
$3_1 5_1$	0.294 ± 0.006
$3_1 5_2$	0.308 ± 0.006
$3_1 3_1 3_1$	0.414 ± 0.003
$3_1 3_1 4_1$	0.423 ± 0.003
$3_1 3_1 5_1$	0.427 ± 0.008
$3_1 3_1 5_2$	0.433 ± 0.006
$3_1 3_1 3_1 3_1$	0.504 ± 0.004
$3_1 3_1 3_1 4_1$	0.519 ± 0.003

[a] Fits obtained by linear regression for $N \geq 500$. The correlation coefficient is $\simeq 0.999$ for all fitting lines.

if the average knot length of two adjacent components depends on their separation. The results for rings of length $N = 1000$ are shown in Fig. 3.6. From them we can see that going from small separations s^{AB} to large separations, the length $< l_k^{AB} >$ has at first a pronunciated peak, followed by a mild decrease which becomes more pronunciated when $s^{AB} \to N$. This may be explained simply by the fact that large knots must stay closer to each other than small knots, as in both cases the total length of the ring is the same.

3.2.3 Effects of ring simplification

As we pointed out in 3.1.2, the simplification procedure, unavoidable from a computational point of view, may introduce systematic errors in the quantities we measure. To obtain an estimation of such errors we repeated the previous analysis with maximum stride $s_{max} = 4$ and $s_{max} = \infty$ on small sets of hundreds of configurations for each topology and ring length. Comparing the results we obtain for $s_{max} = 4$ and $s_{max} = \infty$ with those obtained in 3.2.1 and 3.2.2, we see that increasing simplification stride introduces a systematic effect in the measured probabilities $P_{sep}^{\tau_{comp}}$ and in the knot length of the factor knots, but not on the lengths of the total composite knots, which remain compatible within the errors.

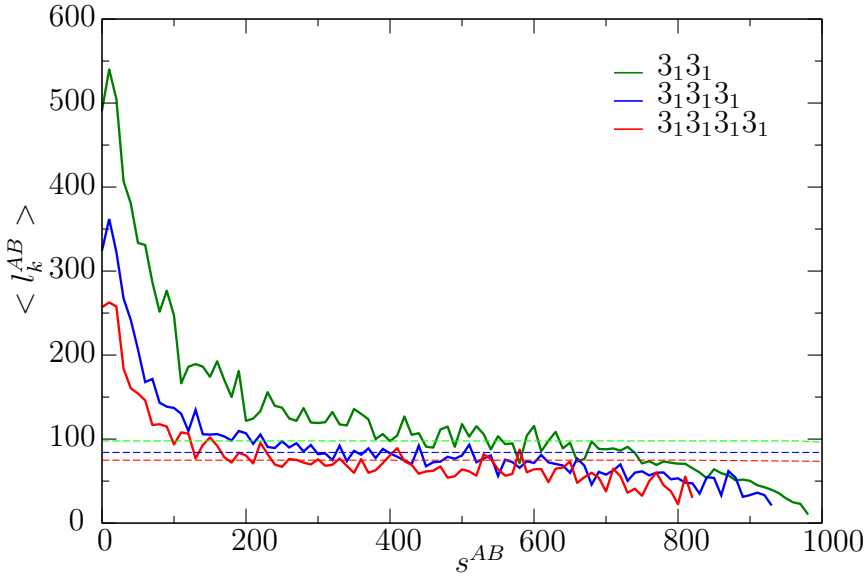

Figure 3.6: Average total length of two factor knots $< l_k^{AB} >$ as a function of their separation s^{AB} along the ring for three different composite knots on rings with $N = 1000$ edges. Horizontal dashed lines correspond to the values $2 * \langle l_k \rangle$ reported in Fig. 3.5

In the case of the $P_{sep}^{\tau_{comp}}$ we see from Fig. 3.7 that an increasing simplification stride lowers the measured probabilities, but the maximum error is $\simeq 10\%$ for $3_1 3_1 3_1 3_1$. As for the length of the factor knots, higher simplification stride results in larger lengths being measured, the total error between measures obtained with $s_{max} = 4$ and $s_{max} = 15$ being on the order of a few ring edges.

3.3 Insight from a one-dimensional model

We now show how the previous results can be interpreted with the aid of a transparent one-dimensional model, based on the following assumptions.

1. Entangled configurations like the one depicted in Fig. 3.3 (c) are very rare and, to a first approximation, can be neglected. With this approximation, two factor knots can only be either separate on the ring or nested. (see Fig. 3.8 (a)).

2. The probability that a factor knot τ has length l_k depends on the presence of other knots only through the imposition of the previous condition, which sets an upper bound on possible knot lengths. In sufficiently long rings the length

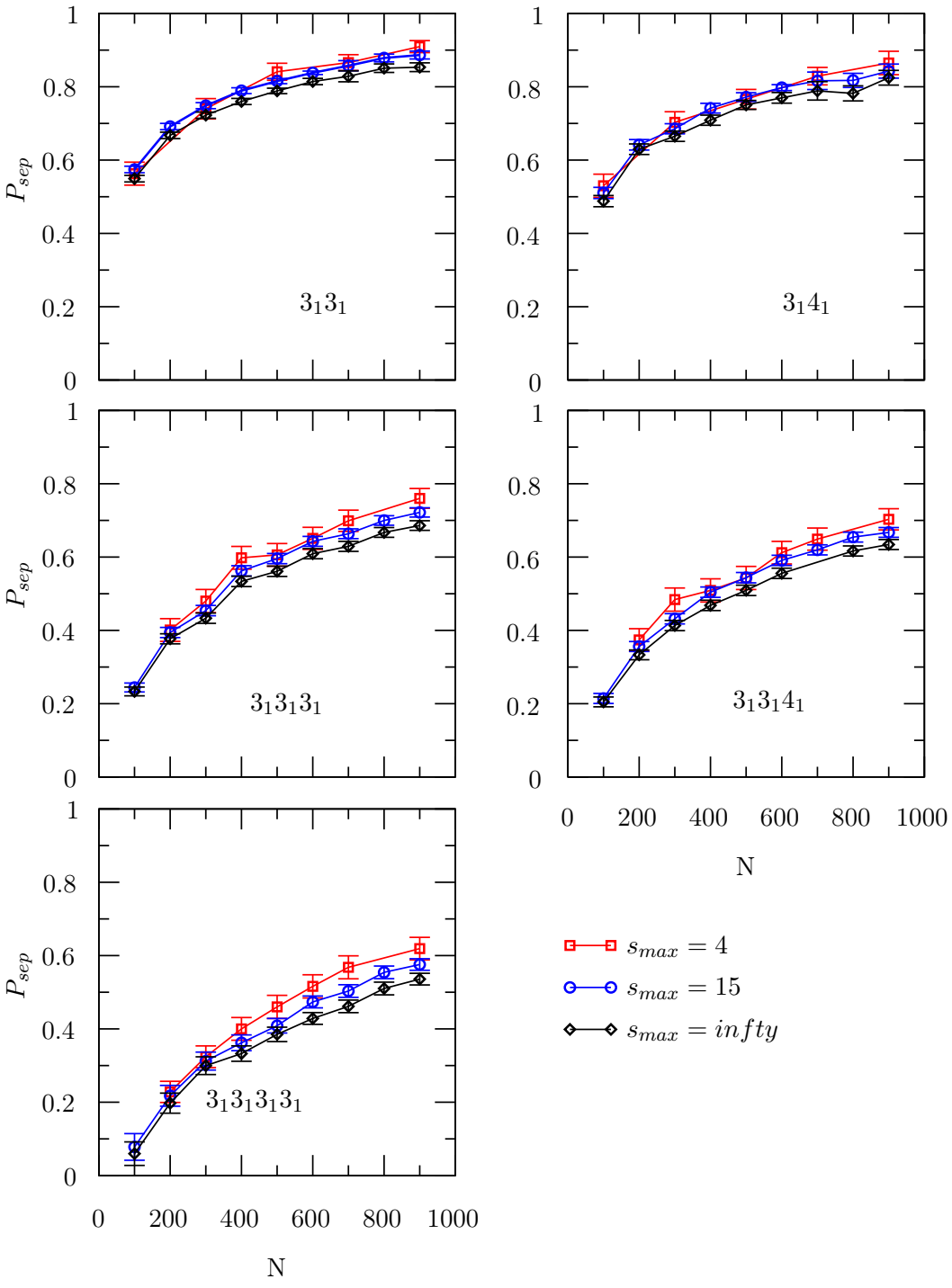

Figure 3.7: Different measures of P_{sep} done on smaller sets of configurations with different simplification strides. The difference between the probabilities measured with different strides increases with the number of factor knots, but remains between $\simeq 10\%$.

distribution of factor knots can be considered to be practically identical to that of their corresponding prime knots.

3. All factor knots are placed randomly on the ring.

According to the first assumption we describe factor knots as paraknots. Each paraknot is identified by a sliplink placed on the ring, joining two distant vertices of it. Every sliplink identifies a loop. No sliplink can be placed so to join a point inside a paraknot with one outside it. Configurations like that depicted in the bottom row of Fig.3.8 are therefore forbidden. According to our second hypothesis, we impose the length distribution of those paraknots to be the same as that of the prime knots they model.

3.3.1 1D model implementation

As 3_1 and 4_1 prime knots are those for which we have more statistics, we consider the topologies 3_13_1, 3_14_1, $3_13_13_1$, $3_13_14_1$, $3_13_13_13_1$ and $3_13_13_14_1$. We use the bottom-up knot location scheme to compute the empirical knot length distributions, $P(l_{sk}, N)$, of prime knots 3_1 and 4_1 extracted from the pool of FJRs (see Fig. 3.9).

Starting from the empirical knot length distributions we proceed as follow to generate paraknots configurations with n paraknots on a polygon with N edges. First we pick randomly n edges of the polygon. Those points correspond to the starting points of the arcs which represent paraknots (in a clockwise direction). To every starting point we associate a length picked randomly from the length distribution $P(l_{sk}, N)$ of the corresponding factor knot (3_1 or 4_1) and compute the ending points of the arcs, taking into account the periodicity of the polygon. Finally, all configurations in which two or more arcs overlap without one being strictly included into the other are rejected as they cannot correspond to a paraknots configuration (see for example bottom row of Fig. 3.8).

Analysis in the 1D model

For each topology and ring length we generate several thousands paraknots configurations. On these configurations we perform the same analysis we performed on the data from the simulation.

To identify the knotted portion of the polygon occupied by the "composite knot" in the one dimensional model we consider that by definition all topological entanglement reside in the sliplinks. A polygon with n sliplinks placed on it is therefore divided in $2n$

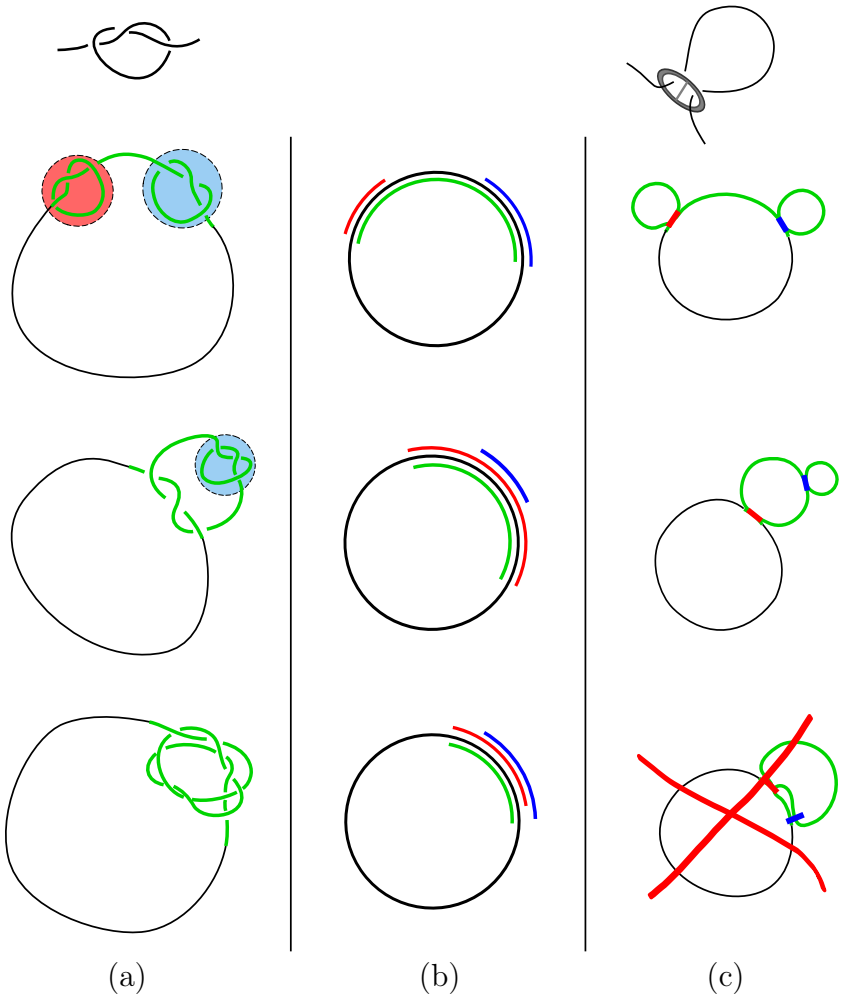

Figure 3.8: Column (a): from top to bottom, the composite knots with two, one and zero isolated components shown also in Fig. 3.3. Column (b): equivalent configurations of random arcs placed on a polygon. Column (c): paraknots configurations equivalent to the knot configurations of column (a), obtained from the random arcs model by rejecting all configurations where two arcs overlaps without one being included into the others. Configurations with no isolated components are therefore forbidden.

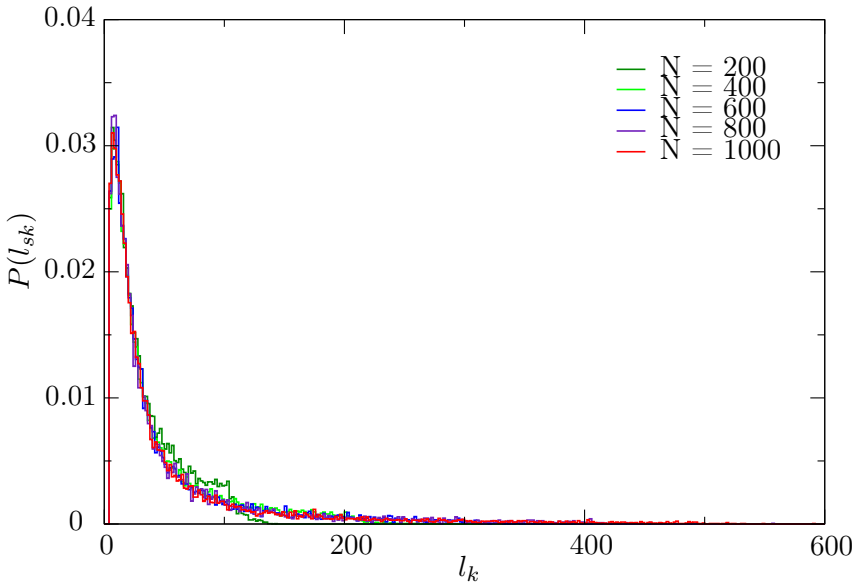

Figure 3.9: Knot length distribution for trefoil knots tied on rings of increasing length N. Note that all distributions are peaked on the same value $l_k \simeq 10$ while they differ because of their tails.

unknotted arcs (see for example Fig. 3.8 (c)). The knotted portion is the complement of the longest of such arcs. This knotted portion does not necessarily include all the paraknots (for example when the longest arc is a loop identified by one of the paraknots). In the so identified knotted region we count as isolated those paraknots which do not include any other paraknot.

3.3.2 Comparison with simulations

We now compare the results obtained from our one dimensional model with those reported in § 3.2. For the case of the probability of having all factor knots separate along the chain, P_{sep}, reported in Fig. 3.10, we observe that there is qualitative agreement with the simulation, while the differences between the results from simulations and those from the model differ by a quantity comparable to the estimated systematic error induced by the simplification procedure. We observe the same kind of qualitative agreement for the lengths of the single factor knots, reported in Fig.3.11 (a). While in the case of P_{sep} the quantities obtained from the model are systematically higher than those obtained from simulations, in the case of the length of factor knots they are systematically lower. This is compatible with a systematic error in the simulation data due to the simplification

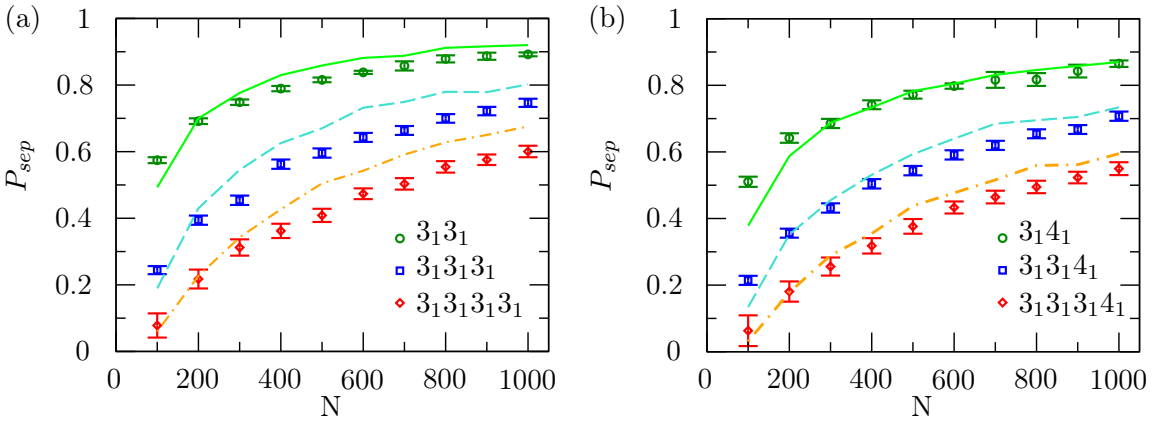

Figure 3.10: Comparison between the probabilities P_{sep} obtained from the simulations (points) and from the 1D model (lines) for composite knots made only of 3_1 knots (a) and composite knots including a 4_1 factor (b).

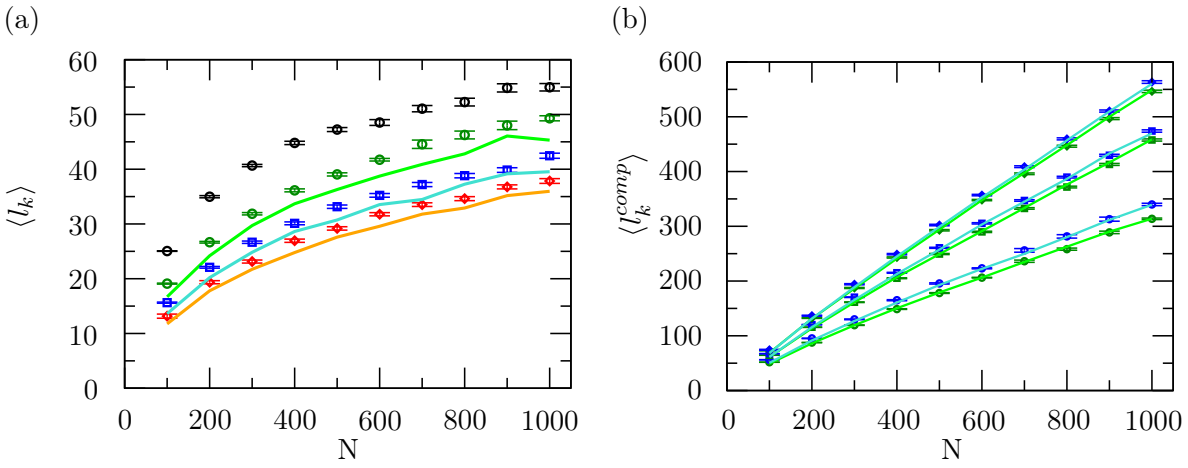

Figure 3.11: Comparison between results from simulations (points) and 1D model (lines). (a) Length of factor knots l_k. (b) Total length of composite knots, $\langle l_k^{comp} \rangle$.

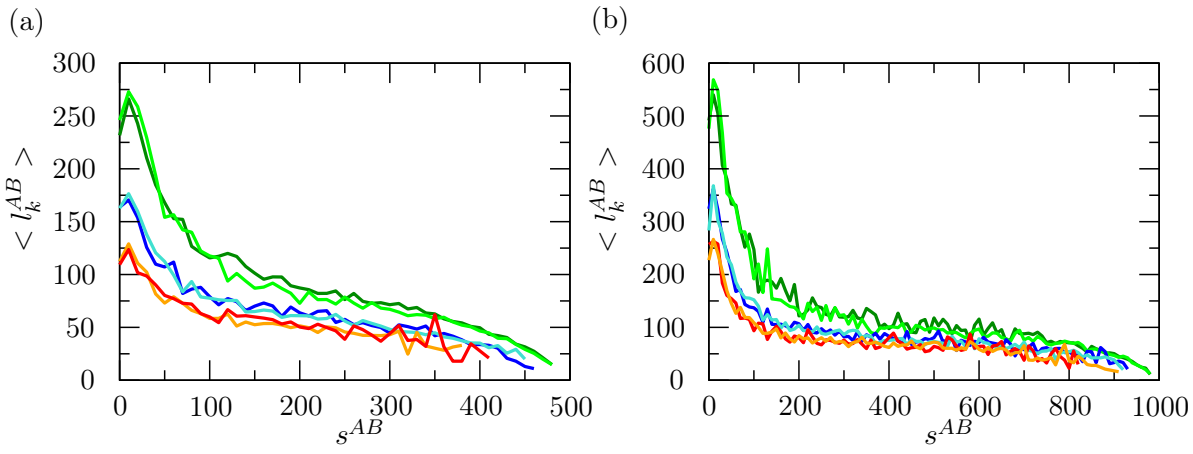

Figure 3.12: Comparison between simulation and 1D model for the distribution of total knot length $\langle l_k^{AB} \rangle$ of couples of adjacent factor knots separate by a distance s^{AB} along the ring, for rings of length $N = 500$ (a) and $N = 1000$ (b). Green, blue and red lines report simulation data for $3_1 3_1$, $3_1 3_1 3_1$, $3_1 3_1 3_1 3_1$ topologies. Light green, cyan and orange lines report data for the same topologies obtained from the model.

procedure. Indeed the simplification procedure results indeed in a slight overestimation of the lengths of knots. Consequently two factor knots which are very close to each other along the chain may be seen as not being separate, lowering P_{sep}. The underestimation is expected to increase for increasing number of components, as observed in Fig. 3.10.

The agreement between our model and simulation data becomes quantitative when we compare the average length of the whole composite knots, $\langle l_k^{comp} \rangle$ (see Fig. 3.11 (b)) and the distribution of total factor knots lengths, $\langle l_k^{AB} \rangle$, as a function of the linear separation between adjacent couple of factor knots, s_{AB}, see Fig. 3.12. These quantities are less influenced by the simplification procedure.

3.4 Summary

In this chapter we saw that a complete factorization of a composite knot into separate prime components is not to be expected for the range of lengths considered. Taking into account the knot spectrum of Fig. 3.2, we suggest that the same behaviour observed here can be expected in general for composite knots extracted from an equilibrium population of ring polymers circularized in good solvent. This is because with increasing ring length, composite knots with an increasing number of prime components dominate the knot

spectrum, and as we saw from Fig. 3.4, the probability $P_{sep}(N)$ decreases with the number of prime components tied on a ring of length N.

We observed that several characteristics of composite knots are still compatible with a random placement of their prime factor knots along the ring. Starting from this observation we rationalized the simulation results using a simple one-dimensional model, in which factor knots are substituted with paraknots of appropriate lengths placed randomly along the ring. We think that this model will prove useful to study the behaviour of composite knots in the presence of more complex physical interactions (e.g. electrostatic, excluded volume) or geometrical confinement [88].

Chapter 4

Entanglement effects in solutions of polymer rings of different topology

4.1 Introduction

From this chapter we begin to study the interplay between topological properties and externally imposed geometrical or physical constraints, such as geometrical confinement or the influence of surrounding rings in a solution of unconcatenated ring polymers.

Characterizing the equilibrium and kinetic properties of semi-dilute solutions of ring polymers is one of the major remaining challenges in theoretical and experimental polymer physics [117, 20, 94, 95, 53, 44, 45, 111]. One aspect of these systems that is very actively investigated regards how intra-chain and inter-chain entanglement reverberate on physical properties of rings solutions. Unlike the case of linear chains, entanglement effects in solutions of ring polymers must take into account topological constraints which are quenched during system preparation, such as the rings topological status (intra-chain entanglement) and relative linking status (inter-chain entanglement). In particular a melt obtained by increasing the density of a solution of unlinked rings will be composed only of unlinked rings. Those topological constraints deeply affect the statics and dynamics of ring polymer solutions which are therefore substantially different from those of solutions of linear polymers.

Static properties of melts of unknotted and unlinked rings have been studied numerically by several groups. Cates and Deutsch [20] and Müller et al. [94] have suggested that strong inter-chain topological interactions lead to pronounced chain compaction of *unlinked* and *unknotted* rings in semi-dilute solutions, and that the typical chain configuration should resemble a branched polymer (akin to a lattice animal) [94]. Further studies both by Müller et al. and Vettorel et al. showed that increasing ring length, rings acquire a more

compact structure [95, 44], compatible with a "crumple-globule" regime [42, 44, 45]. In the latter regime, each ring portion is highly compact and minimally intermingling with the rest of the chain [42], similarly to dense systems of long biopolymers in vivo, such as eukaryotic chromosomes [115].

The influence of topological constraints on the dynamics of molten ring polymers is highlighted by the qualitative and fundamental difference in their kinetics compared to that of linear chains. The kinetics of linear chains in melt is described by the so-called Edwards-DeGennes *reptation* model [28, 25]. According to this model, each chain is confined inside a tube-like region resulting from the excluded-volume interactions with the neighboring chains. The motion of each chain therefore consists of a one-dimensional diffusion along the tube centerline resulting from the "inchworm movements" of small sub-chain loops. This type of local motion is found also in polymer rings moving through a fixed array of obstacles [117]. However, the asymptotic standard diffusive behavior of polymer chains in melt depends on the ongoing process of "tube renewal" which results from the fact that the two polymer ends are practically free and hence capable of exploring and realizing new configurations [28, 25, 10, 34, 141, 63]. This mechanism, which has received striking experimental confirmations as being the dominant kinetic process in dense polymer melts [153], explicitly builds on the linear character of the chains in solution. Hence, it is not applicable, at least in its conventional formulation, to ring polymers. The latter must consequently relax and move in dense solution according to different kinetic mechanisms [20], which are only recently being characterized by means of computationally-intensive molecular dynamics simulations [50, 136, 49, 44, 45, 111, 110].

Here we use stochastic molecular dynamics simulations to investigate complementary aspects of the effects that intra- and inter-chain topological constraints have on kinetic and equilibrium properties of solutions of model ring polymers. Specifically, we consider systems in which the contour length of the rings is fixed while the solution density is varied so to cover an appreciable range of inter-chain entanglement. The study is carried out for monodisperse solutions of unknotted rings as well as trefoil-knotted ones. To have a better insight into topological effects on the statics and dynamics of knotted rings we look also at the knotted portion of the ring using the tools introduced in chapter 2.

To the best of our knowledge this is the first time that a systematic off-lattice study of kinetic and equilibrium properties of rings with non-trivial topology and of their knotted portions has been carried out.

By first exploring the metric and shape properties of equilibrated rings in solution we

find that their behavior depends appreciably on ring topology and that not only it differs from the one seen for linear polymers of equivalent contour length in solutions but even from other physical realizations of dense ring polymers. Specifically, unlike what has been observed in collapsed knotted rings [76, 12] and in confined ones [138], the average size of the knotted portion of a ring in solution is only weakly affected by the increase (for increasing monomer concentration) of the system's geometrical entanglement. In particular, by increasing the solution density, no crossover to delocalized knots is observed, as well as no multiscale behavior of the entanglement, at variance with what we will observe in chapter 5 for spherically confined trefoil knotted rings.

The presence of topological constraints makes the dynamics of rings in solution an even richer phenomenon whose understanding requires a full knowledge of the relationship between the spatial motion of a ring in a melt and the motion of its knotted portion along the ring backbone. By using the knot location tool previously mentioned, and considering dynamic observables commonly used in polymer contexts we show that several time scales are at play: the autocorrelation time of ring configurations, the time required by the rings to diffuse over regions comparable to their average size and – for knotted rings – the time required by the knot to diffuse over the ring contour.

Various relaxation properties of the entire ring are found to change by one order of magnitude across the considered density range. The slowest kinetic process is associated with the diffusion along the backbone of the knotted region. This property, that to the best of our knowledge has not been pointed out before, seamlessly integrates with the other kinetic aspects thus offering a consistent picture for polymer relaxation in solutions of topologically constrained rings.

The author of this thesis contributed to this work by developing the knot location tools and performing part of the analysis. Simulations were performed by a collaborator, A. Rosa.

4.2 Model and methods

4.2.1 The model

To model the rings in solution, we use the bead-spring polymer model introduced by Kremer and Grest [62]. The model accounts for the connectivity, bending rigidity, excluded volume and topology conservation of polymer chains.

Specifically, the intra-chain energy consists of the following terms:

$$\mathcal{H}_{intra} = \sum_{i=1}^{N}[U_{FENE}(i,i+1) + \tag{4.1}$$

$$U_{br}(i,i+1,i+2) + \tag{4.2}$$

$$\sum_{j=i+1}^{N} U_{LJ}(i,j)] \tag{4.3}$$

where n is the total number of beads per ring, and i and j run over the indices of the beads. The latter are assumed to be numbered consecutively along the ring from one chosen reference monomer. The modulo-n indexing is implicitly assumed because of the ring periodicity.

From now on we shall take the nominal bead diameter, σ, as the unit length and adopt the following notation: the position of the center of the ith beads is indicated by $\vec{r}_i$ while the pairwise vector distance of beads i and j is denoted as $\vec{d}_{i,j} = \vec{r}_j - \vec{r}_i$ and its norm simply as $d_{i,j}$.

With this notation the chain connectivity term, $U_{FENE}(i,i+1)$ is expressed as:

$$U_{FENE}(i,i+1) = \begin{cases} -\frac{k}{2} R_0^2 \ln\left[1 - \left(\frac{d_{i,i+1}}{R_0}\right)^2\right], d_{i,i+1} \leq R_0 \\ 0 \qquad\qquad\qquad\qquad\qquad , d_{i,i+1} > R_0 \end{cases} \tag{4.4}$$

where $R_0 = 1.5\sigma$, $k = 30.0\epsilon/\sigma^2$ and the thermal energy $k_B T$ equals 1.0ϵ [62]. The bending energy has instead the standard Kratky-Porod form (discretized worm-like chain):

$$U_{br}(i,i+1,i+2) = \frac{K_B T \xi_p}{\sigma}\left(1 - \frac{\vec{d}_{i,i+1} \cdot \vec{d}_{i+1,i+2}}{d_{i,i+1}\, d_{i+1,i+2}}\right) \tag{4.5}$$

where $\xi_p = 4.5\sigma$ is the nominal persistence length of the chain [118]. Polymer chains are significantly bent by thermal fluctuations at contour lengths larger than b_K, where $b_K = 2\xi_p = 9.0\sigma$ is the Kuhn length of the chain [28, 118].

The excluded volume interaction between distinct beads (including consecutive ones) corresponds to a purely repulsive Lennard-Jones potential:

$$U_{LJ}(i,j) = \begin{cases} 4\epsilon[(\sigma/d_{i,j})^{12} - (\sigma/d_{i,j})^6 + 1/4], d_{i,j} \leq \sigma 2^{1/6} \\ 0, d_{i,j} > \sigma 2^{1/6} \end{cases} . \tag{4.6}$$

This repulsive interaction controls the inter-chain excluded volume too:

$$\mathcal{H}_{inter} = \sum_{I=1}^{N-1} \sum_{J=I+1}^{N} U_{LJ}(i,j) \tag{4.7}$$

where N is the number of rings in solution and the index i $[j]$ runs over the beads in chain I $[J]$.

4.2.2 Simulation details

We consider solutions of $N = 64$ rings, each consisting of $n = 216$ beads (i.e., the ring contour length, $L_c = 216\sigma$ corresponds to $24 b_K$) at six different monomer densities, ρ: $\rho\sigma^3 = 0.010, 0.025, 0.050 < \rho^*\sigma^3$, $\rho\sigma^3 = 0.100$ and $\rho\sigma^3 = 0.200, 0.400 > \rho^*\sigma^3$.

The chosen densities span from a dilute situation to one where the inter-chain entanglement is significant and yet the solution is isotropic [142]. The lowest monomer density is much smaller than the one at which one expects significant ring overlap. The overlap density is estimated as [28],

$$\rho^* \approx \frac{L_c/\sigma}{\langle R_g^2 \rangle^{3/2}} \ . \tag{4.8}$$

where $\langle R_g^2 \rangle$ is the mean square radius of gyration of an isolated ring. Using the Zimm-Stockmayer estimate for the isolated ring size [154], $\langle R_g^2 \rangle = \frac{L_c\, b_K}{12} \approx 162\sigma$ yields $\rho^*\sigma^3 \approx 0.1$, which is an order of magnitude larger than the minimal monomer density considered here.

Above this density, significant mutual entanglement of the chains is expected. For dense solutions of *linear* polymers, the intricacy of the melt [25, 28] and the resulting physical properties [34, 142] are captured by the entanglement length, L_e. Roughly speaking, this quantity corresponds to the typical chain arclength separation between two consecutive topological constraints (known as *entanglements*) arising from inter-chain *un*crossability. It has been recently proposed [142] that the relationship tying L_e, b_K and the solution density, ρ is adequately captured by the following phenomenological expression:

$$\frac{L_e}{b_K} \approx (0.06\,(\rho\,\sigma\,{b_K}^2))^{-2/5} + (0.06\,(\rho\,\sigma\,{b_K}^2))^{-2}. \tag{4.9}$$

Using the previous expression, one has that the interval of ρ considered here corresponds to a wide range of L_e for the equivalent system of linear chains. Indeed, for $\rho\sigma^3$ going

from 10^{-2} to 0.4 we have that L_e/b_K spans from ≈ 400 to ≈ 1. In the latter situation, the entanglement length is approximately equal to the Kuhn length, and hence the system is at the crossover from the loosely- to the tightly-entangled regimes (i.e. the chain is nearly straight between two consecutive entanglements [93]). Higher densities are not considered, because for $\rho\sigma^3 \gtrsim 0.5$ the onset of the Onsager isotropic/nematic transition [142] is expected to break the spatial isotropy of the solution.

For reference, we also consider isolated rings, and solutions of $N = 21$ rings in very dilute conditions ($\rho\sigma^3 = 0.003$).

The equilibrium and kinetic properties of these systems are studied using fixed-volume and constant-temperature Molecular Dynamics (MD) simulations. MD simulations have been performed by A. Rosa using the LAMMPS engine [105] with Langevin thermostat (target temperature = 1.0 LJ-units). The elementary integration time step is chosen equal to $\Delta t = 0.012\tau_{MD}$, where $\tau_{MD} = \sigma(m/\epsilon)^{1/2}$ is the Lennard-Jones time, m is the bead mass and the friction coefficient, γ, corresponds to $\gamma/m = 0.5\tau_{MD}^{-1}$ [62]. We stress that, because we are dealing with model polymers, the solvent is not explicitly included in our simulation. The polymer-solvent interaction is effectively accounted for only through the Langevin thermostat and related friction term.

Preparation of initial configurations

At each density, we consider monodisperse solutions, consisting either of unknotted (Un) *or* trefoil-knotted (3_1) rings.

The system initialization consists of placing a template unknotted or trefoil-knotted ring at the center of a cubic cell with periodic boundary conditions. The template configuration is replicated 4 times along each spatial direction. The linear dimension of the cubic cell is large enough to avoid overlap and linking between the template copies and yields an initial monomer density of about $\rho\sigma^3 \approx 5 \cdot 10^{-3}$. Prior to the production runs, the cell is first evolved at constant pressure until the desired target density is reached and is subsequently equilibrated for a time span of about $10^5\tau_{MD}$. At all considered densities, this time span exceeds the time required by one ring to diffuse over distances larger than its typical size. Production runs have a typical duration of $6 \cdot 10^6\tau_{MD}$. Typical equilibrated configurations at two different densities are shown in Fig. 4.1.

*

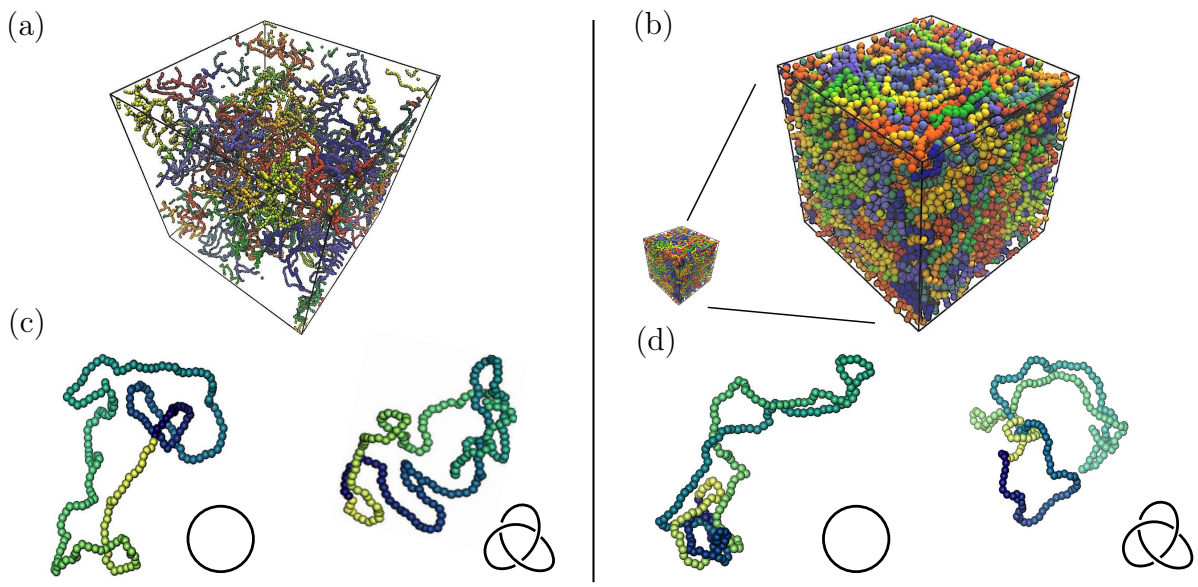

Figure 4.1: Typical configurations of ring polymer solutions, at $\rho\sigma^3 = 0.025$ (a) and $\rho\sigma^3 = 0.4$ (b), and corresponding selected rings with trefoil-knotted (c and d, right) and unknotted topologies (c and d, left). This and some other images in the present chapter have been adapted from reference [116]

.

4.2.3 Ring geometrical properties

Shape and size

Ring shape and size are characterized through the gyration tensor, $\mathbf{Q}$. The entries of this 3×3 matrix are given by:

$$Q_{\alpha,\beta} = \frac{1}{n}\sum_{i=1}^{n}(\vec{r}_{i,\alpha} - \vec{r}_{CM,\alpha})(\vec{r}_{i,\beta} - \vec{r}_{CM,\beta}), \tag{4.10}$$

where α and β run over the three Cartesian components and $\vec{r}_{CM} = \frac{1}{n}\sum_{i=1}^{n}\vec{r}_i$ is the spatial location of the ring center of mass. The non-negative eigenvalues of $\mathbf{Q}$, ranked with decreasing magnitude, Λ_1, Λ_2 and Λ_3 correspond to the square length of the principal axes of the ring gyration ellipsoid. Accordingly, their relative magnitude conveniently captures the overall spatial anisotropy of the rings, while their sum yields the ring square radius of gyration:

$$R_g^2 = Tr\mathbf{Q} = \sum_{\alpha=1}^{3}\Lambda_\alpha, \tag{4.11}$$

where Tr is the *trace* operator. To measure the typical size and anisotropy of the ensemble of rings in solution, we compute the averages $\langle R_g^2 \rangle$ and $\langle \Lambda_{i=1,2,3} \rangle$ where the brackets $\langle ... \rangle$ denote averaging over all rings of all system snapshots at a given solution density.

Identifying the knotted portion of the rings

Because of the chain connectivity constraint, the global topological state of the rings is preserved in the course of the MD evolution. As we saw in chapter 2 the interplay of geometrical and topological entanglement can be aptly described by the linear dimension of the knotted portion. Furthermore the top-down and bottom-up knot location scheme give in general different knot lengths, which we call l_k and l_{sk} respectively. As we saw in § 2.3.4 in the case of FJRs of increasing length the magnitude of the difference $l_k - l_{sk}$ seems to be related with the geometric entanglement of the chains.

Surface accessible area

The rings surface accessible area was computed using the SAS routine of the GROMACS package [32, 46] using a probe sphere of diameter equal to the bead diameter, σ. The computed surface area includes contributions from inner cavities of the ring conformations that are large enough to accommodate the probe sphere.

4.3 Results and discussion

4.3.1 Geometric properties of the rings

We first report on how various equilibrium metric properties of the rings depend on their topology and solution density. In a progression from global to finer aspects, we shall consider the rings size, shape, exposed surface area, the mean-square distance of points at increasing arclength separation and the degree of localization of the knotted portion in 3_1 knotted rings.

For reference, we provide in Table 4.1 the average values of the square radius of gyration, $\langle R_g^2 \rangle$, and the eigenvalues of the gyration tensor for isolated unknotted and trefoil-knotted rings. Analogous quantities are reported for an equivalent freely-jointed ring (FJR) and Gaussian ring (GR) of $L_c/b_K = 24$ bonds [28]. The FJR data are obtained by a Markovian exploration of FJRs, while the GR data are obtained by stochastic

Table 4.1: Average value of the mean square radius of gyration and eigenvalues of the gyration tensor for unkontted and trefoil-knotted isolated rings.[(a)]

	$\langle R_g^2 \rangle$	$\langle \Lambda_1 \rangle$	$\langle \Lambda_2 \rangle$	$\langle \Lambda_3 \rangle$
UN	175.4 ± 0.6	116.3 ± 0.6	43.9 ± 0.1	15.2 ± 0.1
3_1	120.8 ± 0.7	77.9 ± 0.7	30.6 ± 0.1	12.3 ± 0.1
FJR	168.7 ± 0.4	108.5 ± 0.4	42.1 ± 0.2	18.1 ± 0.1
GR	161.6 ± 0.7	106.1 ± 0.6	39.7 ± 0.1	16.2 ± 0.1

[(a)] Analogous quantities are also shown for an equivalent freely-jointed ring (FJR) and Gaussian ring (GR) of 24 bonds. The FJR bond length and the GR root-mean square bond length are equal to $b_K = 9\sigma$. All values are in units of σ^2.

molecular dynamics simulations. Table 4.1 conveys the effect that intra-chain constraints (excluded volume and fixed topology) have on the overall size and shape of rings at infinite dilution. Both types of constraints are absent in the FJR and the GR. Notice, that the FJR and GR quantities are typically within 10% of those of unknotted rings. The difference with analogous quantities for trefoil-knotted rings is substantially larger. These results reflect the fact that, for the considered values of L_c and b_K, unknotted rings dominate the equilibrium ensemble of infinitely-thin (FJR) or Gaussian rings with unrestricted topology. Trefoil-knotted rings therefore possess a degree of entanglement that would be atypical in rings circularized in equilibrium. The presence of the non-trivial topological constraint causes such rings to be tighter and slightly more isotropic than unknotted ones. This result is consistent with the intuitive notion that a certain arclength of trefoil-knotted rings is "used up" [90] in the non-trivial entanglement (in fact the minimal ropelength required to tie trefoil-knotted rings is larger than for unknotted ones).

Ring size and shape

Table 4.2 reports the same metric properties of Table 4.1, but calculated for rings in solution. The data suggest that, for both topologies, the ring size decreases with the monomer density, ρ. Specifically, going from $\rho\sigma^3 = 10^{-2}$ to $\rho\sigma^3 = 0.4$ it is seen that R_g^2 decreases from the typical value of isolated rings down to about half of it. The decreasing trend of the average extension results from the non-concatenation constraint of the rings,

Table 4.2: Mean square radius of gyration, $\langle R_g^2 \rangle$ and average shape parameters of the simulated rings.[(a)]

monomer density	$\langle R_g^2 \rangle$		$\langle \Lambda_1 \rangle / \langle \Lambda_3 \rangle$		$\langle \Lambda_2 \rangle / \langle \Lambda_3 \rangle$	
$\rho\sigma^3$	UN	3_1	UN	3_1	UN	3_1
0.010	165.59±0.37	116.07±0.01	7.45 ±0.05	6.118±0.001	2.77 ±0.01	2.4151±0.0004
0.025	150.55±0.39	108.23±0.08	7.21 ±0.03	5.91 ±0.01	2.63 ±0.02	2.335 ±0.003
0.050	134.64±0.06	97.26±0.05	7.07 ±0.02	5.80 ±0.01	2.530±0.003	2.266 ±0.006
0.100	115.63±0.09	85.62±0.19	7.00 ±0.03	5.95 ±0.02	2.44 ±0.07	2.244 ±0.004
0.200	98.64±0.10	77.94±0.22	7.02 ±0.02	6.29 ±0.03	2.385±0.006	2.260 ±0.008
0.400	86.32±0.85	70.11±0.06	7.46 ±0.13	6.84 ±0.03	2.41 ±0.01	2.318 ±0.008

[(a)] Shape parameters expressed as the ratios $\langle \Lambda_1 \rangle / \langle \Lambda_3 \rangle$ and $\langle \Lambda_2 \rangle / \langle \Lambda_3 \rangle$, where $\langle \Lambda_{\alpha=1,2,3} \rangle$ are the three average eigenvalues of the gyration tensor, Eq. 4.10. $\langle R_g^2 \rangle$ values are in units of σ^2. For very dilute conditions ($\rho\sigma^3 = 0.010$), the calculated quantities are close to the theoretical values for ideal semi-flexible rings (see Table 4.1).

consistent with previous numerical findings [94, 95]. It should also be noted that the monomer density attained by each ring is much smaller than the density of the entire solution. In fact, even in the densest case $\rho\sigma^3 = 0.4$ the individual ring density – defined as the number of ring monomers divided by the volume of the average gyration ellipsoid – is only $\approx 0.05\sigma^{-3}$ for unknots and $\approx 0.06\sigma^{-3}$ for trefoil-knotted rings. These findings suggest that an increase of solution density promotes extensive chain intermingling as opposed to tight compaction of the individual rings.

A further indication that an increase of the solution density affects only weakly the metric properties of each ring is given by looking at the typical ring shape. For this purpose, following previous studies of either closed or open chains [16, 119, 3], we calculate the average eigenvalues $\langle \Lambda_{\alpha=1,2,3} \rangle$ of the gyration tensor, Eq. 4.10 which are shown in Table 4.2. We note that the ratios $\langle \Lambda_1 \rangle / \langle \Lambda_3 \rangle$ and $\langle \Lambda_2 \rangle / \langle \Lambda_3 \rangle$ fluctuate by a few percent throughout the explored range of solution densities and remain close to the overall anisotropy expected for equivalent, isolated FJRs (see Table 4.1).

Exposed surface.

To complete the statistical characterization of ring conformations we next focus on the average exposed surface area of each ring. This is an important geometric indicator that

aptly complements the radius of gyration [94, 95, 44, 45, 42] in describing the overall degree of ring compactness attained in solutions of increasing density. We stress that, because the purpose is to characterize the properties of individual rings, the exposed surface per bead is calculated separately for each ring, i.e. without taking into account the burial effect due to the surrounding chains. Furthermore, the exposed surface is calculated by taking into account voids (cavities) possibly present in a ring (see Methods, Sec. 4.2.3).

The varying degree of exposure of the beads in a ring is illustrated in Fig. 4.2b: the profile pertains to the unknotted ring conformation in panel (a) (picked at $\rho\sigma^3 = 0.4$), where the beads are color coded according to the degree of exposure. For reference, in panel (b) it is also shown the value of the exposed surface per bead in a perfectly straight chain configuration. For the case shown in panels (a-b), highly exposed beads nearly approach this reference value, while the most buried ones have an exposed surface equal to about 1/3 of the reference value. The distributions of the total exposed surface per ring are shown in panel (c): in particular, we notice that the ring exposed surface covers a moderately narrow interval. Nevertheless, the exposed area for trefoil-knotted rings is generally smaller than for the unknots (at the same monomer concentration, ρ), and the mean value of the exposed surface per bead (averaged over all beads of all rings in various configurations at fixed density) is a decreasing function of solution density.

Finally, it is interesting to correlate the decrease of the surface area with the decrease of the ring radius of gyration observed for increasing density. This relationship is shown in panel (d) of Fig. 4.2. By taking into account the different scales and offsets of the two axes in the graph it is realized that unknotted and trefoil rings at the same monomer concentration differ appreciably by average size (see also Table 4.2) though not by exposed surface. Secondly, the density-dependent decrease of the radius of gyration is not paralleled by an analogous decrease of the exposed surface. In fact, with respect to the diluted case, the latter diminishes by less than 5% up to $\rho\sigma^3 = 0.2$ and by less than 10% up to $\rho\sigma^3 = 0.4$. We note that simple dimensional considerations would have suggested, instead, a proportional dependence of the surface accessible area on $\langle R_g^2 \rangle$. The failure of the simple dimensional analysis suggests that, despite ring sizes that are, on average, smaller at higher densities, the corresponding configurations are still sufficiently exposed to the solvent and maintain around each bead enough "free room" to accommodate the probe sphere used to measure the accessible surface.

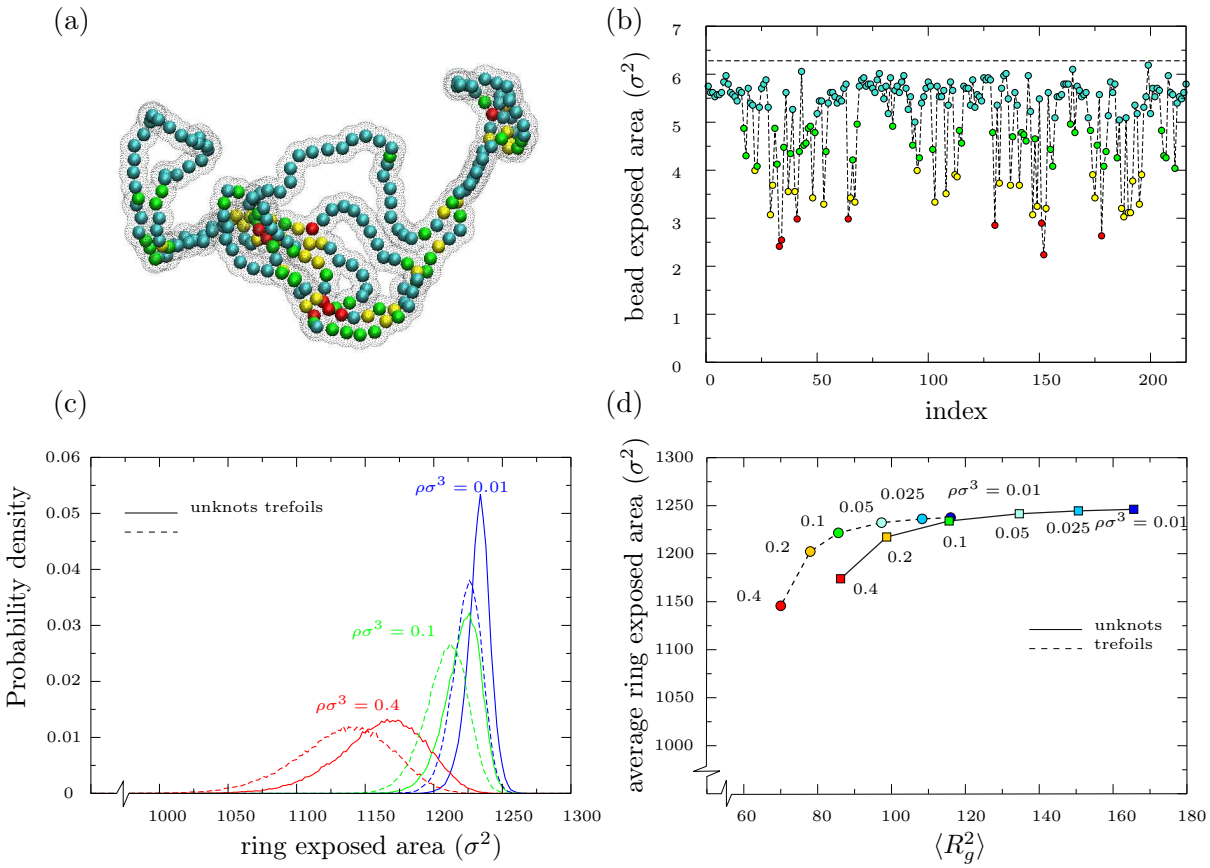

Figure 4.2: (a) The shaded region outlines the accessible surface of the shown ring configuration. This is calculated using the SAS routine of the GROMACS package [46, 32] with a probe sphere of diameter equal to the bead diameter, σ. Monomer beads are colored from red to cyan for increasing degree of their surface exposure, shown in panel (b) with the same coloring scheme. (c) Probability distribution functions of the total accessible surface per ring, for different solution densities and chain topologies. (d) Average accessible surface per ring as a function of the ring average size, for different solution densities and chain topologies.

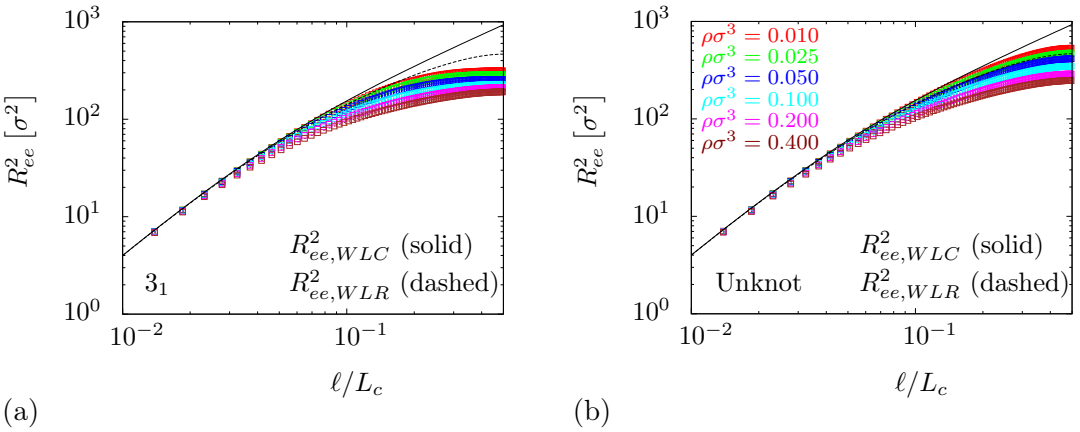

Figure 4.3: Average square spatial distance R^2_{ee} between ring monomers as a function of their (normalized) contour length separation, ℓ/L_c, along the chain: results for (a) unknotted and (b) trefoil-knotted ring polymers at increasing monomer densities.

Geometry of ring portions.

The results presented so far address properties of entire rings. We shall next examine how various ring portions, or arcs, are affected by intra-chain and inter-chain entanglement. We first report on how the mean square end-to-end distance, $R^2_{ee}(\ell)$ of arcs of contour length ℓ, depends on the solution density and ring topology. Furthermore, for rings with non-trivial topology we shall identify the smallest arc accommodating the knot and examine how its contour length depends on the monomer density.

The density-dependent behavior of $R^2_{ee}(\ell)$ is shown in Fig. 4.3. The data for knotted and unknotted rings are presented in two separate panels. For reference, in each panel we include the graph for the mean square end-to-end distance for a worm-like chain (WLC):

$$R^2_{ee,WLC}(\ell) = \frac{{b_K}^2}{2}\left[\frac{2\ell}{b_K} + \exp\left(-\frac{2\ell}{b_K}\right) - 1\right]. \tag{4.12}$$

The analogous expression for a worm-like ring (WLR) is closely approximated by:

$$R^2_{ee,WLR}(\ell) = \left(\frac{1}{R^2_{ee,WLC}(\ell)} + \frac{1}{R^2_{ee,WLC}(L_c - \ell)}\right)^{-1}. \tag{4.13}$$

The latter expression is obtained by matching analytically the exact, small-ℓ (stiff) and large-ℓ (flexible) limiting behaviors for a ring polymer.

Fig. 4.3 shows that for both unknotted and trefoil-knotted rings at all densities, the WLC (and WLR) behavior is followed closely only for arclengths smaller than about b_K (corresponding to $\ell/L_c \sim 0.04$). Beyond this arclength, the WLR behavior is followed well by unknotted rings in dilute solutions. Noticeable differences from the WLR trend occur for both unknotted and knotted rings at densities larger than $\rho^*\sigma^3 = 0.1$. The deviations grow with: (i) increasing solution density at fixed topology and arclength separation; (ii) increasing arclength separation at fixed topology and density; (iii) changing ring topology from unknotted to trefoil-knotted at fixed density and arclength separation. In summary, departures from the WLR trend are seen upon increasing either the inter-chain (solution density) or the intra-chain (topological) entanglements.

Properties of the knotted portion of 3_1 rings.

We conclude the analysis of the equilibrium properties by examining how density influences the top-down (l_k) and bottom-up (l_{sk}) lengths of the ring portion accomodating the knot.

The analysis is motivated by recent studies which showed that the typical value of l_{knot} is substantially larger for collapsed rings than for unconstrained or swollen ones [76, 12]. In addition it is possible that a change in the ring properties will result in a multiscale behaviour, characterised by the two knot localization schemes giving very different value for the length of the knotted portion.

In the present context, we observe that the average values of l_k and l_{sk} remain fairly constant and close to each other, although above the overlap density ρ^* their difference increases with increasing solution density, see Fig. 4.4. Looking at the knot length distributions above the overlap density, ρ^*, (see Fig. 4.5) we note that while tighter knots become more probable according to both knot location schemes, the probability distribution function of the top-down knot length acquires a larger tail for high values of l_k/L_c.

Given the compatibility of the two measures in the following we will always use the bottom-up approach to locate the knotted portion.

4.3.2 Dynamical properties

The growing level of entanglement found in solutions of increasing density is expected to strongly impact the ring dynamics. By analogy with the case of linear polymers melts [28, 62, 34, 140, 63], multiple dynamical regimes are expected. For the latter system, it

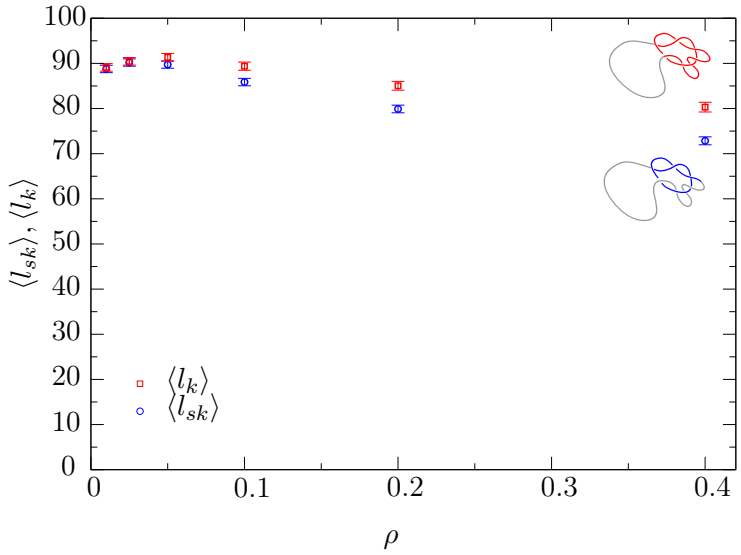

Figure 4.4: Average knot lengths l_{sk} and l_k according to the bottom-up and top-down knot location schemes.

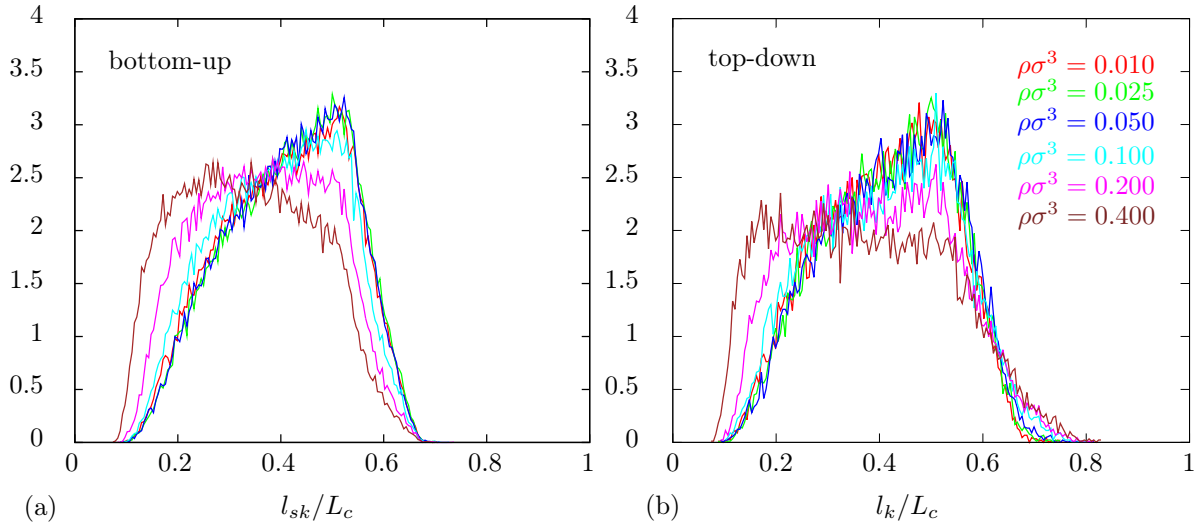

Figure 4.5: Probability distribution function of the normalized knot lengths l_{sk}/L_c and l_k/L_c computed with the bottom-up (a) and the top-down (b) knot location schemes, at different monomer concentrations.

is known that at times longer than the slowest chain relaxation time, the motion of the chain center of mass follows the standard diffusion while at smaller times the kinetics is dominated by the slow chain reptation inside the tube created by inter-chain constraints [62].

We accordingly monitor several observables:

1. The typical time scale for ring diffusion in space;

2. The time scales dominating the fluctuations in rings size and orientation;

3. Finally, for rings with non-trivial topology, we examine how the knotted portion moves both in space and along the ring backbone.

Some of the above mentioned quantities have been considered before in studies on melts of unknotted rings [143, 94, 95, 45], in lattice models of isolated knotted rings [109, 64, 98], and in polymer models of knot diffusion along DNA [13, 146]. The present context therefore offers an opportunity to examine the impact of both solution density and ring topology on dynamics and compare the time-scales associated to the various phenomena.

Time autocorrelation function for the radius of gyration.

We start by considering the time autocorrelation function of an internal (i.e. independent of the ring absolute space position and orientation) quantity, namely the radius of gyration:

$$C_{R_g}(t) = \frac{\langle R_g(t)\, R_g(0)\rangle - \langle R_g\rangle^2}{\langle R_g^2\rangle - \langle R_g\rangle^2}. \tag{4.14}$$

where the brackets, $\langle ...\rangle$, denote the average over simulation time and over rings. The behavior of $C_{R_g}(t)$ was considered in recent lattice studies of *isolated*, unconstrained knotted and unknotted rings [64, 98]. These investigations showed that C_{R_g} decays with a characteristic time, τ_{R_g}, that is larger for knotted rings than for unknotted ones [64, 98]. The effect reflects the enhanced self-hindrance of rings with non-trivial topology; consider, for instance, that the minimal number of crossings observed in any two-dimensional projection of an unknotted ring is zero, while it is three for trefoil-knotted rings (which hence must necessarily wind on themselves more than unknots).

Investigating the decay properties of $C_{Rg}(t)$ in the present context serves a twofold purpose. On the one hand, it can clarify whether the above-mentioned lattice results

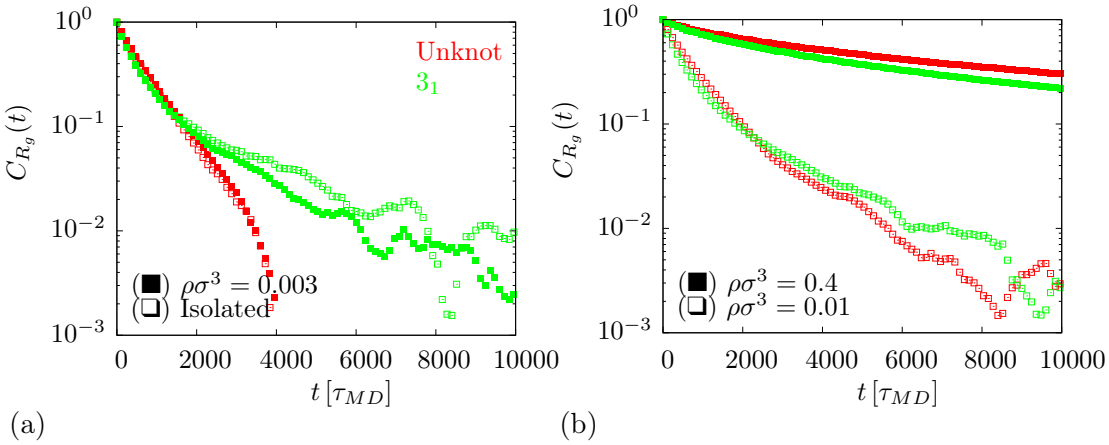

Figure 4.6: Radius of gyration time correlation function $C_{R_g}(t)$ (Eq. 4.14) for unknots (red symbols) and trefoils (green symbols). (a): Result for isolated rings (open symbols) and rings in very dilute conditions with $\rho\sigma^3 = 0.003$ (filled symbols). The long time behavior of $C_{R_g}(t)$ for 3_1 rings deviates from the $C_{R_g}(t)$ for the unknots, and shows a longer exponential tail, in agreement with previous studies of isolated ring polymers on lattice [109, 64, 98]. (b): Results for $\rho\sigma^3 = 0.01$ (open symbols) and $\rho\sigma^3 = 0.4$ (filled symbols).

apply to off-lattice contexts, too. On the other hand, by analyzing the dependence of $C_{R_g}(t)$ on solution density, it is possible to assess if, and to what extent, the increased intra-chain and inter-chain entanglement affect differently the size relaxation times of unknotted and knotted rings.

According to this plan we first compute C_{R_g} from simulations of *isolated* knotted and unknotted rings. The results are shown in Fig. 4.6a (open symbols) and fully support the lattice results regarding the slower relaxation of trefoils compared to unknots. For rings in solutions, at all considered densities ($\rho\sigma^3 = 0.01 - 0.4$), one is surprised to find that the C_{R_g} curves for trefoils and unknots display much smaller differences compared to the isolated case, see Fig. 4.6b. Indeed, a behavior quantitatively similar to the isolated case is found only at densities lower than $\rho\sigma^3 = 0.003$, as shown in Fig. 4.6a. The effect is quantitatively captured by calculating the effective relaxation time, τ_{R_g}, given by the integral of $C_{R_g}(t)$, see Table 4.3. The data in the table illustrate vividly that the density-dependent increase of the intra- and inter-chain entanglement obliterates differences in the average kinetic behavior of rings with different topological state. For both unknots and trefoils, τ_{R_g} has an order of magnitude increase over the considered range of solution density, ρ. Notice that upon increasing ρ, the value of τ_{R_g} for unknots overtakes the one of trefoils (see also the order of the red and green curves in panels a

Table 4.3: Correlation times τ_{R_g} and τ_{diam} [(a)]

monomer density	τ_{R_g} $[10^2\tau_{MD}]$		τ_{diam} $[10^2\tau_{MD}]$		τ_{CM} $[10^2\tau_{MD}]$	
$\rho\sigma^3$	UN	3_1	UN	3_1	UN	3_1
Single ring	6.6 ± 0.6	7.9 ± 0.6	28 ± 1	16 ± 1	31	22
0.003	7.0 ± 0.6	7.0 ± 0.6	27 ± 1	16 ± 1	34	24
0.010	8.1 ± 0.6	7.3 ± 0.6	27 ± 4	16 ± 3	48	36
0.025	11 ± 1	7.8 ± 0.6	28 ± 4	16 ± 3	48	36
0.050	16 ± 1	10 ± 1	31 ± 4	17 ± 3	60	36
0.100	27 ± 1	15 ± 1	39 ± 4	22 ± 3	72	48
0.200	47 ± 1	26 ± 1	61 ± 4	33 ± 3	120	72
0.400	125 ± 1	73 ± 1	159 ± 4	92 ± 4	390	220

[(a)] Correlation times were calculated by numerical integration of the respective time correlation functions $C_{R_g}(t)$ (Eq. 4.14) and $C_{diam}(t)$ (Eq. 4.15). Numerical integration is limited to the time interval where correlation functions are $> 10^{-2}$. τ_{CM} is defined as the typical time required by rings to transverse a region of linear size comparable to the ring average gyration radius, i.e. $\delta r^2_{CM}(\tau_{CM}) = \langle R_g^2 \rangle$ (see Eq. 4.16). All times are expressed in units of $10^2\tau_{MD}$.

and b in Fig. 4.6).

Reorientation time.

We now turn to consider kinetic properties that do depend on the absolute orientation of rings in space. For linear polymers, it is customary to consider the autocorrelation function of the end-to-end vector [28] which, for closed chains, admits several generalizations [45]. The one considered here is the time correlation of the ring diameter vector:

$$C_{diam}(t) = \frac{\langle \vec{d}(t) \cdot \vec{d}(0) \rangle}{\langle |\vec{d}|^2 \rangle}, \tag{4.15}$$

where $\vec{d}$ is the vector joining two monomers that are "diametrically opposite" on the ring backbone, i.e. monomers with the largest possible chemical distance, $L_c/2$. Here the brackets $\langle \cdots \rangle$ denote a multiple average: over the dynamical trajectory and over each pair of diametrically opposite beads for every ring in solution. Notice that C_{diam} is sensitive to both changes in modulus of the diameter vector and to its absolute orientation. For this reason, τ_{diam}, the characteristic decay time of $C_{diam}(t)$ is customarily referred to as

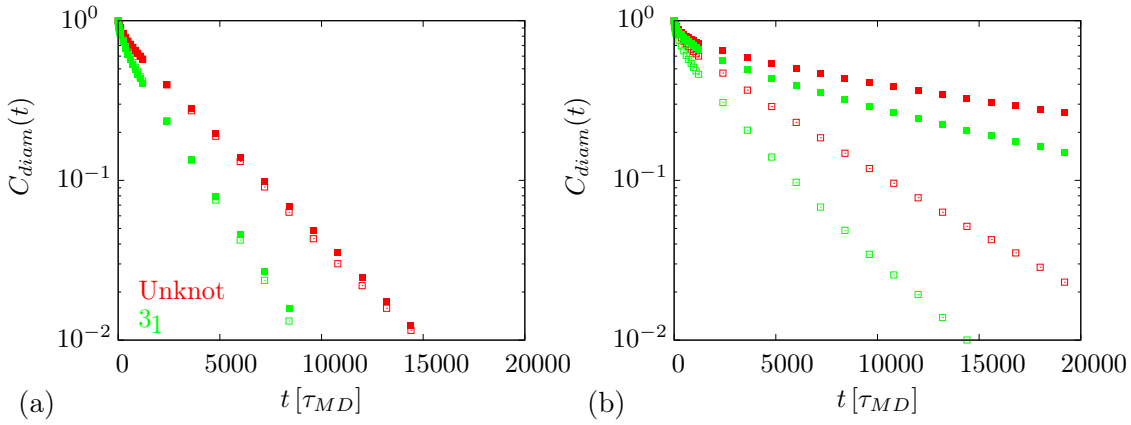

Figure 4.7: Ring diameter time correlation function $C_{diam}(t)$ (Eq. 4.15) for the unknots (red symbols) and trefoils (green symbols). (a): $\rho\sigma^3 = 0.01$ (open symbols) and $\rho\sigma^3 = 0.025$ (filled symbols). (b): $\rho\sigma^3 = 0.1$ (open symbols) and $\rho\sigma^3 = 0.4$ (filled symbols).

the *reorientation* time.

Fig. 4.7 portrays $C_{diam}(t)$ for unknots (red symbols) and 3_1 knots (green symbols) at different monomer concentrations. Analogously to τ_{R_g}, we define the corresponding τ_{diam} as the numerical integral of $C_{diam}(t)$. Final results are reported in Table 4.3. As for $C_{R_g}(t)$, the asymptotic decay time of $C_{diam}(t)$ depends on ring topology and is faster for trefoils than unknots. To the best of our knowledge this effect, that holds at all densities, was neither pointed out nor addressed before. Extending this analysis and considerations to rings with more complicated knot types could represent an interesting avenue for further investigations.

Diffusion of the ring center of mass.

Because trefoils are more compact than unknots they should diffuse faster in the solution, analogously to what they do in other types of media [41, 151]. This intuitive expectation is indeed confirmed by inspecting Fig. 4.8, which portrays the mean square displacement of the ring center of mass, $\delta r^2_{CM}(t)$, for time lags of increasing duration, t:

$$\delta r^2_{CM}(t) \equiv \langle (\vec{r}_{CM}(t) - \vec{r}_{CM}(0))^2 \rangle. \tag{4.16}$$

The displacement data given in Fig. 4.8 pertain to $\rho\sigma^3 = 0.2$; similar plots are obtained for different values of ρ. It is seen that over the time-span covered by the simulations, both unknotted and trefoil rings diffuse over distances that exceed by several orders of

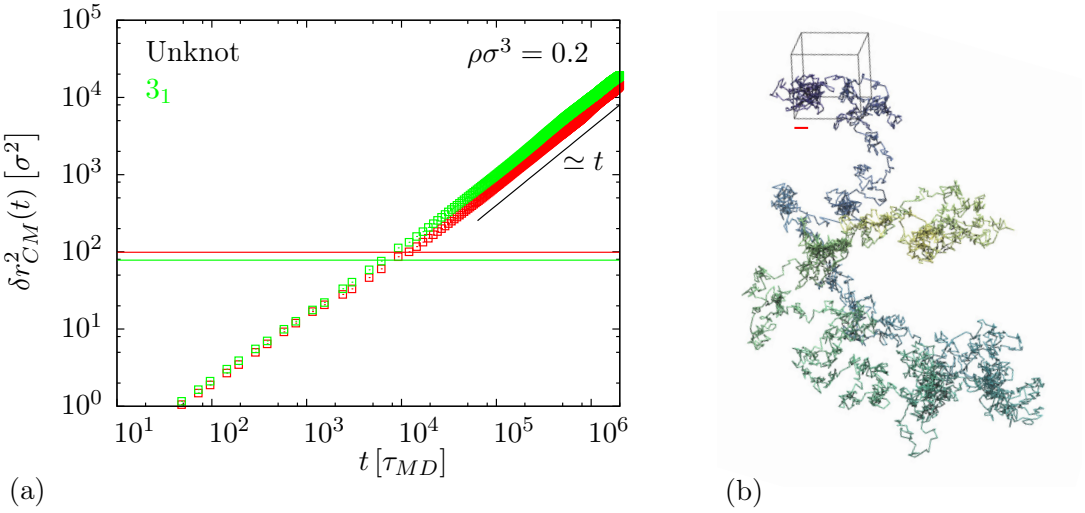

Figure 4.8: (a): Comparison between the time mean-square displacement of the rings center of mass ($\delta r^2_{rCM}(t)$, Eq. 4.16) for unknots (red symbols) and trefoils (green symbols) and the corresponding average square gyration radii (horizontal lines), for $\rho\sigma^3 = 0.2$. Within the considered time-span, rings diffuse over distances much larger than their typical sizes. (b): Diffusive motion of the center of mass of a randomly selected trefoil, for $\rho\sigma^3 = 0.2$. The red bar denotes the average ring size, $\langle R_g^2\rangle^{1/2}$. Corresponding plots at different monomer densities look qualitatively similar.

magnitude their average size. For traveled distances larger than the average ring size, the motion of the center of mass follows standard diffusion. The corresponding diffusion time τ_{CM}, defined as $\delta r^2_{CM}(\tau_{CM}) = \langle R_g^2\rangle$, is given in Table 4.3. Notice, that the values of τ_{CM} are comparable to the values of τ_{diam} at the same solution density, consistently with the case of linear polymers [28].

Motion of the knot along the chain contour

Finally, we examine the dynamics in space and along the ring backbone of the knotted portion of the trefoils. This is a computationally-demanding task, because the numerically-costly identification of the knotted portion must be carried out for each ring of all sampled system snapshots.

For simplicity, the instantaneous position of the knot on the ring is taken to coincide with the chemical coordinate of the midpoint of the knotted portion (defined with respect to the absolute monomer indexing of the ring set at the beginning of the simulation). The instantaneous knot midpoint position, $s_k(t)$ is recorded at fixed time intervals, $\Delta t = 120\tau_{MD}$. The incremental knot displacement between time snapshots $n\left(=\frac{t}{\Delta t}\right)$ and

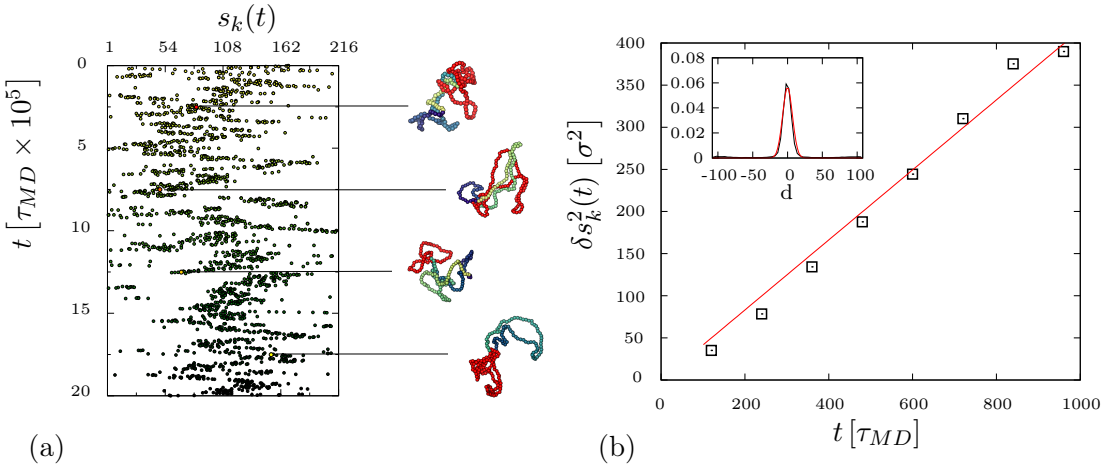

Figure 4.9: (a) Time behavior of the knot midpoint position along the ring contour. Midpoint coordinates are defined with respect to a reference monomer chosen at the beginning of the simulation. On the right, four ring configurations sampled at different times along the trajectory, with the corresponding knotted portions marked in red. (b) Mean square displacement of the knot along the ring contour, $\delta s_k^2(t)$ (Eq. 4.18), at density $\rho\sigma^3 = 0.1$. The proportional dependence on time (red line passing through the origin) can be expressed as $2D_k t$, where D_k is the one-dimensional diffusion coefficient: for the case shown, $D_k = 0.21\sigma^2/\tau_{MD}$ (see Table 4.4, for a list of diffusion coefficients at all monomer concentrations). *Inset*: The Gaussian distribution (red curve) associated with the model one-dimensional diffusion process matches well the numerical distribution (black line) of incremental knot displacements, d_k (Eq. 4.17).

$n+1$, $d_k(n)$, is computed using the expression:

$$d_k(n) = \left\{ \left[s_k(t+\Delta t) - s_k(t) + \frac{3}{2}L_c \right] \bmod L_c \right\} - \frac{L_c}{2} \tag{4.17}$$

where "mod" denotes the modulus operation. The previous expression ensures that the displacement is mapped in the $[-L_c/2, L_c/2]$ interval. The value of Δt is sufficiently small that, at all considered densities, the occurrence of large "jumps" (say equal or larger than $L_c/4$ in modulus) is rare. This is illustrated in the inset of Fig. 4.9 (for $\rho\sigma^3 = 0.1$) which further highlights the Gaussian character of the distribution.

The knot mean square displacement on the ring contour, $\delta s_k^2(t)$, is defined by

$$\delta s_k^2(t = i\cdot\Delta t) = \left\langle \left(\sum_{j=0}^{i-1} d_k(j) \right)^2 \right\rangle, \tag{4.18}$$

Table 4.4: Diffusion coefficients, D_k for the motion of the knotted portion along the ring contour length[(a)]

Monomer density $\rho\sigma^3$	D_k $[\sigma^2/\tau_{MD}]$	τ_k $[\tau_{MD}]$
0.010	0.18 ± 0.01	2.1×10^4
0.025	0.19 ± 0.01	2.0×10^4
0.050	0.19 ± 0.01	2.0×10^4
0.100	0.21 ± 0.01	1.8×10^4
0.200	0.23 ± 0.01	1.6×10^4
0.400	0.16 ± 0.02	2.3×10^4

[a] The value of D_k corresponds to half the slope of the line that, passing through the origin, provides the best interpolation to $\delta s_k^2(t)$ vs t. The typical diffusion (sliding) time, τ_k, is defined as the time required to diffuse by a backbone distance equal to the typical knot contour length ($\approx 40\%$ of the ring contour length, see Fig. 4.4).

where the summation index runs over consecutive displacements, and the average $\langle ... \rangle$ is taken (1) over the trajectory and (2) over the rings ensemble. Fig. 4.9 illustrates that a linear relationship holds between $\delta s_k^2(t)$ and time, indicating that the knot sliding on the ring backbone can be treated as a one-dimensional diffusion process. The corresponding diffusion coefficients, D_k, calculated at different solution densities are given in Table 4.4 which also reports the typical time, τ_k, required by the knot to diffuse by its average length on the ring backbone. Interestingly, τ_k is almost unaffected by increasing monomer concentration. In addition, for a given solution density, τ_k exceeds all other characteristic times given in Table 4.3.

Motion of the knotted portion in space.

The above observation indicates that the knot location on the ring backbone is practically quenched as a ring diffuses in space over a distance equal to its size. This suggests that the three-dimensional motion of the knotted portion should be akin to the one of a fixed, tagged, portion of the ring of comparable size.

This observation was verified by considering the time dependence of the mean-square displacement of the knot center of mass, defined (analogously to Eq. 4.16) as:

$$\delta r_{kCM}^2(t) = \langle (\vec{r}_{kCM}(t) - \vec{r}_{kCM}(0))^2 \rangle. \tag{4.19}$$

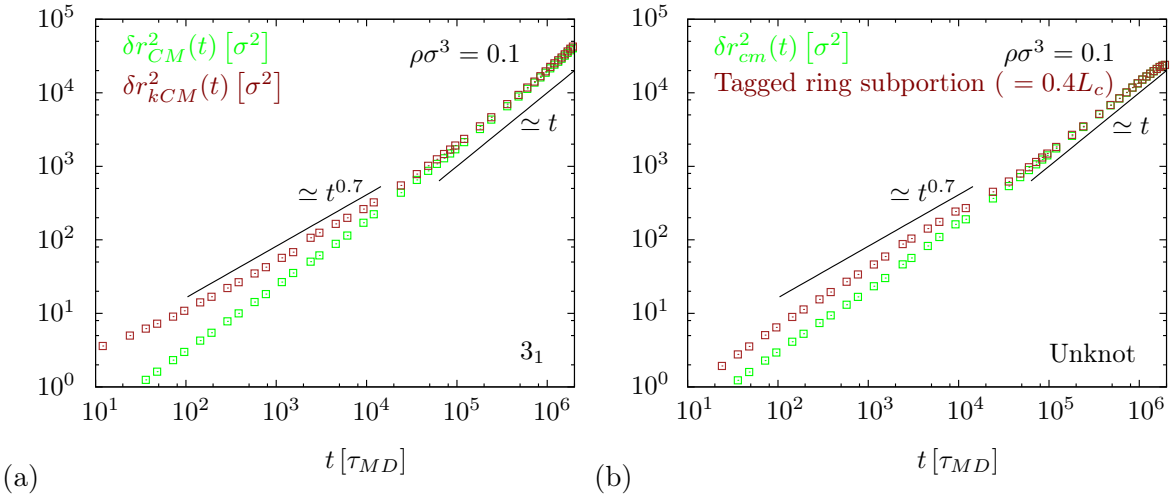

Figure 4.10: (a) Comparison between the mean-square displacement of the center of mass of trefoils ($\delta r^2_{CM}(t)$, Eq. 4.16, green symbols) and the center of mass of their knotted portion ($\delta r^2_{kCM}(t)$, Eq. 4.19, brown symbols). The motion of the knotted portion is sub-diffusive at short times, and follows the chain global displacement at larger times. (b) Comparison between the mean-square displacement of the center of mass of unknots ($\delta r^2_{CM}(t)$, Eq. 4.16, green symbols) and the center of mass of a tagged portion (brown symbols) of linear size equal to the average knot length on 3_1 rings ($\approx 0.4L_c$, Fig. 4.4).

Fig. 4.10 (left panel) shows that the diffusive behavior of the observable $\vec{r}_{kCM}$ sets in at times larger than the relaxation time of the whole chain (compare to Fig. 4.8), while a subdiffusive behavior $\sim t^{\alpha}$ with $\alpha \approx 0.7$ is seen at smaller times. Notice that the same exponent, $\alpha \approx 0.7$ was previously observed by looking at the stochastic dynamics of the center of mass of the knotted portion in isolated self-avoiding polygons on a cubic lattice [98]. Analogous plots at different monomer densities show the same subdiffusive behavior with an exponent α that decreases slightly with ρ (not shown). We have then calculated the mean square displacement of a randomly-picked ring portion spanning 40% of the contour length (the typical size of the knotted portion, fig. 4.4) of the unknotted ring. As shown in Fig. 4.10b it was found that the tagged portion moves very compatibly with the motion of the knotted part, showing an analogous crossover from a diffusive to a subdiffusive behavior. This suggests that the underlying mechanism of the subdiffusive regime of the "quenched" knotted part is similar to the one that governs the subdiffusive behavior of any other (topologically trivial) tagged subregion of the ring. Note, however, that the effective length of the rings considered here is very small compared to the one of the lattice rings studied in [98], and no simple argument is presently available to predict

if the $\alpha \approx 0.7$ exponent is expected to be maintained for increasing contour lengths where the size of the knotted portion is supposed to be negligible with respect to the one of the whole ring.

In conclusion, the above results provide a vivid picture of the key features of the dynamics of the knotted region. Specifically, they illustrate that the displacement of the knot center of mass follows "passively" the one of the whole ring because of the very long times required by the knot to slide along the ring.

4.4 Summary

In this chapter we reported on a systematic computational study of the equilibrium and dynamics of solutions of unconcatenated ring polymers with different knot topology. Specifically, molecular dynamics simulations (with no explicit treatment of the solvent) at fixed-volume and constant temperature were carried out on bead-spring models of semiflexible unknotted and trefoil-knotted rings for several solution densities. This framework was used to explore the extent to which the interplay between topological constraints (knotting) and the geometrical self (intra-chain) and mutual (inter-chain) entanglements affect both the equilibrium and the dynamical properties of the rings. The study complements previous investigations of dense solutions of unlinked and unknotted ring polymers of various contour lengths.

Regarding the equilibrium metric properties it is found that changes of the inter-chain or intra-chain entanglement operated by varying the solution density and/or ring topology, affect modestly the average ring size and shape compared to the infinitely-diluted case. Specifically, the root mean radius of gyration of both unknotted and trefoil rings at the highest solution densities (occupied volume fraction equal to 0.4) are at most about 40% smaller than in the unconstrained case. At all densities, trefoils are smaller (between 10% and 20% in linear size) and slightly more globular than unknots. Yet the average exposed surface of rings with different topology is practically the same and about constant at all densities. These results offer an interesting insight regarding the compactness of the rings and, in particular, they indicate that the moderate decrease in ring size following the increasing intra- and inter-chain entanglement does not preclude the persistence of voids and cavities within the rings convex hull so that the exposed surface area is about the same as for unconstrained isolated rings.

The weak dependence of the overall ring geometric features on solution density prompts the question of whether, for knotted rings, the metric properties of the knotted ring portion are weakly affected too. By knotted ring portion we refer to the shortest arc that accommodates the knot. It is found that the length of the average size of the knotted ring portion is practically insensitive to density variations.

While ring equilibrium metric properties are only weakly affected by variations of solution density and ring topology, the opposite holds for kinetic properties. The characteristic times of ring size relaxation, reorientation, and center of mass diffusion change by one order of magnitude across the considered density range.

Further topology-dependent aspects of ring kinetics were highlighted by monitoring various kinetic observables of the ring knotted portion. Specifically we focused on how such region displaces in space and along the ring contour. The backbone motion is found to follow standard one-dimensional diffusion and the corresponding diffusion coefficient is smaller (much smaller at low concentrations) than the one of the ring center of mass. Consequently, for time scales over which a ring moves appreciably in space, its knotted portion remains practically quenched and, as we verified, diffuses in space as any other equally-long tagged portion of the ring.

In summary, the results presented here offer novel insights into the impact of intra-chain and inter-chain entanglement in solutions of ring polymers. The mild dependence of equilibrium metric properties on both the above-mentioned effects has no parallel with the behavior of dense systems of rings obtained by three-dimensional spatial (spherical) confinement. This suggests that an interesting novel avenue to address in future work would be to examine analogous effects for dense systems of rings obtained by two-and one-dimensional confinement (slabs and channels), which are increasingly adopted for advanced polymer micromanipulations. By converse, the sensitive dependence of various ring kinetic properties on solution density and ring topology suggests that both effects should be relevant to the studies of rheology and transport properties in semi-dilute solutions of circular polymers.

Chapter 5

Multiscale entanglement in spherically confined knotted rings

It is a well known fact that wires and cables that are packaged disorderly tend to be badly entangled and knotted. This common experience bears analogies with numerical and experimental studies on the knotting probabilities of geometrically confined polymers (see [78] for a review). Since many biopolymers and particularly DNA are often subject to confinement inside regions with calliper size that is smaller than their contour length (e.g. the Eukariotic nucleus, mitochondria, bacteria, bacteriophage capsids..), it is interesting to study the relationship and interplay between spatial confinement and topological entanglement. In this chapter we address this interplay for spherically confined polymers.

A first breakthrough in the problem could be made by establishing what portion of a spherically confined knotted polymer ring is occupied by the knot. As we have seen in § 2.3 this fraction can be measured in two different ways, which convey different information about the entanglement related to the knot. The bottom-up knot location scheme, on one hand, gives the length, l_{sk}, of the shortest knotted arc having the same topology of the whole chain. On the other hand the top-down knot location scheme gives the length, l_k, of the shortest knotted arc which not only has the same topology of the whole ring, but can be continuosly extended to encompass the whole of it. The difference (or lack of) between l_k and l_{sk} therefore gives further insight into the degree of entanglement of knotted polymer rings.

As a prototypical context to examine this problem we consider semi-flexible, self-avoiding rings of cylinders with the simplest knotted topology, a 3_1 knot, and subject to isotropic spatial confinement. In such a system, by varying the size of the confining region, the degree of geometrical complexity can be changed and related to the equilibrium properties of the knotted ring portion.

As the bottom-up knot length l_{sk} can correspond to the length of ephemeral knots on the ring, we start our investigation by studying the top-down knot length l_k. In § 5.2.1 we characterize how the knot length l_k depends on the ring contour length, L_c and the radius of the confining sphere, R_c. In the no- and strong-confinement cases we observe weak knot localization and complete knot delocalization, respectively. In § 5.2.2 we show that the complex interplay of l_k, L_c and R_c that seamlessly bridges these two limits can be encompassed by a simple scaling argument based on deflection theory. Finally in § 5.2.3 we consider the behaviour of the bottom-up knotted portion as well and show that its length l_{sk} has a qualitatively different behaviour upon increasing confinement of the rings, leading us to the conclusion that topological entanglement in spherically confined rings has a multiscale character.

5.1 Methods

5.1.1 Model

We shall consider ring polymers modelled as flexible rings of cylinders and subject them to spherical confinement. For definiteness, the properties of the model rings are set to match those of dsDNA. Specifically, the cylinder diameter and long axis are set equal to $d = 2.5nm$ and $b = 10nm$, respectively. The latter quantity is ten times smaller than the DNA Kuhn length (equal to twice the persistence length, $l_p = 50nm$), thus ensuring a fine discretization of the model DNA. The system energy includes steric hindrance of non consecutive cylinders plus a bending potential.

We denote the coordinate of the ring vertices by $\vec{r}_1, \vec{r}_2, \ldots, \vec{r}_{N+1} \equiv \vec{r}_1$. Bond vectors are defined as $\vec{t}_i = \vec{r}_{i+1} - \vec{r}_i$, again with $\vec{t}_{N+1} \equiv \vec{t}_1$. Steric hindrance is enforced by penalizing with a large (practically infinite) energy cost all configurations in which two non-consecutive cylinders come too close. The bending rigidity potential has the standard Kratky-Porod form

$$E_b = -K_b T \frac{l_p}{b} \sum_{i=1}^{N} \vec{t}_i \cdot \vec{t}_{i+1} \tag{5.1}$$

with temperature T set to 300K.

We consider rings of $N = 50, ...250$ cylinders, corresponding to contour lengths, $L_c = Nb$ ranging from 500 nm to 2.5 μm. This range allows for probing changes in knot localization going from semiflexible to fully-flexible rings [3], as well as for examining

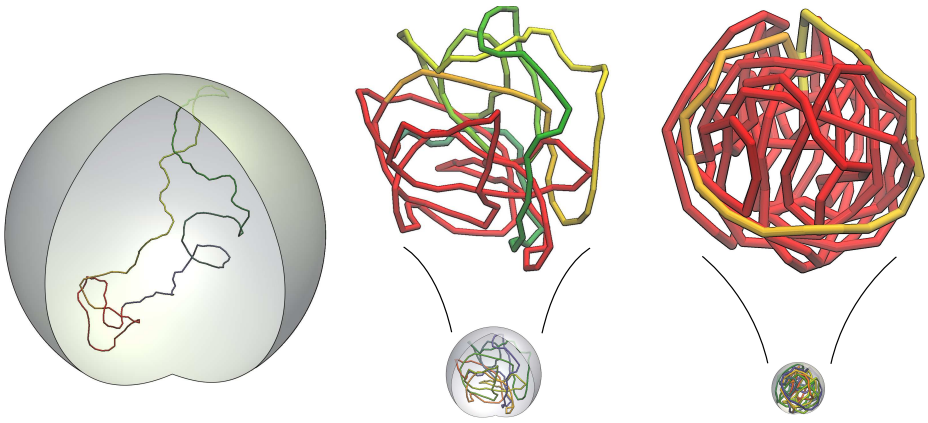

Figure 5.1: Typical configurations of trefoil-knotted rings with $N = 200$ cylinders at different levels of confinement. The encapsidated configurations for $R_c = 6$ and $R_c = 3$ are magnified for ease of visualization. The top-down knotted portion of the rings is shown in red. This and other images in this chapter have been adapted from ref. [138].

the effect of the interplay between L_c, l_p and the radius of the confining sphere, R_c. For simplicity of notation in the following all lengthscales are expressed in units of b.

5.1.2 Sampling

Because compact ring configurations are entropically disfavoured with respect to unconstrained ones, simple stochastic sampling schemes cannot be effectively used to generate spatially confined rings [85]. An analogous entropic attrition works against having a sizeable population of knots of a given type, trefoils in our case, at all levels of confinement [85]. To overcome these two difficulties we used a biased Multiple-Markov-chain sampling scheme designed after the procedure adopted in [86, 87] and described in detail in the review of ref. [85].

In short, a series of 24 markovian replicas is run in parallel by evolving different stochastic trajectories of closed rings. For each replica, ring configurations are evolved using crankshaft and hedgehog Monte Carlo moves [59]. The moves preserve the length of the rings, but not the topology, consistently with ergodicity requirements [4, 85]. In fact, even when the configurations before and after the move are self-avoiding, the move itself may involve self-crossings of the chain. For each replica a newly generated ring, $\Gamma = \{\vec{r}_1, \vec{r}_2, \ldots, \vec{r}_N, \vec{r}_{N+1} = \vec{r}_1\}$ is accepted according to the standard Metropolis

algorithm with generalised canonical weight

$$W(\Gamma) = \exp[E_b(\Gamma) + p\, R_c(\Gamma) + \Delta_\tau(\Gamma)].$$

In this expression R_c is the radius of the sphere containing Γ (calculated as the largest distance of the cylinder vertices from the ring geometric center) and p is a pressure-like parameter whose value is set differently for different replicas, so to sample rings with varying degree of confinement. $\Delta_\tau(\Gamma)$ is a topology-dependent potential energy introduced to reject knots with more than 7 minimal crossings (according to the Alexander determinants in -1 and -2 see § 1.1.5). $\Delta_\tau(\Gamma)$ takes the value 0 for ring configurations with 7 crossings or less or a very large, practically infinite value, for rings with more complex topologies. To sample more efficiently the configuration space at different levels of compactification, swaps of configurations between replicas are proposed and accepted/rejected on the basis of the generalized metropolis criterion described in ref. [133, 85].

For each value of N the procedure is used to generate at least $\sim 10^7$ configurations with varying compactness and topology. For the *a posteriori* data analysis we pick, out of the generated rings, an uncorrelated subset with 3_1 topology (positively established with the KNOTFIND algorithm [47]).

A thermodynamic reweighting technique [86] is applied to the set of trefoil rings to remove the pressure bias p and obtain canonical averages for the observables of an equilibrated set of rings confined within a sphere of radius R_c.

5.1.3 Identifying the knotted portions

As in previous chapters we use the top-down and bottom-up knot location schemes introduced in § 2.3 and denote the obtained knot lengths l_k and l_{sk} respectively. To determine the topology of open ring subportions we close them using the minimally-interfering closure(see § 2.1) and compute the Alexander determinants in (-1) and (-2) of the resulting ring.

Thanks to the reliability of the minimally-interfering closure (see § 2.1) the above scheme for locating the knot can be seamlessly and robustly applied at all levels of ring compactification.

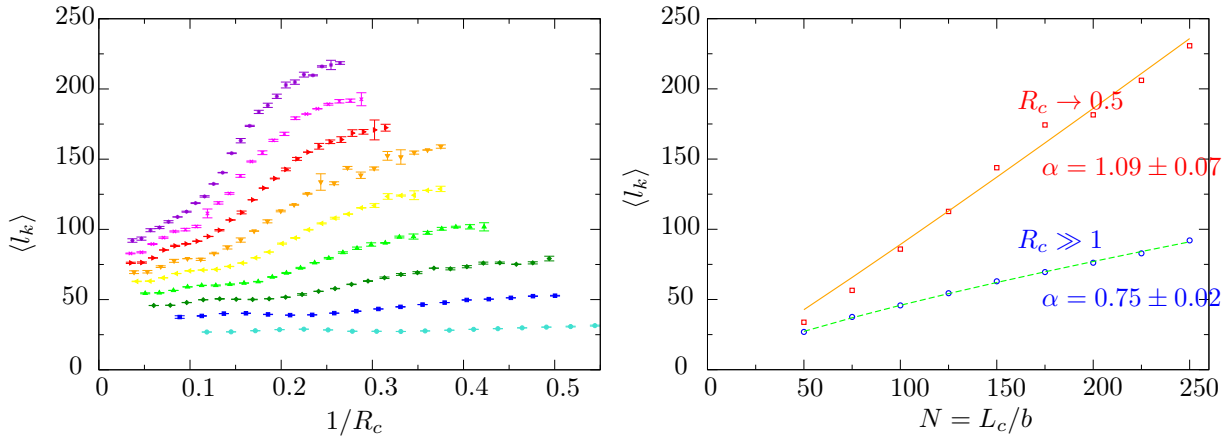

Figure 5.2: (a) Knot length l_k (according to the top down scheme) as a function of progressive confinement $1/R_c$ for different ring lengths. (b) Scaling of l_k in the limiting cases of no confinement ($R_c \gg 1$, blue circles) and strong confinement ($R_c \to 0.5$, red squares).

5.2 Results and discussion

5.2.1 Behaviour of l_k for increasing confinement

The behaviour of l_k with increasing confinement $1/R_c$ is reported in Fig. 5.2 (a). Two important facts emerge: for a given ring contour length, L_c, the increased confinement is parallelled by an increase of the length of the knotted arc, l_k; at the same time, for a given size of the confining sphere one has that l_k increases with L_c. The growth of l_k with $1/R_c$ is characterized by a mild growth for low confinement, followed by a sharp increase as the confining radius is further reduced. Finally, for R_c approaching 0.5, the maximum attainable compression of a ring of cylinders of length b, l_k reaches a plateau whose value depends on L_c.

As a first step towards a comprehensive rationalization of the results we examine the l_k versus L_c behaviour in the no- and strong-confinement limits, $R_c \gg 1$ and $R_c \to 0.5$, which are shown in Fig. 5.2 (b). In the unconstrained case, it is seen that l_k increases as a power of L_c: $l_k(R_c \to \infty) \propto L_c^{\alpha}$ with $\alpha = 0.75 \pm 0.02$ compatibly with the value reported in § 2.3.4. As we saw there, the sublinear increase implies that l_k/L_c vanishes for increasing L_c, resulting in a weak knot localization Consistent with previous results on knot localization for unconstrained rings both on- and off-lattice [76, 145, 73].

To obtain the values of l_k in the limit of strong confinement, we fit the curves of Fig. 5.2 (a) with the function $y = a_0 - a_1 e^{-x/a_2}$ to extract the value of l_k on the plateau,

$l_k^c \equiv a_0$. A power-law dependence of l_k on L_c provides a good fit of the data for strong confinement too but in this case $\alpha = 1.09 \pm 0.07$. This is compatible with a linear dependence of l_k on L_c thus implying a full delocalization of the knot in equilibrated rings subject to severe three-dimensional confinement. To the best of our knowledge this fact has not been established before. However, it is worth pointing out that knot delocalization has been previously observed for θ-collapsed knotted rings [76, 145, 73]. The analogy with our findings is noteworthy since the ring metric properties are dictated purely by equilibrium thermodynamics for collapsed rings while spatial constraints are also at play for confinement.

5.2.2 Rationalization: arc deflection length

Having characterized the limiting behaviour of l_k for no- and strong-confinement we turn our attention to the intermediate regime intervening between the no- and strong-confinement limits and show that the complex behaviour of Fig. 5.2 (a) can be rationalized in terms of a surprisingly simple relationship involving the length scales L_c, R_c and l_k. To this purpose we first observe that upon increasing confinement the geometric characteristics of the rings come to resemble those of uniformly filled spheres. We consider in particular the eigenvalues of the tensor of gyration (see eq. 4.10). Fig. 5.3 (a) shows that for increasing confinement $1/R_c$ they become close to the eigenvalue of a uniformly-filled sphere of radius R_c.

The approximately uniform filling of the confining sphere by mildly- or strongly-confined rings is illustrated also by the mean squared end-to-end separation, R_{ee}^2, of ring portions of different arclength, s, reported in Fig. 5.3 (b). The profile of $R_{ee}^2(s)$ is noticeably flattened and its plateau value is about $6/5R_c^2$, which is the mean square distance of two points inside a spherical volume of radius R_c.

Following those observations, in analogy with the deflection argument originally introduced for polymers in channels [97], we define a deflection arclength $\bar{s}$ as the value of s at which the squared end-to-end distance of a Kratky-Porod chain equals the plateau value $6/5R_c^2$ characteristic of a uniformly filled sphere:

$$R_{ee}^2(\bar{s}) = 2l_p\bar{s}\left[1 - \frac{l_p}{\bar{s}}\left(1 - e^{-\frac{\bar{s}}{l_p}}\right)\right] = \frac{6}{5}R_c^2 \ . \tag{5.2}$$

$\bar{s}$ is the nominal arclength of unrestricted ring-portions that are just long enough to hit

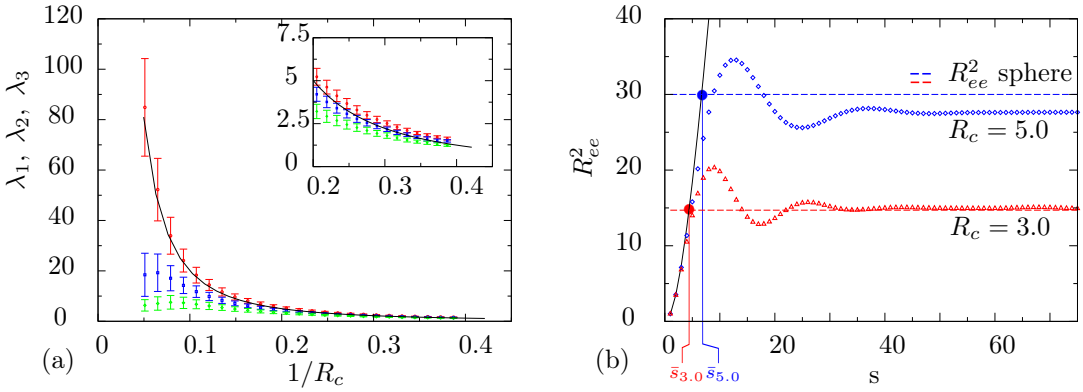

Figure 5.3: (a) Average eigenvalues of the rings gyration matrix, λ_1, λ_2, λ_3 (largest to smallest), shown as a function of the radius of the confining spherical cavity R_c. Errorbars report the standard deviation around the average value. The inset shows the data for high spatial confinement. (b) Mean squared end-to-end distance, R^2_{ee}, of arcs of length s in rings of $N = 150$ cylinders at different levels of confinement. The dashed horizontal line indicates the reference value equal to $6/5R_c^2$ while the continuous line shows the expected R^2_{ee} for an unconstrained, non-self-avoiding Kratky-Porod (KP) chain. The intersection of these reference lines determines the nominal deflection arclength, $\bar{s}$ highlighted by the dropline.

the sphere boundary and, by inverting (5.2), can be expressed in terms of the principal branch of the Lambert W function [23],

$$\bar{s}/l_p = 1 + y + W(-\exp[-1-y]) \tag{5.3}$$

where $y \equiv 3R_c^2/5l_p^2$.

The deflection arclength is crucial for rationalizing the results of Fig. 5.2 (a) and (b). In particular it is plausible that confined rings that experience the same nominal number of deflections at the spherical hull boundary should have statistically similar knot lengths once rescaled by $\bar{s}$. This conjecture is supported by the scatter plot of Fig. 5.4 where the rescaled knot length is plotted against the number of nominal deflections $L_c/\bar{s}$ for rings of all considered lengths, $50 \leq N \leq 250$, and degrees of confinement.

Despite the heterogeneity of the original data sets (see Fig. 5.2 (a)), the plot displays a striking collapse of the data points. A broadening of the curves is seen only in the limit of unconstrained rings, where indeed, the deflection length looses meaning. We stress that, because $\bar{s}$ is calculated deterministically, no single adjustable parameter was introduced to obtain the collapse in Fig. 5.2. The collapsed curve exhibits an asymptotic linear trend thus reinforcing the delocalization result of Fig. 5.2 (b).

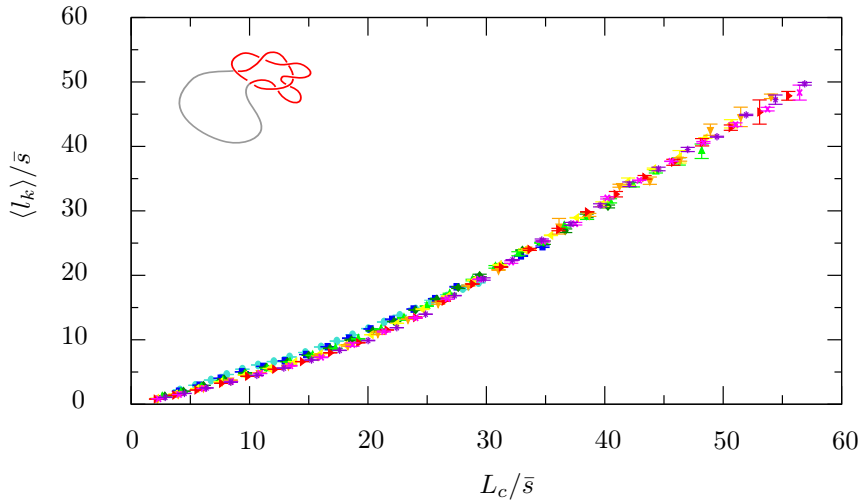

Figure 5.4: Collapse of the same data points as in Fig. 5.2 (a) obtained by rescaling l_k and L_c by $\bar{s}$. The slope of the line fitting the data for $\frac{L_c}{\bar{s}} > 40$ is 1.09 ± 0.02.

5.2.3 Multiscale character of the knot length: l_k and l_{sk}

Apart from the top-down knot length l_k considered up to here, we saw that another length, the "bottom-up" knot length l_{sk}, can be associated to a knotted portion. We recall that while l_k is the length of the shortest portion of the ring which shares the same topology of the whole ring *and* can be extended to encompass the whole ring, this latter requirement is not enforced for the knotted arc identified by the bottom-up scheme, which can consequently correspond to an ephemeral knot (because it can be contained in a longer arc with different topology, e.g. an unknot) [91].

In § 2.3.4 we saw that the knot lengths l_k and l_{sk} diverge for increasing ring length. It is intriguing to correlate such divergence with an increasing geometrical entanglement of the longer rings. On the other hand, we saw in § 4.2.3 that the increase in geometrical entanglement caused by the presence of other rings in solution does not reflect in a difference between l_k and l_{sk}. It is therefore interesting to compare the results given by the two schemes in the present contest, in which trefoil rings are subject to increasing geometrical entanglement due to spherical compactification.

The difference between the knotted portions identified by the two schemes is clearly exemplified in Fig. 5.5 which reports the knotted portions identified by the top-down and the bottom-up schemes for a confined ring of 250 edges. While the top-down knotted portion takes almost the whole ring, the bottom-up knotted portion is seen to be formed

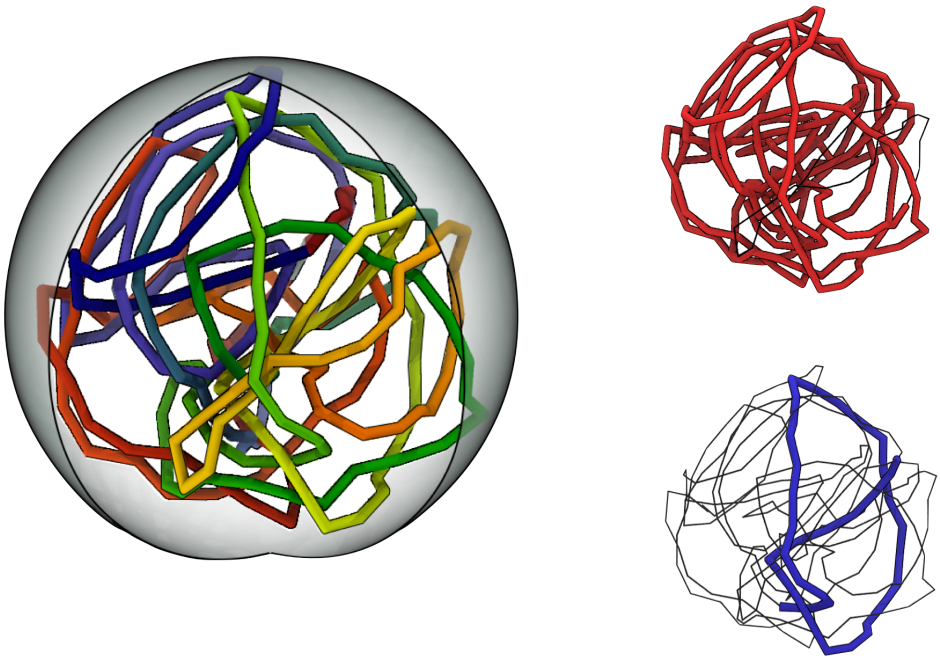

Figure 5.5: The knotted portions identified by the top-down scheme (Red) and the bottom-up scheme (blue) for a compact ring with 250 edges.

by a short trefoil-knotted arc, which is repeatedly threaded through by the rest of the chain and may therefore correspond to an ephemeral knot.

Fig. 5.6 illustrates how the length of the shortest knotted arc, l_{sk}, behaves for increasing confinement and compares it with l_k. It is seen that for no- or mildly-constrained rings, when the ring geometrical entanglement is minimal, the two measures are in good accord. However, upon increasing confinement they progressively diverge. Compared with the divergence observed in § 2.3.4 for rings of increasing length, the divergence we observe here is not only quantitative, but qualitative as well. While l_k saturates at almost the whole ring length in the limit of strong confinement this is not the case for l_{sk}. On the contrary, it is clear from Fig. 5.7 that the knotted portion measured by the bottom-up scheme becomes smaller and smaller with increasing compactification, much below the typical dimension of the knots in unconstrained rings.

Recalling that l_{sk} and l_k provide lower and upper limits to the range of arclengths over which non-trivial topological entanglements (after arc closure) are observed, the divergence of the two metrics indicates that the entanglement cannot be described by a single length scale but it displays a multiscale behaviour that amplifies upon increasing

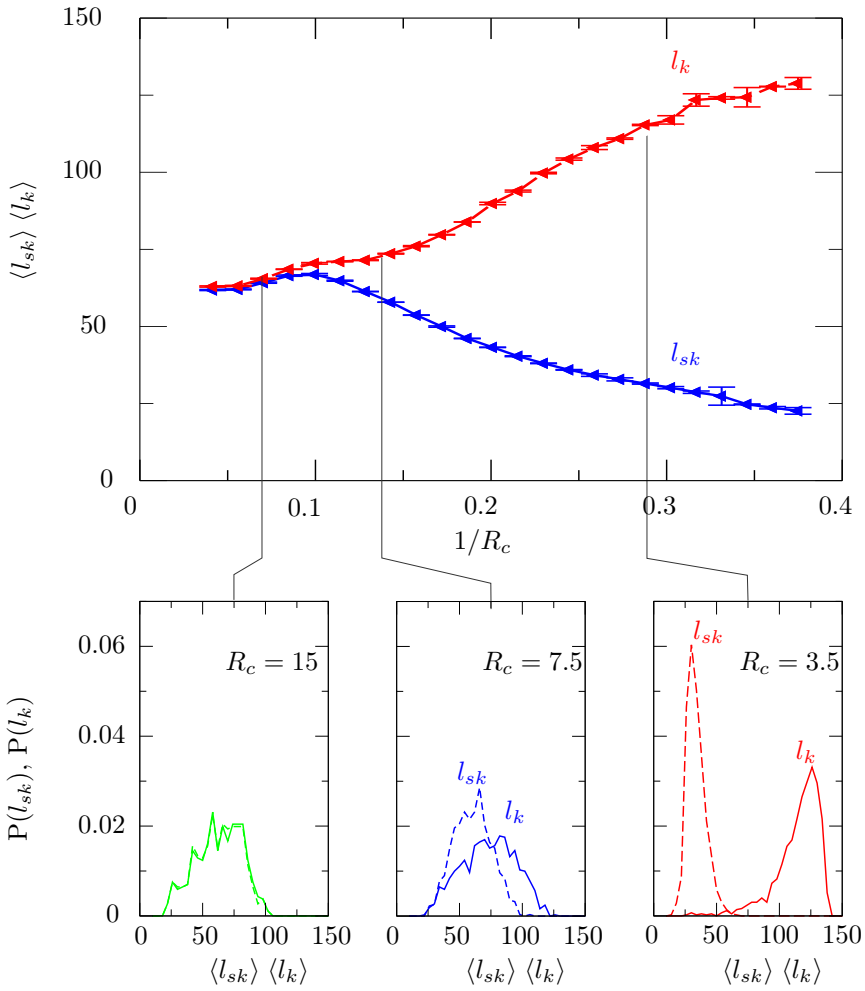

Figure 5.6: Top panel: dependence of knot length, l_k, and the shortest knot length, l_s, on confinement for rings of $N = 150$ cylinders. Bottom panels: probability distributions of the knot lengths l_{sk}, l_k for three different values of R_c.

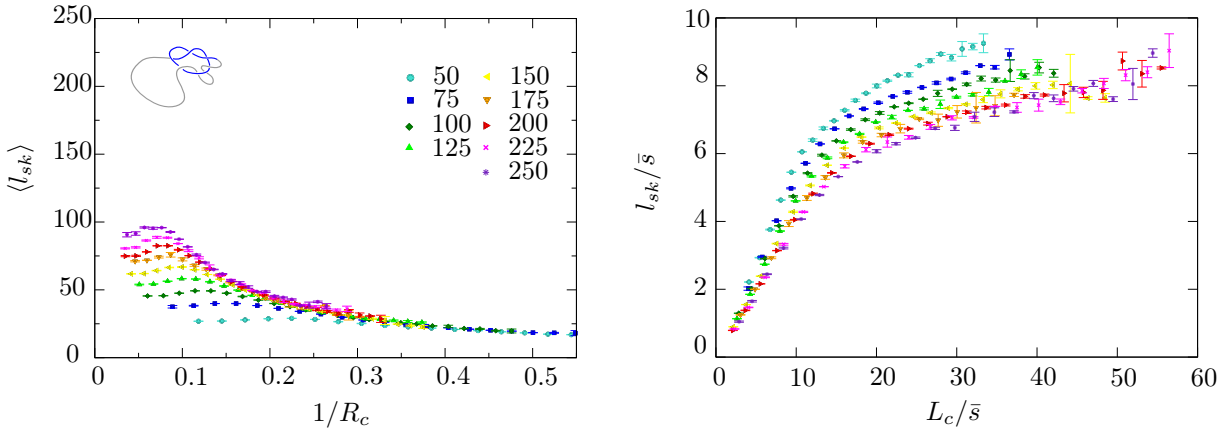

Figure 5.7: (a) Dependence of bottom-up knot length l_{sk} on the confinement $1/R_c$ for different length of the confined ring. (b) Scatter plot of $l_s/\bar{s}$ versus $L_c/\bar{s}$ for rings of all lengths and degree of confinement.

confinement.

Similarly to the case of the proper knot length, l_k, the concept of deflection arclength is useful for rationalizing the interplay of l_s, R_c and L_c. In fact, l_s expectedly results from the balance between (a) the increasing probability that a knot can be tied with a minimal (nominal) number of deflected segments/cylinders for longer and more confined rings and (b) the decreasing probability that the complementary arc is unknotted.

In the plot of Fig. 5.7 (b) it is seen that, for increasing L_c, the $l_s/\bar{s}$ data tend to approach a limiting curve that has a linear dependence on $L_c/\bar{s}$. The results indicate that for medium and strong confinement the length of the smallest, and possibly ephemeral, knot, l_s, increases approximately linearly both with L_c at fixed R_c and with R_c at fixed L_c. Together with the behaviour of l_k, the results provide a quantitative basis for the multiscale character of the ring entanglement that sets in for increasing confinement.

5.3 Summary

To summarize, we used the top-down and bottom-up knot location schemes to characterize the interplay between geometrical and topological entanglement in spherically confined polymer rings. At variance with the case of ring solutions discussed in chapter 4, we found that the ring compactification produced by spherical confinement results in a multiscale character of the knotted portion. This is characterized by a qualitative divergence of

the two knot lengths l_k and l_{sk}: while l_k follows a complete delocalization trend, the bottom-up knot length l_{sk} becomes smaller and smaller for increasing confinement.

We further showed that the complex behaviour of l_{sk} and l_k at moderate and high degrees of confinement can be rationalised in terms of a deflection arclength. The latter therefore appears to be a key quantity to characterize the complex interplay of the geometry and topology in confined polymer rings, which reverberates in the above mentioned multiscale entanglement. This observation prompts the question of whether an analogous concept and scaling argument can be introduced to characterize and rationalize the entanglement found in other systems of densely-packed circular polymers, such as for example theta-collapsed rings [42, 145, 76].

Our results have direct bearings on the relevant problem of viral DNA ejection into infected cells [81]. This problem will be part of the focus of next chapter, in which we will show that this crucial step of the viral infection is not hindered by the presence of knots, in the packaged genome, because the latter are highly delocalized [78, 80].

Chapter 6

DNA-DNA interactions and DNA knotting in bacteriopaghes

[1]

In the previous chapters we studied how topological entanglement influenced physical properties of polymers by focusing on polymers with fixed topology. By varying parameters like the polymer length or the degree of confinement (either geometrical or due to the presence of other rings) we studied the effects of knots on the physical properties of polymer rings. In this chapter we adopt a complementary approach, using topological analysis (the properties of the knot spectrum) to infer the physical properties of packaged bacteriophage genome. With their μm long dsDNA genome packaged inside capsids whose diameter are in the $50 - 80$ nm range, bacteriophages achieve the highest level of compactification and arguably bring the simplest example of genome organization in living organisms [31, 40]. Thanks to experimental advancements in single-molecule manipulation and imaging techniques [125], many aspects of the process of DNA loading inside the phage capsid, and its subsequent ejection are now understood in detail [65, 40, 35, 19, 72]. Nevertheless, the problem of DNA organization and storage inside the capsid (i.e. after completion of the loading process and before ejection) remains elusive.

There are two main kinds of experimental assays for genome organization in bacteriophages, both giving important terms of reference for any study of dsDNA packaging. These assays are cryo-electron microscopy (cryo-EM) probing the geometry and gel-electrophoresis probing the topology of the confined genome.

[1]Originally published on PNAS **106**, 2009, pages 22269-2274: *DNA-DNA interactions in bacteriophage capsids are responsible for the observed knotting.* By D. Marenduzzo, E. Orlandini, A. Stasiak, D.W. Sumners, L. Tubiana and C. Micheletti. Research originally designed by D.M., E.O., D.W.S. and C.M.; simulations performed by D.M.; data analyzed by E.O., L.T. and C.M.

Cryo-EM techniques allow to reconstruct the three-dimensional structure of packaged dsDNA starting from electron-density distributions. Recent studies performed using advanced cryo-EM techniques, that do not assume any *a priori* simmetry to perform the three dimensional structure reconstruction, have revealed that close to the capsid internal wall, the DNA of bacteriophages $\epsilon 15$ [52] and $\phi 29$ [22] is arranged in neatly ordered concentric shells, each formed by stacked hoops of DNA. The distance between neighbouring DNA hoops and shells have been measured to be $2.5nm$ equal to DNA hydration radius. An increasingly disordered DNA arrangement, possibly due to the loss of experimental resolution, was instead observed when moving toward the interior of the capsid. This data therefore suggested a DNA arrangement compatible with the *coaxial inverse spool model*.

Gel-electrophoresis analysis allows for establishing the topology of DNA rings by correlating it to their migration velocity in an agarose gel under the influence of a uniform electric field. Rings with different knots migrate at different velocities, giving origin to distinct DNA bands, which can be weigthed to obtain the relative probability of different knots [123, 129].

Gel-electrophoresis assays were carried out on specific mutants of the P2 and P4 bacteriophages. The P4 genome is a $10 - 11.6$ Kb DNA molecule with 19-bp cohesive ends. Cohesive ends are complementary sequences of single-stranded DNA that can anneal together forming a nicked DNA ring and thus capturing any knot present in the P4 genome. Once the ends anneal, their interaction is so stable that the topology of the molecules is fixed during further experimental manipulation [149, 68, 67].

The analysis of the knot spectrum was performed both on mature phages where one DNA end is kept within the collar of the phage, therefore preventing ends annealing before extraction, and on tailless mutants in which both ends were free to meet and anneal inside the capsid [9, 8]. The knot spectrum obtained in those two cases provided several important indications about genome organization within phages.

First, 47% of the DNA molecules were found to be knotted in mature P4 phages [9]. This already considerable fraction increases to a staggering 95% for molecules coming from the tailless mutant [67, 9]. Second, measured knot resulted to be highly complex as indicated by an average minimal crossing number of $\simeq 26$. Minimal crossing number ranging up to 40 were reported [9]. For comparison, the knotting probability of P4 DNA circularized in solution is 3% with a knot spectrum characterized by simple knots with average minimum crossing number of $\simeq 5$ [9]. Finally, the population of the simplest

types of knots was found to be strongly biased towards torus knots and against achiral ones [8]. In particular, the populations of the achiral knot 4_1 and of the twist knot 5_2 were much smaller than those of the torus knots 3_1 and 5_1.

The observed knot spectrum provides an important, albeit indirect, indication of DNA arrangement, as it cannot be explained by simple models for semiflexible polymers subject to spatial confinement. For example, the extremely high (95%) knotting probability is at odds with predictions from DNA-packaging models where ordered and mostly unknotted spools are obtained as a result of minimization of the bending energy [7]. Accounting for thermal disorder in semiflexible polymers confined in a spherical cavity produces, on the other hand, highly entangled configurations [37]. While the resulting disorder reflects in a high fraction of knots and high knot complexity, it fails to account for the observed bias among the simplest types of knots [86, 87]. Arsuaga et al. observed that the latter can been qualitatively reproduced in simulations of mildly confined ring polymers, either sampled with a preferential bias for configurations with high writhe [8] or generated in spool like configurations [6]. In this regard, it is important to observe that both the writhe and the spooling provide a quantitative measure of *global* geometric properties. This leads to the question of what plausible *local* DNA interactions are responsible for the observed knot spectrum (possibly, but not necessarily, also resulting in the proposed biases).

In this chapter we show that several experimentally accessible features of viral genome packaging can be reproduced and understood via a suitable mesoscopic model of double-stranded DNA which can be studied by computer simulations. In addition to accounting for the well known bending rigidity and thickness of the DNA, our model incorporates a crucial phenomenological aspect, the fact that contacting DNA segments are chiral and meet with a preferred twist angle. To the best of our knowledge, this interaction has not been previously considered in models for DNA organisation inside bacteriophages, although it is known to be ultimately responsible for the appearance of cholesteric phases in dense suspensions of DNA segments [112, 17, 128, 61].

6.1 Model and methods

6.1.1 DNA model

We model dsDNA as a open semiflexible chain of N spherical beads of diameter $\sigma = 2.5$ nm (each bead therefore comprises slightly less than 8 base pairs). The P4 genome we study consists of 10 kilo-base pairs[2] (kb) and hence is modelled with chains of 1360 beads. Mutant phages with 4.7 kb-long genome were simulated using chains of 640 beads. The P4 capsid is approximated as a non-deformable sphere with a diameter of 45nm [29].

In the following we shall indicate with $\vec{r}_i$ the position of the center of the ith bead and with $\vec{b}_i \equiv \vec{r}_{i+1} - \vec{r}_i$ the virtual bond vector connecting beads i and $i+1$.

The connectivity of the chain is treated within the finitely-extensible nonlinear elastic (FENE) model [62], and by further requiring that the bond length is never either smaller than 0.7 σ or larger than 1.3 σ.

The bending rigidity of DNA is captured with a standard Kratky-Porod potential:

$$V^{bend} = -\kappa_b \sum_{i=1}^{N-1} \frac{\vec{b}_i \cdot \vec{b}_{i+1}}{|\vec{b}_i||\vec{b}_{i+1}|}. \tag{6.1}$$

and the bending energy amplitude is set so to reproduce the known persistence length (l_p = 50nm) of unconstrained DNA [18], $\kappa_b = {}^{K_B T l_p}/_{\sigma}$, where K_B is the Boltzmann constant and $T = 300\,K$ is the temperature. .

The mesoscopic DNA model includes three types of chain self-interaction, namely Van der Waals, screened electrostatic and cholesteric interactions [130]. The Van der Waals interaction is modelled using a pairwise Lennard-Jones potential

$$V^{LJ} = \left\{ \epsilon \sum_{i,j>i} \left[\left(\frac{\sigma}{|\vec{r}_{ij}|} \right)^{12} - \left(\frac{\sigma}{|\vec{r}_{ij}|} \right)^{6} \right] + \frac{\epsilon}{4} \right\} \theta[r - 2^{1/6}\sigma] \tag{6.2}$$

where $\epsilon = \frac{2}{5}\ k_B T$, and $\vec{r}_{ij} = \vec{r}_i - \vec{r}_j$.

Like previous work (see e.g. [8, 37, 87, 57, 108, 77, 104]) we build on the notion that viral capsids are permeable to ions in solution [66] which effectively screen electrostatic interactions inside the capsid. Screened electrostatic interactions are accounted for via a

[2]Corresponding to mutant P4vir1 del 22 strain

Debye-H uckel potential,

$$V^{DH} = \frac{K_B T \sigma^2}{a^2} l_B \sum_i \sum_{j>i} \frac{1}{|\vec{r}_{ij}|} e^{(-|\vec{r}_{ij}|/l_D)} \tag{6.3}$$

where l_B is the Bjerrum length (0.7 nm in water), a is the distance between two elementary charges (0.34 nm for B-DNA, see e.g. [106, 37]), and l_D is the Debye length, which we take equal to 0.9 nm (corresponding to 0.1 M solution of monovalent counterions such as NaCl).

The potential energy terms introduced above are known to be sufficient to account with remarkable detail for the main conformational properties for unconstrained DNA in solutions of high ionic strength [120].

We note that this model does not account either for DNA torsional rigidity or for desolvation effects. The latter are very important in systems where DNA strands are packed at interaxial distances smaller than 3 nm [130]. For the particular systems considered here model calculations [108, 51] indicate that the expected average separation of the packaged DNA ought to be larger than this spatial threshold (see Fig. 6.4) and therefore, to maintain the model complexity at a minimal level, no attempt is made to incorporate effects resulting from interaction with the solvent.

Cholesteric interaction

As discussed later, the ingredients introduced thus far alone are not sufficient to reproduce either the cryo-EM or the P4 DNA knotting data. To make contact with these experiments we include another crucial term in our short-ranged potential, which introduces a preferred "twist angle" between DNA segments that are close in space (Fig. 6.1). This cholesteric, twist, interaction has a strong phenomenological basis, and leads to the onset of cholesteric phases in dense solutions of DNA fragments, typically for DNA densities between about 160 and 380 mg/ml [71]. Accounting for the cholesteric interaction appears, therefore, mandatory for systems where the DNA density is larger than ∼150 mg/ml. This is the case for several phages, including P4 where a lower bound for the DNA density is ∼200 mg/ml (calculated assuming homogeneous density). Microscopically, the interaction results from an interplay of the helical nature of DNA (which favors the juxtaposition of contacting DNA segments at an angle reflecting the groove "inclination") and the interaction between the effective electrostatic charges on the double-helical molecule [21].

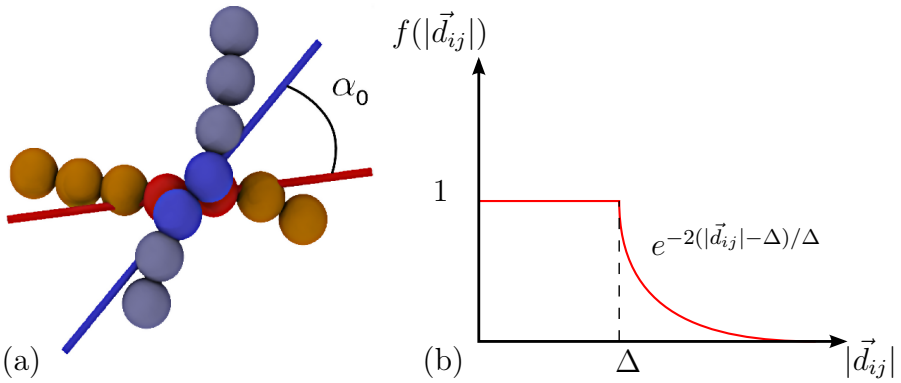

Figure 6.1: (a) The cholesteric interaction between contacting portions of DNA is introduced by favoring a preferential twist angle, α_0, between virtual bonds that have a close spatial separation. The figure highlights the pairs of consecutive beads (shown as spheres) bridged by the virtual bonds. The directionality of the latter is shown with colored sticks. The twist angle is calculated accounting for the non-oriented character of dsDNA.(b) Plot of the strength f_{ij} of the cholesteric potential as a function of the distance between two strands.This and some other images in the present chapter have been adapted from ref. [80]

Finally, the cholesteric, twist, interaction potential is:

$$V^c = \sum_i \sum_{j>i+1} k_c(\alpha - \alpha_0)^2 f(d_{ij}) \tag{6.4}$$

where

$$f(d_{ij}) = \begin{cases} 1 & \text{if} \quad |\vec{d}_{ij}| < \Delta \\ e^{-2(|\vec{d}_{ij}|-\Delta)/(\Delta)} & \text{otherwise} \end{cases} \tag{6.5}$$

where $\vec{d}_{ij} = (\vec{r}_i + \vec{r}_{i+1} - \vec{r}_j - \vec{r}_{j+1})/2$ is the distance between the centers of mass of the two bonds and Δ is the spatial range of the interaction. The twist angle, α, formed by two bonds, $\vec{b}_i$ and $\vec{b}_j$ is defined by

$$\tan\alpha = [(\vec{b}_i \times \vec{b}_j) \cdot \vec{d}_{ij}]/[(\vec{b}_i \cdot \vec{b}_j)|\vec{d}_{ij}|]. \tag{6.6}$$

With this definition of α the cholesteric interaction is *apolar*, i.e. insensitive to the reversal $\vec{b}_i \to -\vec{b}_i$ of any of the two bonds $\vec{b}_i$ and $\vec{b}_j$. The apolarity is required in consideration of the symmetry of the DNA double-helix. The preferential twist angle is indicated as α_0.

The above potential arguably represents the simplest, phenomenological, way to account for the preferential twist-angle formed by contacting DNA segments, in a chain-of-beads

DNA model. This interaction, which is responsible for the well-documented phenomenology of cholesteric phases of DNA [71], results from the complex interplay of various atomic interactions which only in recent years are being systematically addressed [61, 134].

Viable values for the phenomenological parameters k_c and α_0 can be obtained from available estimates of k_t and k_{22} measured and computed for dsDNA cholesteric phases. Specifically, it is found that α_0 should be of the order of 1° [134] though larger values could be obtained if the capsid is permeated by polycations. In addition, considering the energy associated to the introduction of a cholesteric twist in an hexagonal arrangement of parallel DNA strands [61] one has $k_c \approx 1 K_B T$ at $T = 300K$. Finally, the interaction range Δ is expected to be $\sim$ 3-5 nm [61, 21].

6.1.2 Kink-jump dynamics.

The simulations were performed using the constant-temperature kink-jump stochastic dynamics scheme [79]. This algorithm consists of the Metropolis acceptance/rejection of attempted local polymer deformations. The elementary move entails a displacement of randomly-picked bead by a fraction of its diameter. The time step associated to each kink-jump move can be mapped to the time span of 1-5 ns over which an isolated bead would diffuse over a length comparable to such a fraction. At all stages of the loading process, one end of the DNA is held fixed at a specific "portal motor" position on the surface of the spherical capsid (45nm diameter) confining the beads. The progressive insertion of the genome performed by the motor is described by the occasionally attempted addition of beads at the free end of DNA until the desired length of the chain inside the capsid is reached. The half-P4 genome packaging process lasts several ms consistent with the time-span covered by other DNA packaging simulations [104, 113]. The chain growth process is expected to capture the realistic aspects of the DNA insertion inside the capsid which is expected to mostly progress by reptation [39].

Simulations of spontaneous (free) ejection are carried out within the kink-jump scheme by modifying the potential field so that there is a hole (radius 5 nm) on the surface of the capsid from which DNA can exit. To model the presence of a collar in the phage, beads close to the opening are subjected to an harmonic potential towards the center of the opening.

6.1.3 DNA circularization and topological analysis

Packaging simulations are performed using an open chain which eventually must be closed in order to identify its topological (knotted) state. Virtually all configurations produced with this scheme had their ends at the surface, hence their topology is unambiguously identified by any outward closure like the radial closure and the minimally-interfering closure described in § 2.1.

Ring topology have been established using the KNOTFIND routine implemented in the KNOTSCAPE package [47]. Knot degree of localization have been measured using the top-down and bottom-up schemes described in § 2.3.

6.2 Results and Discussion

6.2.1 DNA organization inside the capsid

In the absence of the cholesteric term, the configurations generated by packaging the full P4 genome have the typical appearance shown in Fig. 6.2 (a). The highly disordered organization of the DNA at the inner surface of the capsid is apparent, at odds with the cryo-EM experiments.

Introducing the cholesteric orienting potential, with the interaction strength, range and amplitude of the angular bias deduced from available data [128, 21, 134], results in a dramatic change of DNA ordering at the surface (see Fig. 6.2 (b)). Projection views of the resulting arrangement, shown in Fig. 6.3, convey a level of order consistent with cryo-EM observations of various bacteriophages [52, 22]. This provides a strong indication that the introduction of this potential profoundly affects the organization of DNA inside the capsids. While the arrangement of Fig. 6.2 (b) resembles an inverse spool, the coloring scheme reveals both an appreciable degree of interweaving of the layers and the occurrence of *hairpin defects*. In particular, it is observed that there is (i) no systematic progression of the chain from bottom to top (or vice-versa) of the capsid and (ii) no unique winding directionality. These aspects, particularly (ii), reflect the apolar character of the cholesteric interaction since the symmetry of the DNA double-helix implies that the potential bias is insensitive to the directional orientation of interacting DNA segments.

The analysis of the DNA packaging process reveals that initially the DNA chain tends

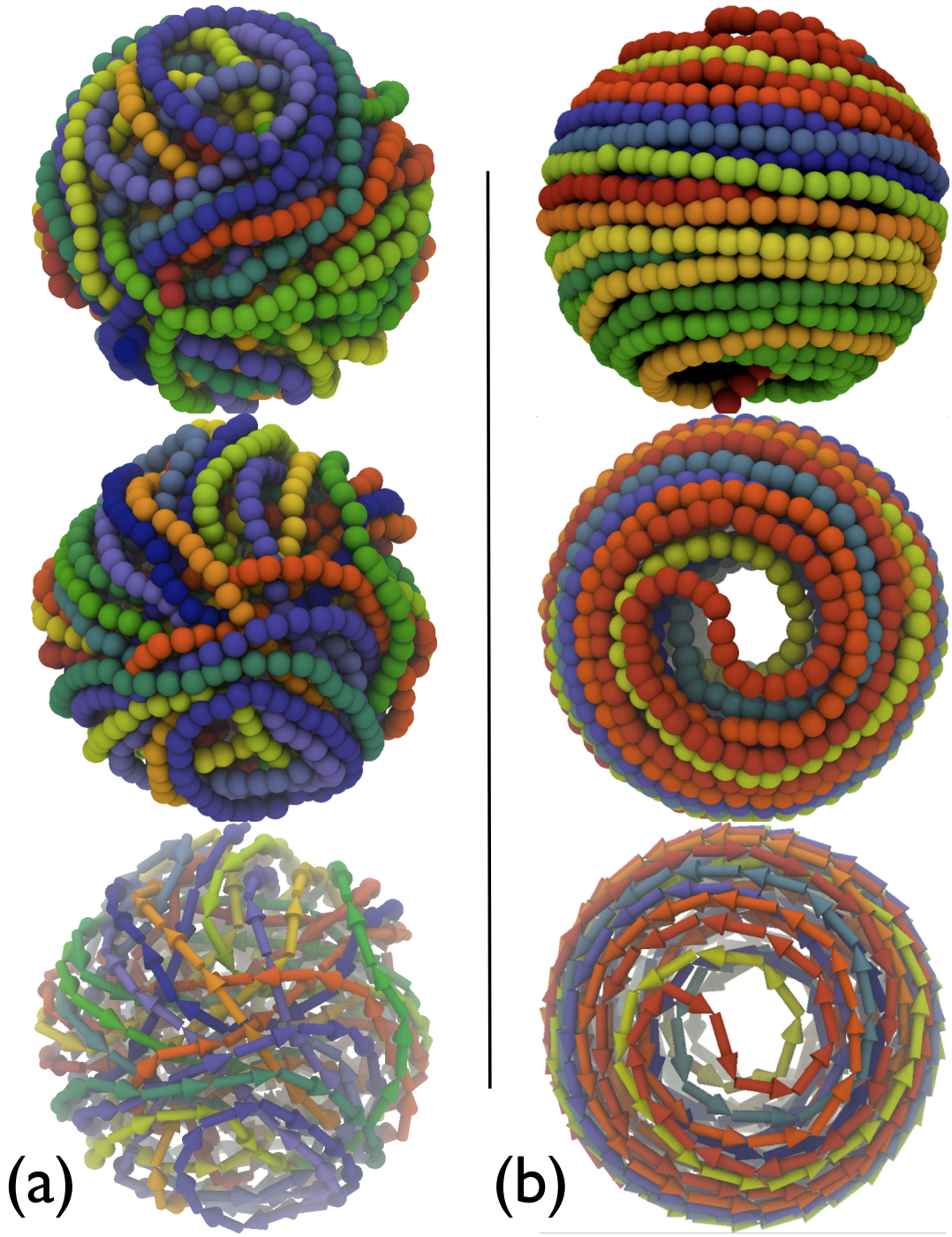

Figure 6.2: Model conformations of the fully-packaged 10kb-long P4 genome in the (a) absence and (b) presence of the cholesteric potential (of strength $k_c = 1\,K_B T$ range Δ=3nm and biasing angle $\alpha_0 = 1°$). In each of the two panels, the first two images present front and top views of DNA arrangement. In both cases a rainbow coloring scheme (red → yellow → green → blue) is used to follow the indexing of the chain beads (the red end is the one rooted at the portal motor location). The progression of the DNA chain, and its winding directionality is also highlighted in the bottom images where an oriented arrow is used to represent each triplet of beads.

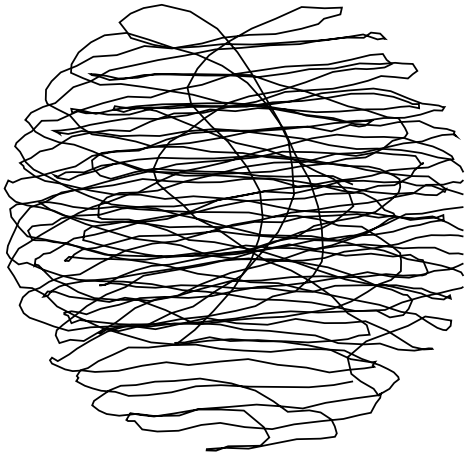

Figure 6.3: Projection view of the fully-packaged model P4 genome configuration shown in Fig. 6.2 (b). The configuration is represented with its projected centerline so to highlight the arrangement of the chain in the capsid interior, in a fashion analogous to cryo-EM images (where signal comes from all packed layers at the same time).

to form a coaxial spool, with loops having maximum (equatorial) diameter. As more DNA is fed inside, the spool proceeds maintaining the initial winding directionality (which can change from run to run) and moving away from the equatorial region towards the poles. In doing so it attains tighter radii of curvature and the accompanying increase in bending energy makes it possible for the chain to change winding directionality near the poles producing hairpin defects, like the one shown in Fig. 6.2 (b).

6.2.2 Knot spectrum

We now turn our attention to the second and key issue, namely the bias in the knot spectrum of circularized DNA molecules. Characterizing the knot spectrum requires the collection of hundreds of configurations where DNA is fully loaded inside the capsid. The duration of each of the packaging simulations depends very strongly on the final filling fraction of the capsid. In fact, the effective rate of DNA loading shows a noticeable reduction upon increasing the fraction of packed genome. For reasons of computational efficiency, we therefore took as term of reference not the knotting experiments on the full P4 genome, but those on the half-P4 genome recently carried by Trigueros and Roca [135].

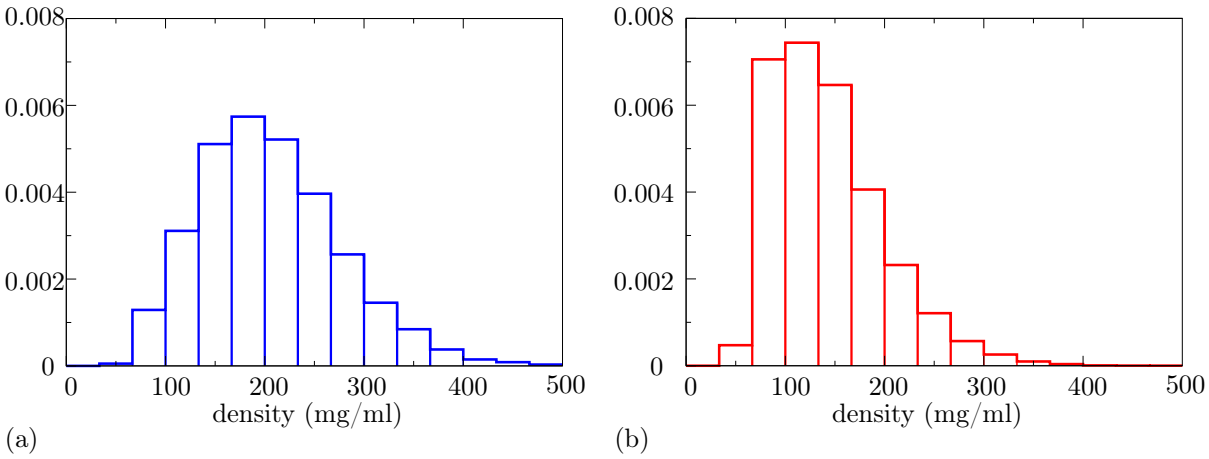

Figure 6.4: (a) Distribution of the local density of DNA for fully-packaged configurations of the entire P4 genome in the absence of the cholesteric potential. (b) Distribution of the local density of DNA for fully-packaged configurations of the half P4 genome in the absence of the cholesteric potential. In both cases a non negligibile part of the chain is packed at densities inside the cholesteric range $160 - 380$ mg/ml. This result indicates the necessity of considering a cholesteric interaction between DNA strands. With reference to locally hexagonal arrangements of dsDNA strands, the $160 - 380$ mg/ml density range corresponds to DNA interaxial distances going respectively from 4.9nm to 3.2nm.

In this study, the knotting of the 4.7kb-long DNA still occurred inside the P4 capsid and produced a spectrum that, except for a decrease in the average level of knot complexity, maintained the same biases of the full-genome case among the simplest types of knots. As shown in Fig. 6.4, the shorter genome is still expected to attain local packing densities in the cholesteric range and therefore provides an ideal, computationally viable (requiring only 640 beads), testbed for the proposed model.

We generated several hundred configurations for various values of the cholesteric potential strength k_c (from 0.25 $K_B T$ to $3.0 K_B T$), for different values of the interaction range Δ (from $\sim$ 3 to 5 nm), and of the preferred twist angle α_0 (from $0°$ to $10°$). These values cover the range of available estimates for k_c, Δ and α_0 [128, 21, 134]. In general, increasing the strength of the cholesteric interaction simplifies the average topological complexity of the generated (closed) configurations. In spite of this, the relative probability of occurrence of the simplest types of knots is found to be only mildly affected by the specific parametrization of the cholesteric potential and was therefore taken as a meaningful term of comparison against available experimental data. As, a part for a difference in the average knot complexity, the key features of the half and full

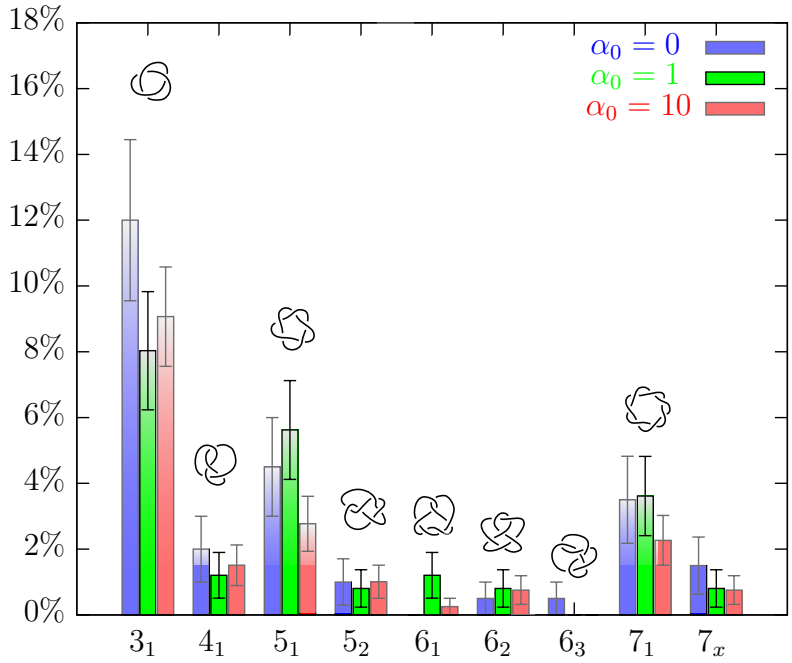

Figure 6.5: Knot spectrum: probability of occurrence of the simplest types of prime knots in 4.7Kb-long DNA inside the P4 capsid obtained accounting for the cholesteric interaction. Blue, green and red bars correspond to probabilities obtained for $\alpha_0 = 0°$, $\alpha_0 = 1°$ and $\alpha_0 = 10°$ respectively. The total knot population sizes in the three cases are 200, 250 and 300. Error bars are calculated using poissonian statistics. Chiral and torus knots prevail in all three cases, as evident from the predominance of 3_1, 5_1, 6_1 and 7_1 knots. Spectra obtained for $\alpha_0 = 0°$ and $\alpha_0 = 1°$ are compatible within errors. The index 7_x is used for the cumulative set of 7_2, 7_3, 7_4 and 7_5 knots.

genome knot spectrum are consistent with each other, we take as reference the 10kb case, for which finer experimental data are available [8]. As shown later, the best quantitative agreement between the experimental and computed relative knot probabilities is found for $k_c = 1\, K_B\, T$, $\Delta = 5$nm and $\alpha_0 = 1°$. Unless otherwise stated, the results presented hereafter pertain to this choice of parameters.

The packaging dynamics was used to generate 250 configurations which, on average, appear to be highly knotted (with $\sim$ 70% of them being non-trivial knots). After all possible geometrical simplifications, about 20% of the configurations remained too complex to be correctly identified against a lookup table of knots having crossing number smaller than 17.In particular, the average number of crossings after simplification is 12 (with about 25% of the knots with more than 14 crossings), consistently with experimental

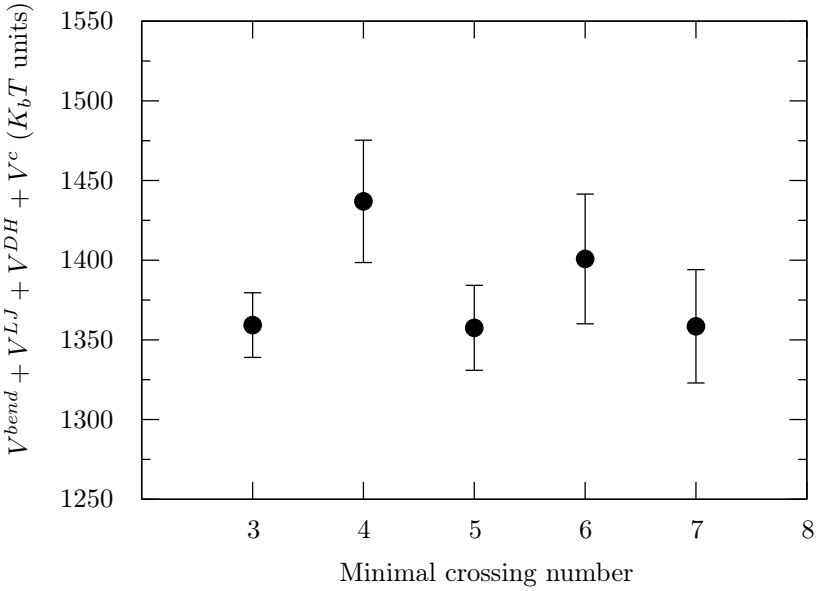

Figure 6.6: Average internal energy (with omission of the contribution from the chain connectivity, FENE, potential) as a function of the topological complexity of the configurations of the fully-loaded P4 half-genome. The topological complexity is conveyed by the minimal number of crossings after geometrical simplification of the closed configurations. On average, knots with 3, 5 and 7 crossings (which are dominated by torus knots) appear energetically favoured over non-torus knot types with comparable complexity.

findings on the half genome P4 [135]. Among the simplest types of knots, those with up to 7 crossings, the most populated ones are torus knots. The probabilities of the simplest knots for three different choices of the preferential twist angle α_0, $\alpha_0 = 0°, 1°$ and $10°$ (with $\Delta = 5$nm and k_c=$1K_bT$) are reported in the histogram of Fig. 6.5. From it we can see that in all three cases the achiral knot 4_1 is severely suppressed when compared to both the simpler torus knot 3_1 and the more complex torus knot 5_1. The latter is, furthermore, in excess of its 5_2 counterpart, reversing the trend observed in models of confined self-avoiding flexible polymers [8, 87]. Overall, at least 20% of the conformations correspond to the torus knots 3_1, 5_1, 7_1, 8_{19}, 9_1 and 10_{124} which, in fact, appear to possess an average lower energy than knots type of comparable complexity, as shown in Fig. 6.6.

For the purpose of a comparison with the experimental data of ref. [8] we recall that the experimental relative population of 3_1, 4_1, 5_1 and 5_2 knots were 57%, 3.8%, 39%

and $< 1\%$, respectively. Within estimated uncertainties, the knots populations obtained for $\alpha_0 = 1^\circ$ (in green in Fig. 6.5) are in good agreement with the above data as their relative probability profile is the following: 51% for 3_1, 8% for 4_1, 36% for 5_1 and 5% for 5_2. The comparison indicates a level of accord with experiments which was not achieved in previous studies where both equilibrium and dynamical processes were used to sample compact configurations of DNA models of varying complexity [8, 7, 86, 87].

Our results therefore suggest that the knot spectrum can be used to discriminate the viability of several force fields for DNA interactions in confined geometries. Indeed, as expected, simulations with $k_c = 0$, when compared with the experimental data, lack the characteristic bias towards torus knots and provide too complex a knot spectrum. We also performed simulations with self-attractive force fields (coming e.g. from multivalent counterions in the buffer) which led to better spooling but, once more, produced a knot spectrum qualitatively different from the experimental one.

It is worth pointing out that the bias in favor of torus knots is not accompanied by a detectable bias on the geometrical writhe which has an average value compatible with 0 (see table 6.1). A related observation is that no statistically-significant difference is observed between the types of handedness of the occurring torus knots. These two aspects reflect the small bias angle $\alpha_0 = 1^\circ$ of the cholesteric interaction which, on the lengthscale given by the capsid size, essentially promotes a nematic, collinear ordering of contacting packaged strands. In fact, as shown in Fig. 6.5, the knot spectra obtained for $\alpha_0 = 1^\circ$ or $\alpha_0 = 0^\circ$ (nematic ordering) are compatible withing the given uncertainties. Furthermore, in spite of the apolar character of the interaction, it is found that most pairs of contacting strands are co-directional (assume that orientation is given by chain indexing) so that pronounced differences in the handedness of torus knots are observed upon using larger absolute values of α_0. For example $\alpha_0 = 10^\circ$ produces an appreciable majority of right-handed torus knots, as reported in table 6.1. The results suggest that future experiments where the handedness of torus knots in circularised P4 DNA is probed in dependence of the concentration of polycations (which can modulate the biasing angle) would be valuable to confirm the present findings.

6.2.3 DNA ejection

The spatial organization of the DNA in the capsid reproduced by our model can also explain the apparent contradiction between the occurrence of highly knotted DNA

Table 6.1: Knot handedness for different values of α_0.[(a)]

α_0	left-handed	right-handed
0	0.56 ± 0.10	0.44 ± 0.09
1	0.49 ± 0.04	0.51 ± 0.04
10	0.24 ± 0.06	0.76 ± 0.11

[(a)] Fraction of left-handed and right-handed knots among the set of torus knots. Analyzed configurations included knots of up to 16 crossings after simplification that were either prime torus knots or prime components of composite knots where all factors were torus knots. Errors denote the uncertainty obtained using the binomial statistics. A highly significant bias is observed only for $\alpha_0 = +10°$.

configurations inside the mutant phage capsids and the necessity of a highly efficient delivery, by ejection, of the wild-type genome into the cytoplasm of the infected cell [40, 57, 108, 124, 39]. In this respect it is important to recall that, though most of the experiments on the knotting of the P4 DNA have been carried out for the P4 tailless mutant, a non-negligible fraction of knots (47%) was found also for the wild-type mature P4 phage. In this case only one of the DNA ends is inside the capsid, while the other is anchored to the phage tail. At variance with the mutant case, the annealing of the two cohesive ends occurs *outside* the phage *after* the destruction of the capsid. Considering that a partial DNA relaxation occurs between the extraction of the DNA and its circularization (which "traps" its knotted state), the fact that a substantial fraction of knotted DNA is still found under these conditions is therefore indicative of two facts. First, DNA is highly entangled inside the wild-type virus. As these viruses are infective, the second conclusion is that the entanglement does not hinder the ejection of DNA into the host cell.

Our study provides valuable insight into both these aspects. Consistent with the first observation, we have verified that both in the wild-type case where one end of the DNA is kept anchored at the portal motor location or the mutant case when both ends are free to reptate and anneal inside the capsid, the majority of the configurations are found to be knotted upon an outward closure.

The implications of our results for the ejection process are best discussed in relation to the geometrical properties of the occurring knots. Analyzing the knot lengths with both the bottom-up and top-down knot location schemes (see § 2.3) we found that knot are highly delocalized according to both schemes. For example, for the most abundant

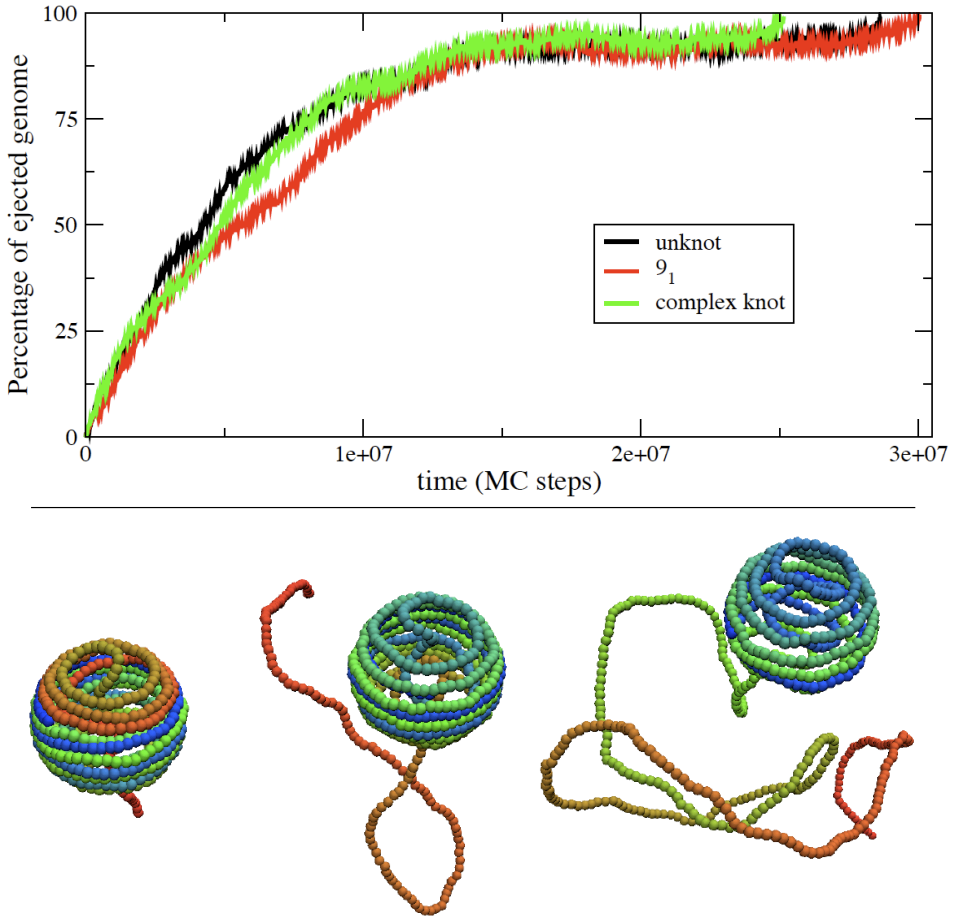

Figure 6.7: Percentage of ejected genome as a function of time (in simulation steps, each step corresponds to about 1-5 ns), for three different starting configurations of the fully-loaded half-P4 genome. The initial configurations correspond to an unknot (black curve), a 9_1 knot (red curve) and a knot which was too complex to be identified against a lookup table of prime knots of up to 16 crossings (green curve). The ejection proceeds in a fashion that is largely independent of the initial knotted state. A slowing down of the ejection is seen after 70% of the genome has ejected. The ejection speed up for the very last portion of the genome is ascribable to the entropic pulling of the expelled chain (this regime is expected to be sensitive to various details such as the presence of phage tail). For snapshots of the ejection process for the 9_1 initial knot, see bottom panel.

simple knot types, 3_1 and 5_1, the knotted portion of the chain [75] is on average $\sim 50\%$. This indicates a very high degree of delocalization, as 3_1 and 5_1 knots can be tied very tightly with as little as $\sim 5\%$ of the chain, as well as an "ordering" effect of the cholesteric potential, highlighted by small incidence of multiscalar behaviour of the knot length, in contrast to what observed in § 5.2.3. Based on this quantitative observations we formulate the proposal that the delocalization of the knots is a key factor for avoiding ejection slow-down which can occur in the presence of tight knots [81]. A recent study on the pore translocation of knotted DNA has further indicated that, besides knot tightness, a further important player is the force which draws the knotted DNA out of the cavity from a narrow pore. In fact, tight knots can slow down the pore-translocation process but not necessarily halt it, unless the driving force is sufficiently high [114].

In principle, knot delocalization and the absence of complex multiscalar behaviour of the knot length may not be sufficient to ensure an effective delivery of the genome, as even delocalized knots may be badly entangled geometrically and slow down ejection. We have verified that this is not the case for the knotted configurations generated with our model. To establish this point we have performed a series of simulations where the fully-loaded chains with different topological state (upon closure) were left free to diffuse out of the capsid by taking advantage of thermodynamic forces which disfavor the confined packaged state [96]. The ejection kinetics was found to be largely independent of the initial topological state and all the configurations are ejected without any significant geometrical or topological hindrance, see Fig. 6.7.

6.3 Summary

We have presented a theoretical study of several aspects of DNA packaging in viral capsids for which experimental measurements are available and that were unaccounted for by previous theoretical and computational investigations of the problem. The typical mesoscopic description of DNA employed by such studies was that of a self-avoiding semiflexible chain. This treatment is highly successful in reproducing the observed features of unconstrained DNA [120]. Our findings show that the known rich phenomenology of densely-packed DNA inside phages can be satisfactorily reproduced by accounting for the known preference of contacting DNA portions to meet with a preferred twist angle, without the necessity to postulate biases resulting from out of equilibrium effects.

Our approach allow us to reproduce the salient features of the spectrum of knots observed experimentally for P4 DNA and are also consistent with the cryo-EM data which show regular organization close to the surface of the capsid. This is at odds with most previous simulation data on bacteriophage DNA which show much more disordered packing if, as we do here, a buffer with monovalent counterions is considered.

Concluding remarks

In this thesis we presented a numerical investigation of the interplay between physical, geometrical and topological properties of polymer rings in several cases of relevance for biophysics. Since many biopolymers, and particularly DNA, are often confined within regions having calliper size smaller their contour length, or are found in dense solutions, we dedicated most of this Thesis to the investigation of the interplay between topological and geometrical/physical properties in dense systems of polymer rings, focusing in particular on the localization properties of the knots (their tightness) in relation with the geometrical entanglement of the chains.

In order to study the degree of localization of knots in highly entangled polymer rings, in chapter 2 we introduced a novel closure scheme, termed the *minimally-interfering* closure, to assign a topological state to open subportions of a ring. We proved that the *minimally-interfering* closure is computationally fast, yet robust and accurate compared to other schemes, particularly when applied to compact polymers. Furthermore we showed that the degree of localization of a knot depends in general on the searching algorithm adopted to locate the knot on the chain. Search algorithms usually adopted in literature can be divided into two broad categories: bottom-up schemes, and top-down schemes. The former start from a small unknotted subportion of the ring and subsequently look for the knot in subportions of increasing length. The latter on the other hand start by considering large knotted subportions of the ring and try to reduce their size until the knot is untied, keeping the previous to last (knotted) arc. we showed that while this two kinds of knot location algorithms produce consistent results on simple, unconstrained polymer rings, their result diverge with increasing ring compactness and ring length. We observed that this divergence can explain the different results reported in literature for the scaling behaviour of the knot length with increasing length of polymer rings.

We devoted chapter 3 to the study of the mutual entanglement between the prime components of a composite knot. For asymptotically large chain lengths, prime components are expected to behave like point-like decorations and be completely independent from

one another. We showed that this is not the case for the most probable composite knots extracted from an equilibrium population of rings where, on the contrary, we observed a significant degree of entanglement between different prime components . We found that prime components are often nested one inside the other and the properties of those prime knots which are found as separate along the chain depend on the number of knots tied on it. We further showed that the properties of this mutual entanglement can be qualitatively reproduced using a transparent one-dimensional model in which knots are substituted with paraknots.

Starting from chapter 4 we tackled the interplay between topological properties and physical confinement. In chapter 4 we investigated the equilibrium and kinetic properties of solutions of model ring polymers, by varying both solution density and ring topology. We observed that while the equilibrium metric properties of unknot and trefoil knotted rings are only weakly affected by the increase of solution density, kinetics properties are strongly affected by the degree of inter-chain entanglement, with characteristic times of ring size relaxation, reorientation and diffusion changing by one order of magnitude across the considered range of concentrations. Yet, significant topology-dependent differences in kinetics were observed only for very dilute solutions. For knotted rings, the slowest kinetic process was found to correspond to the diffusion of the knotted region along the ring backbone.

In chapter 5 we studied the interplay of geometrical and topological entanglement in semiflexible knotted polymer rings under spherical confinement. In particular we characterized how the top-down and bottom-up knot lengths depend on the ring contour length, L_c and the radius of the confining sphere, R_c. We observed that the entanglement acquires a multiscale character upon increasing confinement and showed how the complex interplay of both top-down and bottom-up knot lengths with L_c and R_c can be encompassed by a simple scaling argument based on deflection theory.

Finally, we used topological analysis to infer the physical properties of dsDNA packaged in bacteriophage capsids. Cryo-em studies showed that DNA in bacteriophages epsilon-15 and phi-29 is neatly ordered in concentric shells close to the capsid wall, while an increasing level of disorder was measured when moving away from the capsid internal surface. On the other hand the detected spectrum of knots formed by DNA that is circularised inside the P4 viral capsid showed that DNA tends to be knotted with high probability, with a knot spectrum characterized by complex knots and biased towards torus knots and against achiral ones. In chapter 6 we showed, that both the shell ordering

and the knot spectrum can be reproduced quantitatively if one accounts for the preference of contacting DNA strands to juxtapose at a small twist angle, as in cholesteric liquid crystals.

Acknowledgements

I am deeply indebted to my advisor, Prof. Cristian Micheletti, for patiently mentoring me during my doctorate. During my PhD I realized that Cristian teaches to his students much more than biophysics. He teaches how to set objectives, how to plan and organize research and how to communicate it effectively. Much more importantly, through his example, Cristian teaches to do research with honesty and dedication, always showing a great sense of responsibility towards his students and collaborators, and towards other researchers. Thanks to this, I can now say that my PhD has been a truly enriching and formative experience, both professionally and personally.

During my doctorate I had the luck and pleasure to collaborate with D. Marenduzzo, E. Orlandini and A. Rosa. Several results presented in this thesis are the fruit of these enriching collaborations. I further wish to thank D. Marenduzzo for encouraging me to apply to SISSA when I was a master student.

The computational work presented in this thesis would have been much harder without the presence of Marco Giunta and the other computer technicians of SISSA, who do an impressive job in maintaining our workstations and mainframes.

I wish to thank E. Paoli for her help in double-checking the manuscript for grammatical errors and, together with F. Rizzato, P. Vasko and K. Kustrin, for many meals, teas, coffees and in general for support during these past months I spent writing the manuscript.

This manuscript is not only the result of hard scientific work. Behind this work, sustaining it, there are all those human interactions I had the luck to enjoy during my PhD. Many people, through their friendship and love helped me arriving at this point. I can not possibly write a complete list of them, but I wish to remember here at least some. First of all, I am grateful to my parents who always sustained my studies and choices. Then I wish to thanks my flatmates in these past two years: Elisa, Petr, Francesca, Maya, Luca and Pierpaolo for creating and keeping alive that warm environment which I ended up calling home. I know I will miss it. I am very grateful to Katerina for her friendship, her smile and her wisdom. I am grateful to my friends from Ponte and

Susegana, especially Daniele, Alberto, Eleonora, Chiara, Marco, Elena, Davide and Matteo, for I know I can count on them wherever I am, even after all these years I have spent wandering around the world. To Daniele Zarantonello, Alberto Degan, Marta Bettin and Cristina Cella for listening to me when I was troubled. To Meta and Peter for their friendship and for introducing me to Trieste and the Carsic plateau. To the family of Ayllu Situwa, and all my Peruvian friends, for always making me think about what is important.

Last but not least, I am grateful to all the people of the Statistical and Biological Physics group of SISSA, with whom I had the luck to work during my PhD, and in particular to my officemates Raffaello and Marco, who had the patience to share an office with me, and to Daniele Granata, whom I once convinced to be a student representative. Nonetheless he never tried to kill me for that (not that I know at least). To all of you: I could not hope to find a better working environment, thanks for these years.

Bibliography

[1] C. C. Adams. *The Knot Book*. Freeman, 1994.

[2] J.W. Alexander. Topological invariants of knots and links. *Trans. Amer. Math. Soc*, 30(2):275–306, 1928.

[3] K. Alim and E. Frey. Shapes of semiflexible polymer rings. *Phys. Rev. Lett.*, 99:198102, 2007.

[4] Sotero Alvarado, Jorge Calvo, and Kenneth Millett. The generation of random equilateral polygons. *Journal of Statistical Physics*, 143:102–138, 2011. 10.1007/s10955-011-0164-4.

[5] Y. Arai, R. Yasuda, K. Akashi, Y. Harada, H. Miyata, T. Kinosita, and H. Itoh. Tying a molecular knot with optical tweezers. *Nature*, 399:446–448, Jun 1999.

[6] J. Arsuaga and Y. Diao. Dna knotting in spooling like conformations in bacteriophages. *Computational and Mathematical Methods in Medicine*, 9(3-4):303–316, 2008.

[7] J. Arsuaga, R.K.Z. Tan, M. Vazquez, D.W. Sumners, and S.C. Harvey. Investigation of viral dna packaging using molecular mechanics models. *Biophysical chemistry*, 101:475–484, 2002.

[8] J. Arsuaga, M. Vazquez, P. McGuirk, S. Trigueros, D.W. Sumners, J. Roca, et al. DNA knots reveal a chiral organization of DNA in phage capsids. *Proceedings of the National Academy of Sciences of the United States of America*, 102(26):9165, 2005.

[9] J. Arsuaga, M. Vázquez, S. Trigueros, D.W. Sumners, J. Roca, et al. Knotting probability of DNA molecules confined in restricted volumes: DNA knotting in phage capsids. *Proceedings of the National Academy of Sciences of the United States of America*, 99(8):5373, 2002.

[10] R. Auhl, R. Everaers, G. S. Grest, K. Kremer, and S. J. Plimpton. Equilibration of long chain polymer melts in computer simulations. *J. Chem. Phys.*, 119:12718, 2003.

[11] M. Baiesi, E. Orlandini, and A. L. Stella. The entropic cost to tie a knot. *Journal of Statistical Mechanics: Theory and Experiment*, 2010(06):P06012, 2010.

[12] M. Baiesi, E. Orlandini, A. L. Stella, and F. Zonta. Topological signatures of globular polymers. *Phys. Rev. Lett.*, 106:258301, 2011.

[13] X.R. Bao, H.J. Lee, and S.R. Quake. Behavior of complex knots in single dna molecules. *Physical review letters*, 91(26):265506, 2003.

[14] A.D. Bates and A. Maxwell. *DNA Topology*. Oxford Bioscience, 2005.

[15] E. Ben-Naim, Z. A. Daya, P. Vorobieff, and R. E. Ecke. Knots and random walks in vibrated granular chains. *Phys. Rev. Lett.*, 86:1414–1417, Feb 2001.

[16] M. Bishop and J. P. J. Michels. Scaling in three-dimensional linear and ring polymers. *J. Chem. Phys.*, 84:444, 1986.

[17] Y. Bouligand and F. Livolant. The organization of cholesteric spherulites. *Journal de Physique*, 45(12):1899–1923, 1984.

[18] C. Bustamante, J. F. Marko, E. D. Siggia, and S. Smith. Entropic elasticity of lambda-phage dna. *Science*, 265(5178):1599–1600, Sep 1994.

[19] M. Castelnovo and A. Evilevitch. Dna ejection from bacteriophage: towards a general behavior for osmotic-suppression experiments. *Eur. Phys. J. E Soft Matter*, 24(1):9–18, Sep 2007.

[20] M.E. Cates and J.M. Deutsch. Conjectures on the statistics of ring polymers. *Journal de physique*, 47(12):2121–2128, 1986.

[21] A. G. Cherstvy. Dna cholesteric phases: the role of dna molecular chirality and dna-dna electrostatic interactions. *J. Phys. Chem. B*, 112(40):12585–12595, Oct 2008.

[22] Luis R. Comolli, Andrew J. Spakowitz, Cristina E. Siegerist, Paul J. Jardine, Shelley Grimes, Dwight L. Anderson, Carlos Bustamante, and Kenneth H. Downing. Three-dimensional architecture of the bacteriophage phi29 packaged genome and elucidation of its packaging process. *Virology*, 371(2):267–277, Feb 2008.

[23] R. Corless, G. Gonnet, D. Hare, D. Jeffrey, and D. Knuth. On the lambert w function. *Advances in Computational Mathematics*, 5:329–359, 1996. 10.1007/BF02124750.

[24] Peter Cromwell. *Knots and Links*. Cambridge University Press, 2004.

[25] P.-G. de Gennes. *Scaling Concepts in Polymer Physics*. Cornell University Press, Ithaca, 1979.

[26] M Delbrück. Dnotting problems in biology. In R E Bellman, editor, *Mathematical problems in biological sciences*, volume 14 of *Proc. Symp. Appl. Math*, page 55, 1962.

[27] J. des Cloizeaux. Ring polymers in solution: topological effects. *J. Phys. Lett.*, 42:L433, 1981.

[28] M. Doi and S. F. Edwards. *The theory of Polymer Dynamics*. Clarendon Press, 1986.

[29] T. Dokland, B. H. Lindqvist, and S. D. Fuller. Image reconstruction from cryo-electron micrographs reveals the morphopoietic mechanism in the p2-p4 bacteriophage system. *EMBO J*, 11(3):839–846, Mar 1992.

[30] R. Dulbecco and M. Vogt. Evidence for a ring structure of polyoma virus DNA. *Proceedings of the National Academy of Sciences of the United States of America*, 50(2):236–243, 1963.

[31] W. C. Earnshaw and S. C. Harrison. Dna arrangement in isometric phage heads. *Nature*, 268(5621):598–602, Aug 1977.

[32] F. Eisenhaber, P. Lijnzaad, P. Argos, C. Sander, and M. Scharf. The double cube lattice method: Efficient approaches to numerical integration of surface area and volume and to dot surface contouring of molecular assemblies. *J. Comp. Chem.*, 16:273, 1995.

[33] Erika Ercolini, Francesco Valle, Jozef Adamcik, Guillaume Witz, Ralf Metzler, Paolo De Los Rios, Joaquim Roca, and Giovanni Dietler. Fractal dimension and localization of dna knots. *Phys. Rev. Lett.*, 98:058102, Jan 2007.

[34] R. Everaers, S. K. Sukumaran, G. S. Grest, C. Svaneborg, A. Sivasubramanian, and K. Kremer. Rheology and microscopic topology of entangled polymeric liquids. *Science*, 303:823, 2004.

[35] Alex Evilevitch, Laurence Lavelle, Charles M. Knobler, Eric Raspaud, and William M. Gelbart. Osmotic pressure inhibition of DNA ejection from phage. *Proceedings of the National Academy of Sciences of the United States of America*, 100(16):9292–9295, Aug 2003.

[36] O. Farago, Y. Kantor, and M. Kardar. Pulling knotted polymers. *Europhys. Lett.*, 60:53–59, 2002.

[37] Christopher Forrey and M. Muthukumar. Langevin dynamics simulations of genome packing in bacteriophage. *Biophys J*, 91(1):25–41, Jul 2006.

[38] E. Frisch, H.L .and Wasserman. Chemical topology 1. *Journal of the American Chemical Society*, 83(18):3789–3795, 1961.

[39] I. S. Gabashvili and A.Y. Grosberg. Dynamics of double stranded dna reptation from bacteriophage. *J Biomol Struct Dyn*, 9(5):911–920, Apr 1992.

[40] William M. Gelbart and Charles M. Knobler. Virology. pressurized viruses. *Science*, 323(5922):1682–1683, Mar 2009.

[41] O. Gonzalez, A. B. A. Graf, and J. H. Maddocks. Dynamics of a rigid body in a stokes fluid. *J. Fluid Mech.*, 519:133, 2004.

[42] A. Grosberg, Y. Rabin, S. Havlin, and A. Neer. Crumpled globule model of the three-dimensional structure of dna. *Europhys. Lett.*, 23:373, 1993.

[43] E. Guitter and E. Orlandini. Monte carlo results for projected self-avoiding polygons: a two-dimensional model for knotted polymers. *Journal of Physics A: Mathematical and General*, 32(8):1359, 1999.

[44] J. D. Halverson, W. B. Lee, G. S. Grest, A. Y. Grosberg, and K. Kremer. Molecular dynamics simulation study of nonconcatenated ring polymers in a melt: I. statics. *J. Chem. Phys.*, 134:204904, 2011.

[45] J. D. Halverson, W. B. Lee, G. S. Grest, A. Y. Grosberg, and K. Kremer. Molecular dynamics simulation study of nonconcatenated ring polymers in a melt: Ii. dynamics. *J. Chem. Phys.*, 134:204905, 2011.

[46] B. Hess, C. Kutzner, D. van der Spoel, and E. Lindahl. Gromacs 4: Algorithms for highly efficient, load-balanced, and scalable molecular simulation. *J. Chem. Theory Comput.*, 4:435, 2008.

[47] J Hoste and M Thistlethwaite. knotscape. http://www.math.utk.edu/ morwen/knotscape.html

[48] Lei Huang and Dmitrii E. Makarov. Langevin dynamics simulations of the diffusion of molecular knots in tensioned polymer chains†. *The Journal of Physical Chemistry A*, 111(41):10338–10344, 2007. PMID: 17637045.

[49] K. Hur, C. Jeong, R. G. Winkler, N. Lacevic, R. H. Gee, and D. Y. Yoon. Chain dynamics of ring and linear polyethylene melts from molecular dynamics simulations. *Macromolecules*, 44:2311, 2011.

[50] K. Hur, R. G. Winkler, and D. Y. Yoon. Comparison of ring and linear polyethylene from molecular dynamics simulations. *Macromolecules*, 39:3975, 2006.

[51] Mandar M. Inamdar, William M. Gelbart, and Rob Phillips. Dynamics of dna ejection from bacteriophage. *Biophys J*, 91(2):411–420, Jul 2006.

[52] W. Jiang, J. Chang, J. Jakana, P. Weigele, J. King, and W. Chiu. Structure of epsilon15 bacteriophage reveals genome organization and dna packaging/injection apparatus. *Nature*, 439(7076):612–616, 2006.

[53] M. Kapnistos, M. Lang, D. Vlassopoulos, W. Pyckhout-Hintzen, D. Richter, D. Cho, T. Chang, and M. Rubinstein. Unexpected power-law stress relaxation of entangled ring polymers. *Nature Materials*, 7:997, 2008.

[54] V. Katritch, J. Bednar, D. Michoud, R.G. Scharein, J. Dubochet, and A. Stasiak. Geometry and physics of knots. *Nature*, 384:142 – 145, 1996.

[55] Vsevolod Katritch, Wilma K. Olson, Piotr Pieranski, Dubochetm Jacques, and Andrzej Stasiak. Properties of ideal composite knots. *Nature*, 388:148–151, 1997.

[56] Vsevolod Katritch, Wilma K. Olson, Alexander Vologodskii, Jacques Dubochet, and Andrzej Stasiak. Tightness of random knotting. *Phys. Rev. E*, 61:5545–5549, May 2000.

[57] J. Kindt, S. Tzlil, A. Ben-Shaul, and W. M. Gelbart. DNA packaging and ejection forces in bacteriophage. *Proceedings of the National Academy of Sciences of the United States of America*, 98(24):13671–13674, Nov 2001.

[58] Neil P. King, Eric O. Yeates, and Todd O. Yeates. Identification of rare slipknots in proteins and their implications for stability and folding. *Journal of Molecular Biology*, 373(1):153 – 166, 2007.

[59] KV Klenin, AV Vologodskii, VV Anshelevich, AM Dykhne, and MD Frank-Kamenetskii. Effect of excluded volume on topological properties of circular dna. *Journal of biomolecular structure & dynamics*, 5(6):1173, 1988.

[60] Kleanthes Koniaris and M. Muthukumar. Knottedness in ring polymers. *Phys. Rev. Lett.*, 66:2211–2214, Apr 1991.

[61] A.A. Kornyshev, S. Leikin, and S.V. Malinin. Chiral electrostatic interaction and cholesteric liquid crystals of dna. *The European Physical Journal E: Soft Matter and Biological Physics*, 7(1):83–93, 2002.

[62] K. Kremer and G. S. Grest. Dynamics of entangled linear polymer melts: A molecular-dynamics simulation. *J. Chem. Phys.*, 92:5057, 1990.

[63] F. Lahmar, C. Tzoumanekas, D. N. Theodorou, and B. Rousseau. Onset of entanglements revisited. dynamical analysis. *Macromolecules*, 42:7485, 2009.

[64] P.-Y. Lai. Dynamics of polymer knots at equilibrium. *Phys. Rev. E*, 66:021805, 2002.

[65] A. Leforestier, S. Brasilès, M. de Frutos, E. Raspaud, L. Letellier, P. Tavares, and F. Livolant. Bacteriophage t5 dna ejection under pressure. *J Mol Biol*, 384(3):730–739, Dec 2008.

[66] Amélie Leforestier and Françoise Livolant. Structure of toroidal DNA collapsed inside the phage capsid. *Proceedings of the National Academy of Sciences of the United States of America*, 106(23):9157–9162, Jun 2009.

[67] L. F. Liu, J. L. Davis, and R. Calendar. Novel topologically knotted dna from bacteriophage p4 capsids: studies with dna topoisomerases. *Nucleic Acids Res*, 9(16):3979–3989, Aug 1981.

[68] L. F. Liu, L. Perkocha, R. Calendar, and J. C. Wang. Knotted DNA from bacteriophage capsids. *Proceedings of the National Academy of Sciences of the United States of America*, 78(9):5498–5502, Sep 1981.

[69] L.F. Liu, R.E. Depew, and J.C. Wang. Knotted single-stranded dna rings: A novel topological isomer of circular single-stranded dna formed by treatment with escherichia coli ω protein. *Journal of molecular biology*, 106(2):439–452, 1976.

[70] C. Livingston. *Knot theory.* The Carus Mathematical Monographs, Nr 24, Mathematical Association of America, Whashington DC, 1993.

[71] F. Livolant and A. Leforestier. Condensed phases of dna: structures and phase transitions. *Progress in polymer science*, 21(6):1115–1164, 1996.

[72] David Löf, Karin Schillén, Bengt Jönsson, and Alex Evilevitch. Forces controlling the rate of dna ejection from phage lambda. *J Mol Biol*, 368(1):55–65, Apr 2007.

[73] M. L. Mansfield and J. F. Douglas. Properties of knotted ring polymers. i. equilibrium dimensions. *J. Chem. Phys.*, 133:044903, 2010.

[74] M.L. Mansfield. Knots in hamilton cycles. *Macromolecules*, 27(20):5924–5926, 1994.

[75] B. Marcone, E. Orlandini, A. L. Stella, and F. Zonta. What is the length of a knot in a polymer? *J. Phys. A: Math. Gen.*, 38:L15, 2005.

[76] B. Marcone, E. Orlandini, A.L. Stella, and F. Zonta. Size of knots in ring polymers. *Physical Review E*, 75(4):041105, 2007.

[77] D. Marenduzzo and C. Micheletti. Thermodynamics of dna packaging inside a viral capsid: the role of dna intrinsic thickness. *J Mol Biol*, 330(3):485–492, Jul 2003.

[78] D. Marenduzzo, C. Micheletti, and E. Orlandini. Biopolymer organization upon confinement. *Journal of Physics: Condensed Matter*, 22(28):283102, 2010.

[79] D. Marenduzzo and E. Orlandini. Dynamics of fibers growing inside soft vesicles. *EPL (Europhysics Letters)*, 80(4):48004, 2007.

[80] D. Marenduzzo, E. Orlandini, A. Stasiak, D.W. Sumners, L. Tubiana, and C. Micheletti. DNA-DNA interactions in bacteriophage capsids are responsible for the observed dna knotting. *Proceedings of the National Academy of Sciences of the United States of America*, 106(52):22269–22274, 2009.

[81] Richard Matthews, A. A. Louis, and J. M. Yeomans. Knot-controlled ejection of a polymer from a virus capsid. *Phys. Rev. Lett.*, 102:088101, Feb 2009.

[82] R. Metzler, A. Hanke, P.G. Dommersnes, Y. Kantor, and M. Kardar. Equilibrium shapes of flat knots. *Phys. Rev. Lett.*, 88:188101, Apr 2002.

[83] R. Metzler, A. Hanke, P.G. Dommersnes, Y. Kantor, and M. Kardar. Tightness of slip-linked polymer chains. *Phys. Rev. E*, 65:061103, 2002.

[84] R. Metzler, W. Reisner, R. Riehn, R. Austin, J.O. Tegenfeldt, and I.M. Sokolov. Diffusion mechanisms of localised knots along a polymer. *EPL (Europhysics Letters)*, 76:696, 2006.

[85] C. Micheletti, D. Marenduzzo, and E. Orlandini. Polymers with spatial or topological constraints: theoretical and computational results. *Physics Reports*, 2011.

[86] C. Micheletti, D. Marenduzzo, E. Orlandini, and D. W. Sumners. Knotting of random ring polymers in confined spaces. *J. Chem. Phys.*, 124:64903–64903, Feb 2006.

[87] C. Micheletti, D. Marenduzzo, E. Orlandini, and D. W. Sumners. Simulations of knotting in confined circular dna. *Biophys J.*, 95:3591–3599, Oct 2008.

[88] C. Micheletti and E. Orlandini. Knotting and metric scaling properties of dna confined in nano-channels: a monte carlo study. *Soft Matter*, 2012.

[89] J. P. J. Michels and F.W. Wiegel. On the topology of a polymer ring. *Proc. R. Soc. Lond.*, A403:269–284, 1986.

[90] K. Millett, A. Dobay, and A. Stasiak. Linear random knots and their scaling behavior. *Macromolecules*, 38:601, 2005.

[91] K.C. Millett. Knots, slipknots, and ephemeral knots in random walks and equilateral polygons. *Journal of Knot Theory and its Ramifications*, 19(5):601–615, 2010.

[92] N. T. Moore, R. C. Lua, and A. Y. Grosberg. Topologically driven swelling of a polymer loop. *Proceedings of the National Academy of Sciences of the United States of America*, 101:13431, 2004.

[93] D. C. Morse. Viscoelasticity of concentrated isotropic solutions of semiflexible polymers. 1. Model and stress tensor. *Macromolecules*, 31:7030, 1998.

[94] M. Müller, J. P. Wittmer, and M. E. Cates. Topological effects in ring polymers: A computater simulation study. *Phys. Rev. E*, 53:5063, 1996.

[95] M. Müller, J. P. Wittmer, and M. E. Cates. Topological effects in ring polymers. II. influence of persistence length. *Phys. Rev. E*, 61:4078, 2000.

[96] M. Muthukumar. Translocation of a confined polymer through a hole. *Phys. Rev. Lett.*, 86(14):3188–3191, Apr 2001.

[97] T. Odijk. The statistics and dynamics of confined or entangled stiff polymers. *Macromol.*, 16:1340–1344, 1983.

[98] E. Orlandini, A. L. Stella, C. Vanderzande, and F. Zonta. Slow topological time scale of knotted polymers. *J. Phys. A: Math. Theor.*, 41:122002, 2008.

[99] E Orlandini, A.L. Stella, and C. Vanderzande. The size of knots in polymers. *Phys. Biol.*, 6:025012, 2009.

[100] E. Orlandini, M.C. Tesi, E.J. Rensburg, and S.G. Whittington. Entropic exponents of lattice polygons with specified knot type. *Journal of Physics A: Mathematical and General*, 29:L299, 1996.

[101] E. Orlandini, M.C. Tesi, E.J. Rensburg, and S.G. Whittington. Asymptotics of knotted lattice polygons. *Journal of Physics A: Mathematical and General*, 31:5953, 1998.

[102] E. Orlandini and S. G. Whittington. Statistical topology of closed curves: some applications in polymer physics. *Rev. Mod. Phys.*, 79:611, 2007.

[103] Enzo Orlandini, Attilio L. Stella, and Carlo Vanderzande. Geometry and topology of knotted ring polymers in an array of obstacles. *Phys Rev E Stat Nonlin Soft Matter Phys*, 82(5 Pt 1):050804, Nov 2010.

[104] Anton S. Petrov and Stephen C. Harvey. Packaging double-helical dna into viral capsids: structures, forces, and energetics. *Biophys J*, 95(2):497–502, Jul 2008.

[105] S. Plimpton. Fast parallel algorithms for short range molecular dynamics. *J. Comp. Phys.*, 117:119, 1995.

[106] Rudi Podgornik, Per Lyngs Hansen, and V. Adrian Parsegian. Elastic moduli renormalization in self-interacting stretchable polyelectrolytes. *The Journal of Chemical Physics*, 113(20):9343–9350, 2000.

[107] R. Potestio, C. Micheletti, and H. Orland. Knotted vs. unknotted proteins: evidence of knot-promoting loops. *PLoS computational biology*, 6(7):e1000864, 2010.

[108] Prashant K. Purohit, Jané Kondev, and Rob Phillips. Mechanics of DNA packaging in viruses. *Proceedings of the National Academy of Sciences of the United States of America*, 100(6):3173–3178, Mar 2003.

[109] S. R. Quake. Topological effects of knots in polymers. *Phys. Rev. Lett.*, 73:3317, 1994.

[110] D. Reith, A. Milchev, P. Virnau, and K. Binder. Anomalous structure and scaling of ring polymer brushes. *Europhys. Lett.*, 95:28003, 2011.

[111] D. Reith, L. Mirny, and P. Virnau. Gpu based molecular dynamics simulations of polymer rings in concentrated solution: Structure and scaling. *Progress of Theoretical Physics Supplement*, 191:135–145, 2011.

[112] C. Robinson. The cholesteric phase in polypeptide solutions and biological structures. *Molecular Crystals and Liquid Crystals*, 1(4):467–494, 1966.

[113] Geoffrey C. Rollins, Anton S. Petrov, and Stephen C. Harvey. The role of dna twist in the packaging of viral genomes. *Biophys J*, 94(5):L38–L40, Mar 2008.

[114] A. Rosa, M. Di Ventra, and C. Micheletti. Topological jamming of spontaneously knotted polyelectrolyte chains driven through a nanopore. *Physical Review Letters*, 109(11):118301, 2012.

[115] A. Rosa and R. Everaers. Structure and dynamics of interphase chromosomes. *PLOS Comp. Biol.*, 4:e1000153, 2008.

[116] A. Rosa, E. Orlandini, L. Tubiana, and C. Micheletti. Structure and dynamics of ring polymers: entanglement effects because of solution density and ring topology. *Macromolecules*, 44(21):8668–8680, 2011.

[117] M. Rubinstein. Dynamics of ring polymers in the presence of fixed obstacles. *Phys. Rev. Lett.*, 57:3023, 1986.

[118] M. Rubinstein and R. H. Colby. *Polymer Physics*. Oxford University Press, New York, 2003.

[119] J. Rudnick and G. Gaspari. The shapes of random walks. *Science*, 237:384, 1987.

[120] V. V. Rybenkov, N. R. Cozzarelli, and A. V. Vologodskii. Probability of DNA knotting and the effective diameter of the dna double helix. *Proceedings of the National Academy of Sciences of the United States of America*, 90:5307–5311, Jun 1993.

[121] A. M. Saitta, P. D. Soper, E. Wasserman, and M. L. Klein. Influence of a knot on the strength of a polymer strand. *Nature*, 399:46–48, 1999.

[122] Jorge B. Schvartzman and Andrzej Stasiak. A topological view of the replicon. *EMBO Rep*, 5(3):256–261, Mar 2004.

[123] S.Y. Shaw and J.C. Wang. Knotting of a dna chain during ring closure. *Science*, 260:533–536, 1994.

[124] A. Siber, M. Dragar, V. A. Parsegian, and R. Podgornik. Packing nanomechanics of viral genomes. *Eur Phys J E Soft Matter*, 26(3):317–325, Jul 2008.

[125] D. E. Smith, S. J. Tans, S. B. Smith, S. Grimes, D. L. Anderson, and C. Bustamante. The bacteriophage straight phi29 portal motor can package dna against a large internal force. *Nature*, 413(6857):748–752, Oct 2001.

[126] J. M. Sogo, A. Stasiak, M. L. Martínez-Robles, D. B. Krimer, P. Hernández, and J. B. Schvartzman. Formation of knots in partially replicated dna molecules. *J Mol Biol*, 286(3):637–643, Feb 1999.

[127] S. J. Spengler, A. Stasiak, and N. R. Cozzarelli. The stereostructure of knots and catenanes produced by phage lambda integrative recombination: implications for mechanism and dna structure. *Cell*, 42(1):325–334, Aug 1985.

[128] Christopher B. Stanley, Helen Hong, and Helmut H. Strey. Dna cholesteric pitch as a function of density and ionic strength. *Biophys J*, 89(4):2552–2557, Oct 2005.

[129] A. Stasiak, V. Katritch, J. Bednar, D. Michoud, and J. Dubochet. Electrophoretic mobility of dna knots. *Nature*, 384(6605):122, Nov 1996.

[130] H. H. Strey, R. Podgornik, D. C. Rau, and V. A. Parsegian. Dna–dna interactions. *Curr Opin Struct Biol*, 8(3):309–313, Jun 1998.

[131] D.W. Sumners and S.G. Whittington. Knots in self-avoiding walks. *Journal of Physics A: Mathematical and General*, 21(7):1689, 1988.

[132] W.R. Taylor. A deeply knotted protein structure and how it might fold. *Nature*, 406(6798):916–919, 2000.

[133] M.C. Tesi, E.J.J. Rensburg, E. Orlandini, and S.G. Whittington. Monte carlo study of the interacting self-avoiding walk model in three dimensions. *Journal of statistical physics*, 82(1):155–181, 1996.

[134] F. Tombolato and A. Ferrarini. From the double-stranded helix to the chiral nematic phase of B-DNA: a molecular model. *J. Chem. Phys.*, 122(5):54908, Feb 2005.

[135] Sonia Trigueros and Joaquim Roca. Production of highly knotted dna by means of cosmid circularization inside phage capsids. *BMC Biotechnol*, 7:94, 2007.

[136] G. Tsolou, N. Stratikis, C. Baig, P. S. Stephanou, and V. G. Mavrantzas. Melt structure and dynamics of unentangled polyethylene rings: Rouse theory, atomistic molecular dynamics simulation, and comparison with the linear analogues. *Macromolecules*, 43:10692, 2010.

[137] K. Tsurusaki and T. Deguchi. Fractions of particular knots in gaussian random polygons. *Journal of the Physical Society of Japan*, 64:1506, May 1995.

[138] Luca Tubiana, Enzo Orlandini, and Cristian Micheletti. Multiscale entanglement in ring polymers under spherical confinement. *Phys. Rev. Lett.*, 107:188302, Oct 2011.

[139] Luca Tubiana, Enzo Orlandini, and Cristian Micheletti. Probing the entanglement and locating knots in ring polymers: A comparative study of different arc closure schemes. *Progress of Theoretical Physics Supplement*, 191:192–204, 2011.

[140] C. Tzoumanekas, F. Lahmar, B. Rousseau, and D. N. Theodorou. Onset of entanglements revisited. topological analysis. *Macromolecules*, 42:7474, 2009.

[141] C. Tzoumanekas and D. N. Theodorou. Topological analysis of linear polymer melts: a statistical approach. *Macromolecules*, 39:4592, 2006.

[142] N. Uchida, G. S. Grest, and R. Everaers. Viscoelasticity and primitive-path analysis of entangled polymer liquids: from f-actin to polyethilene. *J. Chem. Phys.*, 128:044902, 2008.

[143] T. Vettorel, A. Y. Grosberg, and K. Kremer. Statistics of polymer rings in the melt: a numerical simulation study. *Phys. Biol.*, 6:025013, 2009.

[144] J. Vinograd, J. Lebowitz, R. Radloff, R. Watson, and P. Laipis. The twisted circular form of polyoma viral DNA. *Proceedings of the National Academy of Sciences of the United States of America*, 53(5):1104–1111, 1965.

[145] Peter Virnau, Yacov Kantor, and Mehran Kardar. Knots in globule and coil phases of a model polyethylene. *Journal of the American Chemical Society*, 127(43):15102–15106, 2005.

[146] A. Vologodskii. Brownian dynamics simulation of knot diffusion along a stretched dna molecule. *Biophys. J.*, 90:1594, 2006.

[147] Alexander V. Vologodskii, Nancy J. Crisona, Ben Laurie, Piotr Pieranski, Vsevolod Katritch, Jacques Dubochet, and Andrzej Stasiak. Sedimentation and electrophoretic migration of dna knots and catenanes. *Journal of Molecular Biology*, 278(1):1 – 3, 1998.

[148] A.V. Vologodskii, A.V. Lukashin, M.D. Frank-Kamenetskii, and Anshelevich V.V. The knot problem in statistical mechanics of polymer chains. *Sov. Phys.-JETP*, 39:1059–1063, 1974.

[149] J. C. Wang, K. V. Martin, and R. Calendar. On the sequence similarity of the cohesive ends of coliphage p4, p2, and 186 deoxyribonucleic acid. *Biochemistry*, 12(11):2119–2123, May 1973.

[150] S. A. Wasserman, J. M. Dungan, and N. R. Cozzarelli. Discovery of a predicted dna knot substantiates a model for site-specific recombination. *Science*, 229(4709):171–174, Jul 1985.

[151] C. Weber, A. Stasiak, P. De Los Rios, and G. Dietler. Numerical simulation of gel electrophoresis of dna knots in weak and strong electric fields. *Biophys. J.*, 90:3100, 2006.

[152] Roger Weil and Jerome Vinograd. The cyclic helix and cyclic coil forms of polyoma viral dna. *Proceedings of the National Academy of Sciences of the United States of America*, 50(4):730–738, 1963.

[153] S. A. Wischnewski, M. Monkenbusch, L. Willner, D. Richter, and G. Kali. Direct observation of the transition from free to constrained single-segment motion in entangled polymer melts. *Phys. Rev. Lett.*, 90:058302, 2003.

[154] B. H. Zimm and W. H. Stockmayer. The dimensions of chain molecules containing branches and rings. *J. Chem. Phys.*, 17:1301, 1949.